JETP Letters, Vol. 74, No. 4, 2001, pp. 191–195. Translated from Pis'ma v Zhurnal Éksperimental'noĭ i Teoreticheskoĭ Fiziki, Vol. 74, No. 4, 2001, pp. 211–215.

Gell-Mann–Low Function in QED

I. M. Suslov

Kapitza Institute for Physical Problems, Russian Academy of Sciences, ul. Kosygina 2, Moscow, 117973 Russia
e-mail: suslov@kapitza.ras.ru

Received July 10, 2001

The Gell-Mann–Low function $\beta(g)$ in QED (g is the fine structure constant) is reconstructed. At large g, it behaves as $\beta_\infty g^\alpha$ with $\alpha \approx 1$ and $\beta_\infty \approx 1$. © *2001 MAIK "Nauka/Interperiodica".*

PACS numbers: 12.20.Ds; 11.10.Gh

Recently [1, 2], I developed a method of summing divergent perturbation series with arbitrary coupling constants. With this method, information about all terms of the series is obtained by the interpolation of the known first terms exhibiting Lipatov asymptotic behavior [3]. In this paper, this method will be used to reconstruct the Gell-Mann–Low function in QED.

Lipatov's method [3] is based on the saddle-point calculation of path integrals near instanton configurations and is being questioned because of the possible renormalon contributions [4]. Formally, the asymptotic behavior of perturbation theory is determined by the singularity nearest to the origin in the Borel plane. Whereas the presence of instanton singularities is beyond question, the existence of renormalon singularities has never been proved, which is acknowledged by the most active advocates of this direction [5]. Having been proved in [6], the absence of renormalon singularities in the φ^4 theory casts some doubt on the renormalon concept as a whole, although similar proofs are lacking for other field theories. In such a situation, I believe that it can be assumed that the renormalon singularities are absent.

1. The asymptotic form of perturbation theory for QED was discussed in the late 1970s [7–9]; all fundamental problems were solved by Bogomolny and Fateyev [8, 9], but they did not find specific values for their calculations. Below, I partially fill this gap.

The vertex with M photon and $2L$ electron free lines is determined by the path integral

$$Z_{M,L} = \int DAD\bar{\psi}D\psi A(x_1)\ldots A(x_M)\psi(y_1)\bar{\psi}(z_1)\ldots\psi(y_L) \times \bar{\psi}(z_L)\exp\left\{-\int d^4x\left[\frac{1}{4}(\partial_\mu A_\nu - \partial_\nu A_\mu)^2 + \bar{\psi}(i\gamma_\nu\partial_\nu - m + e\gamma_\nu A_\nu)\psi\right]\right\}. \quad (1)$$

Integration with respect to the fermion fields gives

$$Z_{M,L} = \int DAA(x_1)\ldots A(x_M)G(y_1, z_1)\ldots G(y_L, z_L) \times \det(i\gamma_\nu\partial_\nu - m + e\gamma_\nu A_\nu) \times \exp\left\{-\frac{1}{4}\int d^4x(\partial_\mu A_\nu - \partial_\nu A_\mu)^2\right\} + \ldots, \quad (2)$$

where $G(x, x')$ is the Green's function for the Dirac operator

$$(i\gamma_\nu\partial_\nu - m + e\gamma_\nu A_\nu)G(x, x') = \delta(x - x'), \quad (3)$$

and the ellipsis stands for the terms with other pairings of $\psi(y_i)$ and $\bar{\psi}(z_k)$. Estimations show that the quantity $eA_\nu(x)$ is large for the saddle-point configuration and the asymptotic form of the determinant at $e \longrightarrow i\infty$ can be used, because the growth rate is maximal at imaginary e values [9]:

$$\ln\det(i\gamma_\nu\partial_\nu - m + e\gamma_\nu A_\nu) = \frac{e^4}{12\pi^2}\int d^4x(A_\nu^2)^2. \quad (4)$$

This result is not gauge invariant and is only valid for a specifically chosen gauge; it can be obtained for slowly varying fields or for configurations with a sufficiently high symmetry [9]. Taking Eq. (4) into account, a path integral with effective action

$$S_{\text{eff}}\{A\} = \int d^4x\left\{\frac{1}{4}(\partial_\mu A_\nu - \partial_\nu A_\mu)^2 - \frac{4}{3}g^2(A_\nu^2)^2\right\}, \quad g = \frac{e^2}{4\pi}, \quad (5)$$

appears in Eq. (2); the asymptotic form of perturbation theory for this action can be found by Lipatov's method. Its structure is determined by the homogeneity

properties of the action [10]; when g^2 is used as a coupling constant, these properties are the same as in the φ^4 theory, and the general asymptotic term has the form $cS_0^{-N}\Gamma(N+b)g^{2N}$, where S_0 is the instanton action. In actuality, the expansion is in arbitrary integer (not only even) g powers, and the general term is $cS_0^{-N/2}\Gamma(N/2+b)g^N$.[1] Taking the value of instanton action into account, one obtains for the Nth-order contribution to the vacuum integral ($M = 0$, $L = 0$) [8]:

$$Z_N(-g)^N = \text{const}\left(\frac{3^{3/2}}{4\pi^3}\right)^{N/2}\Gamma\left(\frac{N+r}{2}\right)(-g)^N, \quad (6)$$

where $r = 11$ is the number of zeroth modes including four translations, a scale transformation, and six four-dimensional rotations (instanton corresponds in symmetry to a rigid body of an irregular shape).

In the general case, the functional form of the result can be found by structural calculations described in [10] and reduced to dimensional analysis. It is easy to show that $e_c \sim N^{-1/4}$ and $A_c(x) \sim N^{1/2}$ for the saddle-point configuration. To find the dimension of $G(x, x')$, consider the Dyson equation

$$G(x,x') = G_0(x-x') - \int d^4y G_0(x-y)e\gamma_\nu A_\nu(y)G(y,x') \quad (7)$$

which follows from Eq. (3). In order to clarify the structure of the solution, let us consider the scalar analogue of Eq. (7) and assume that the function $A_\nu(x)$ is strongly localized near $x = 0$; one can then set $G(y, x') \approx G(0, x')$ in the integral, after which the equation is easily solved:

$$G(x,x') = G_0(x-x') - \frac{G_0(-x')\int d^4y G_0(x-y)e\gamma_\nu A_\nu(y)}{1+\int d^4y G_0(-y)e\gamma_\nu A_\nu(y)}. \quad (8)$$

Because $eA_\nu(x) \sim N^{1/4}$ and Eq. (8) is finite in the limit $e \longrightarrow \infty$, one has $G(x, x') \sim N^0$. It is natural to expect that this result is quite general and is not caused by the above assumptions. The Nth-order contribution to the integral in Eq. (1) has the form

$$\text{const}\left(\frac{3^{3/2}}{4\pi^3}\right)^{N/2}\Gamma\left(\frac{N+r+M}{2}\right)(-g)^N \quad (9)$$

for even M and, with the extra factor $eN^{1/4}$, for odd M values.

[1] The direct expansion of Eq. (2) in powers of the last term in Eq. (5) is incorrect, because the functional integration will then include the configurations for which result (5) is invalid. The calculation should be carried out by the saddle-point method, which yields a continuous function of N; the fact that it must be taken at the integer or half-integer points is an external condition.

High-power coefficients in the expansion of the Gell-Mann–Low function $\beta(g) = \sum_N \beta_N(-g)^N$ coincide, except for a constant factor, with the coefficients for the invariant charge [3], which is determined in the electrodynamics by the quantity gD, where D is the photon propagator ($M = 2$, $L = 0$). The general asymptotic term is $D_N(-g)^{N+1} \sim NZ_N(-g)^{N+1}$ or $NZ_{N-1}(-g)^N \sim N^{1/2}Z_N(-g)^N$, from whence it follows that

$$\beta_N = \text{const}\times 4.886^{-N}\Gamma\left(\frac{N+12}{2}\right), \quad N \longrightarrow \infty. \quad (10)$$

The same result is obtained if the invariant charge is determined through the triple vertex ($M = 1$, $L = 1$). In this case, the dominant contribution to the asymptotic expression comes from the elimination of the photon line.

2. The following four terms of the β-function expansion in the MOM scheme are known [11]

$$\beta(g) = \frac{4}{3}g^2 + 4g^3 + \left[\frac{64}{3}\zeta(3) - \frac{202}{9}\right]g^4 + \left[186 + \frac{256}{3}\zeta(3) - \frac{1280}{3}\zeta(5)\right]g^5 + \dots . \quad (11)$$

The series summation procedure should be somewhat modified as compared to [1, 2], because Lipatov's asymptotic expression has the form $ca^N\Gamma(N/2+b)$ instead of $ca^N\Gamma(N+b)$. The Borel transform $B(z)$ is defined as

$$\beta(g) = \int_0^\infty dx e^{-x}x^{b_0-1}B(ag\sqrt{x}),$$
$$B(z) = \sum_{N=0}^\infty B_N(-z)^N, \quad B_N = \frac{\beta_N}{a^N\Gamma(N/2+b_0)}, \quad (12)$$

where b_0 is an arbitrary parameter. The conformal mapping $z = u/(1-u)$ of the Borel transform provides a convergent series in u with the coefficients

$$U_N = \sum_{K=1}^N B_K(-1)^K C_{N-1}^{K-1} (N \geq 1), \quad U_0 = B_0, \quad (13)$$

whose large-N behavior

$$U_N = U_\infty N^{\alpha-1}, \quad U_\infty = \frac{\beta_\infty}{a^\alpha\Gamma(\alpha)\Gamma(b_0+\alpha/2)} \quad (14)$$

determines the parameters of the asymptotic expression $\beta(g) = \beta_\infty g^\alpha$ at $g \longrightarrow \infty$.

The interpolation is performed for the reduced coefficient function

$$F_N = \frac{\beta_N}{\beta_N^{as}} = A_0 + \frac{A_1}{N-\tilde{N}} + \frac{A_2}{(N-\tilde{N})^2} + \ldots, \qquad (15)$$
$$\beta_N^{as} = a^N N^{\tilde{b}} \Gamma(N/2 + b - \tilde{b}),$$

by cutting off the series and choosing the coefficients A_K so that Eq. (15) coincides with the known F_N values. Optimal parametrization is carried out for $\tilde{b} = b - 1/2 = 5.5$ [2], while the parameter $\tilde{N}$ is used for checking on the stability of the results and for numerical optimization. In contrast to the φ^4 theory [1, 2], the general coefficient (10) in the asymptotic expression is unknown. Technically, this is not a problem because the parameter A_0 in Eq. (15) is not considered as known but is found by interpolation. However, this leads to a much greater uncertainty in the function F_N; its first values (in units of 10^3) $F_2 = 63.1$, $F_3 = -7.02$, $F_4 = 0.34$, and $F_5 = 1.23$ exhibit only a weak tendency to become a constant, and the predicted value $A_0 = \lim_{N\to\infty} F_N$ changes by several orders of magnitude with changing $\tilde{N}$. At first glance, no reasonable results can be obtained in such a situation.

However, the algorithm used for determining the asymptotic form of $\beta(g)$ is, in a sense, "superstable": the addition of an arbitrary mth-order polynomial $P_m(N)$ to B_N does not change the coefficients U_N at $N \geq m + 2$ [2]. This property can be generalized for a wide class of smooth functions: a change in U_N caused by the replacement $B_N \longrightarrow B_N + f(N)$, where $f(N)$ is an integer function with rapidly decreasing Taylor-series coefficients, rapidly decreases with N. Thus, smooth errors are immaterial even if they are large. In contrast, the nonsmooth errors lead to a catastrophic effect, which can be used to optimize interpolation: if the interpolation procedure is unsuccessful, the behavior of U_N at large N cannot be approximated by a power-law dependence [2].

To check this argumentation, a test experiment was carried out for the φ^4 theory. The use of complete information [i.e., coefficients β_2–β_5 and parameters A_0 and A_1 in Eq. (15)] gave $\alpha = 0.96 \pm 0.01$ and $\beta_\infty = 7.4 \pm 0.4$ [2]; the same procedure without the use of A_0 and A_1 gave $\alpha = 1.02 \pm 0.03$ and $\beta_\infty = 1.7 \pm 0.3$. Taking into account that the uncertainty in the coefficient function (estimated through varying $\tilde{N}$ by ~1 near its optimal value) amounts to few percent in the first case and more than an order of magnitude in the second, one can conclude that such a stability of the results is quite satisfactory.[2] Clearly, the results obtained below should only be treated as a zero approximation.

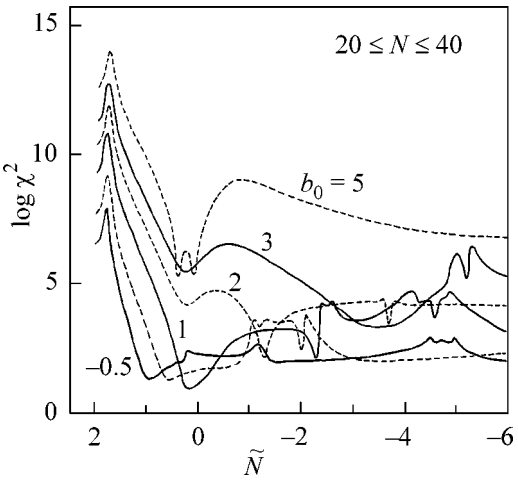

Fig. 1.

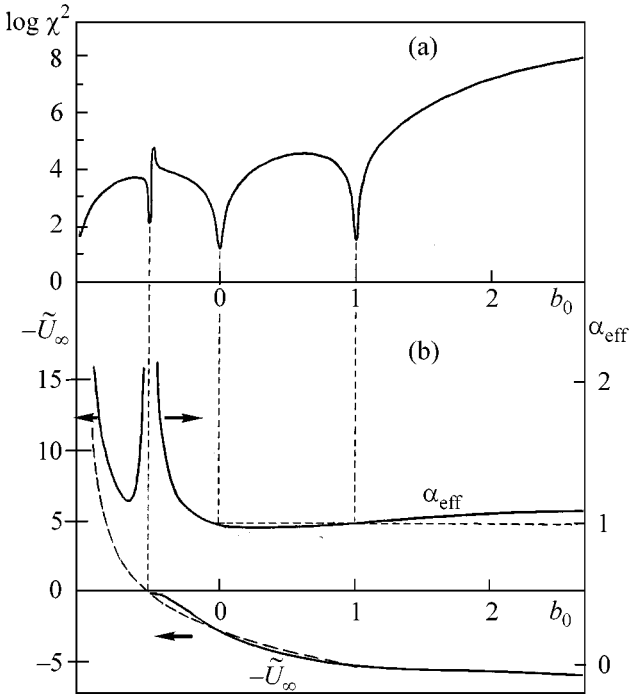

Fig. 2.

Following [2], let us approximate U_N by the power-law dependence for a fixed interval $20 \leq N \leq 40$ and different b_0 and $\tilde{N}$ values. The χ^2 dependence on $\tilde{N}$

[2] The difference in the β_∞ values is beyond the estimated accuracy, but this is quite explainable: the procedure proposed in [2] for estimating errors is only justified in the vicinity of the exact result, where all deviations can be linearized.

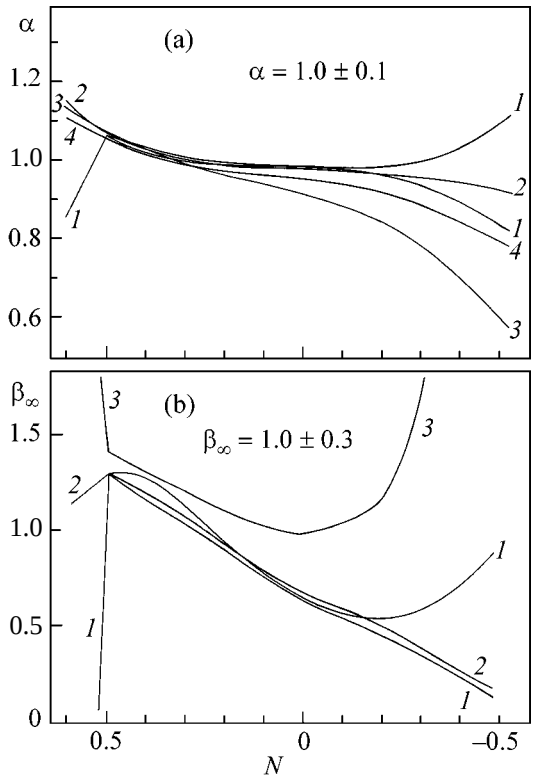

Fig. 3.

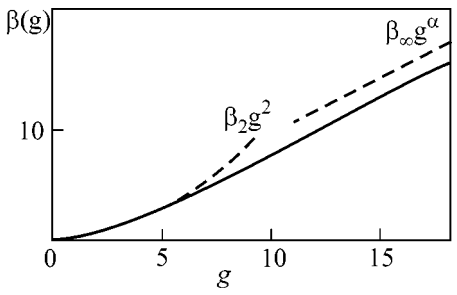

Fig. 4.

(Fig. 1) enables one to select a set of interpolations ($-0.5 \lesssim \tilde{N} \lesssim 1.0$) for which the power-law behavior of U_N is probable. The typical dependences of χ^2 and effective values of U_∞ and α on b_0 (Fig. 2) indicate that $\alpha \approx 1$.[3] Indeed, the quantity U_∞ reverses its sign [see Eq. (14)] at $b_0 = -\alpha/2 \approx -0.5$. At the same b_0 value, χ^2 has a minimum, which corresponds to the fact that the leading contribution $U_\infty N^{\alpha-1}$ vanishes and the power-law dependence $U_N \sim N^{\alpha'-1}$ prevails, where the index α' corresponds to the next correction to the asymptotic expression for $\beta(g)$ (it is assumed that $\beta(g) = \beta_\infty g^\alpha + \beta'_\infty g^{\alpha'} + \beta''_\infty g^{\alpha''} + \ldots$ at large g). The values of α_{eff} at the minima of χ^2 at $b_0 = -\alpha'/2, -\alpha''/2, \ldots$, where the respective corrections to Eq. (14) vanish, are closest to the exact value $\alpha \approx 1$ [2].[4]

Figure 3a shows different estimates for the α index as a function of $\tilde{N}$ [2]: (*1*) from the value of α_{eff} at the χ^2 minima corresponding to α' and α''; (*2*) from the position of the χ^2 minimum corresponding to $b_0 = -\alpha/2$; (*3*) from a change in sign of U_∞ when processing by taking the logarithm of U_N (solid line in Fig. 2b); and (*4*) the same but for processing with a fixed index (dashed line in Fig. 2b). Figure 3b shows different estimates obtained for β_∞: (*1*) from the U_∞ value at the χ^2 minima corresponding to α' and α'' and (*2*) and (*3*) from the slope of the linear portion of the $U_\infty(b_0)$ dependence near the root (upper and lower estimates, respectively). The discrepancy between different estimates gives a measure of uncertainty of the results. For $\tilde{N} \le 0.25$, the results for α are consistent with a value slightly smaller than unity. For $\tilde{N} > 0.25$, there is a systematic increase to 1.08, which is beyond the error, but the χ^2 minima are ill-defined and unstable in this case. Similar behavior is observed for β_∞. With the most reliable values in the middle of the chosen $\tilde{N}$ interval, the following conservative estimate can be given for the accuracy including systematic changes:

$$\alpha = 1.0 \pm 0.1, \quad \beta_\infty = 1.0 \pm 0.3. \qquad (16)$$

It follows from above that even this estimate of error is not reliable.

It is easy to sum up the series for arbitrary g by calculating the U_N coefficients in Eq. (13) for $N \lesssim 30$ and continuing them according to the asymptotic expression found for $U_\infty N^{\alpha-1}$. Figure 4 shows the results for $\tilde{N} = 0.2$ and $b_0 = 0$. The one-loop law $\beta_2 g^2$ matches the asymptotic dependence $\beta_\infty g^\alpha$ at $g \sim 10$. At $g < 5$, $\beta(g)$ differs only slightly from the one-loop result. Within the accuracy adopted, the asymptotic expression for $\beta(g)$ coincides with the upper limit of inequality $0 \le \beta(g) < g$, which was derived in [12] from spectral considerations. For $\alpha = 1$ and $\beta_\infty = 1$, the fine structure constant in pure electrodynamics increases at small distances L as L^{-2}.

This work was supported by INTAS (grant no. 99-1070) and the Russian Foundation for Basic Research (project no. 00-02-17129).

[3] For technical reasons, Fig. 2 shows the quantity $\tilde{U}_\infty = U_\infty \Gamma(b_0 + 1)$.

[4] In the test examples, minima of χ^2 are usually observed only for α and α' [2]. The appearance of additional minima is probably specific to a small amount of information; it was observed in the above-mentioned test experiment for the φ^4 theory.

REFERENCES

1. I. M. Suslov, Pis'ma Zh. Éksp. Teor. Fiz. **71**, 315 (2000) [JETP Lett. **71**, 217 (2000)].
2. I. M. Suslov, Zh. Éksp. Teor. Fiz. **120**, 5 (2001) [JETP **93**, 1 (2001)].
3. L. N. Lipatov, Zh. Éksp. Teor. Fiz. **72**, 411 (1977) [Sov. Phys. JETP **45**, 216 (1977)].
4. G. t'Hooft, in *The Whys of Subnuclear Physics: Proceedings of the 1977 International School of Subnuclear Physics, Erice, 1977*, Ed. by A. Zichichi (Plenum, New York, 1979).
5. M. Beneke, Phys. Rep. **317**, 1 (1999), Sect. 2.4.
6. I. M. Suslov, Zh. Éksp. Teor. Fiz. **116**, 369 (1999) [JETP **89**, 197 (1999)].
7. C. Itzykson, G. Parisi, and J. B. Zuber, Phys. Rev. D **16**, 996 (1977); R. Balian, C. Itzykson, G. Parisi, and J. B. Zuber, Phys. Rev. D **17**, 1041 (1978).
8. E. B. Bogomolny and V. A. Fateyev, Phys. Lett. B **76B**, 210 (1978).
9. E. B. Bogomolny, V. A. Fateyev, and L. N. Lipatov, Sov. Sci. Rev., Sect. A **2**, 247 (1980).
10. I. M. Suslov, Zh. Éksp. Teor. Fiz. **117**, 659 (2000) [JETP **90**, 571 (2000)].
11. S. G. Gorishny, A. L. Kataev, S. A. Larin, and L. R. Surguladze, Phys. Lett. B **256**, 81 (1991).
12. N. V. Krasnikov, Nucl. Phys. B **192**, 497 (1981); H. Yamagishi, Phys. Rev. D **25**, 464 (1982).

Translated by R. Tyapaev

JETP Letters, Vol. 74, No. 4, 2001, pp. 196–199. Translated from Pis'ma v Zhurnal Éksperimental'noĭ i Teoreticheskoĭ Fiziki, Vol. 74, No. 4, 2001, pp. 216–219.

Test for the *CPT* Invariance of Bound States in QED and Production of Muonium or Antimuonium in Electron or Positron Scattering by Nuclei

G. A. Kazakov and É. A. Choban*

St. Petersburg State Technical University, ul. Politekhnicheskaya 29, St. Petersburg, 195251 Russia

** e-mail: choban@part.hop.stu.neva.ru*

Received June 18, 2001; in final form, July 20, 2001

The possibility of testing the QED *CPT* invariance of bound states is analyzed for muonium or antimuonium produced in electron or positron scattering by nuclei. The number of muonium production events is estimated for modern accelerators. The method of muonium detection by measuring oscillations appearing in the decay curve owing to the interference of the muonium ground and excited states is discussed. © *2001 MAIK "Nauka/Interperiodica"*.

PACS numbers: 11.30.Er; 12.20.Ds; 25.30.Rw

Test for *CPT* invariance of quantum field theory (QFT), in particular QED, is one of the most important problems of high energy physics, because locality and relativistic invariance are the basic postulates of QFT [1, 2]. As shown in [3], this leads to the *C*, *P*, and *T* invariance of the QFT Lagrangian. The identity of the particle and antiparticle masses is the simplest consequence of *CPT* invariance and is presently fulfilled with a high accuracy; e.g., one has for μ^+ and μ^- mesons, $m_{\mu^+}/m_{\mu^-} = 1.000024 \pm 0.000078$ [4]. At the same time, the problem of *CPT* invariance of bound states is much less clear. Munger *et al*. [5] suggested that the Lamb shift of the hydrogen $2S_{1/2}$–$2P_{1/2}$ transition be compared with that of the antihydrogen atoms $\overline{H}{}_1^1$ produced in $\bar{p}Z$ collisions. However, the current statistics are about one-fortieth of those necessary for a reliable conclusion.

In this paper, we consider the production of muonium M^0 or antimuonium $\overline{M}{}^0$ in the processes

$$\begin{aligned} e^- + Z &\longrightarrow Z + M^0 + \mu^-, \\ e^+ + Z &\longrightarrow Z + \overline{M}{}^0 + \mu^+, \end{aligned} \tag{1}$$

where $M^0(\overline{M}{}^0)$ is a bound state of μ^+, e^- (μ^-, e^+). The dominant contribution to the amplitude of processes (1) comes from the diagrams shown in Fig. 1. Before writing the amplitudes of processes (1) (the $e^-Z \longrightarrow ZM^0\mu^-$ process is taken as an example), we consider the recombination vertex $e^- + \mu^+ \longrightarrow M^0$, $e^+ + \mu^- \longrightarrow \overline{M}{}^0$. This vertex was obtained by solving the Bethe–Salpeter equation with one-photon exchange kernel, whose diagrammatic representation is shown in Fig. 2 [6]. Let us introduce the quantity

$$\hat{X}(p, k-p) = \hat{G}_{\mu^+}(k-p)\hat{\Gamma}_0\hat{G}_{e^-}(p), \tag{2}$$

where $\hat{G}_{e^-}(p) = 1/(\hat{p} - m_e)$ and $\hat{G}_{\mu^+}(k-p) = 1/(\hat{p} - \hat{k} - m_\mu)$ are the electron and muon propagators, respectively, and $\hat{\Gamma}_0$ is the recombination vertex $e^- + \mu^+ \longrightarrow M^0$ in the diagrams in Fig. 1. Then, the solution of the Bethe–Salpeter equation for $\hat{X}(p, k-p)$ can be represented as [6]

$$\begin{aligned} \hat{X}(p, k-p) &= \frac{\sqrt{m_\mu}}{2i}(1-\gamma_4)\gamma_5 \\ &\times \frac{(\mathbf{p}^2/2m_e - E_{\text{bound}})\Psi(\mathbf{p})}{(p_0 - m_e - \mathbf{p}^2/2m_e + i0)(p_0 - k_0 + m_\mu + \mathbf{p}^2/2m_\mu - i0)}, \end{aligned} \tag{3}$$

where m_e and m_μ are the electron and muon masses, respectively, and the Fourier transform of the wave function of e^- in M^0 has the form

$$\Psi(\mathbf{p}) = \frac{8\sqrt{\pi a_0^3}}{(1 + \mathbf{p}^2 a_0^2)^2}, \quad a_0 = \frac{1}{m_e\alpha} \quad (\hbar = c = 1),$$

$$\alpha = \frac{e^2}{4\pi} = \frac{1}{137}.$$

Taking the diagrams in Fig. 1 into account and substituting vertex (3) into the amplitude, we obtain the

0021-3640/01/7404-0196$21.00

following expression for the amplitude of process (1) with e^-:

$$M = \frac{(4\pi\alpha)^2}{q^2}\Psi(0)l_\mu\frac{\sqrt{m_\mu}}{m_e(\omega^2-2qk)^2(q^2-2qk)}$$
$$\times\bar{u}(\mathbf{p}_1')\gamma_5\{2(2qk-\omega^2)[qp_1'\gamma_\mu-\hat{q}p_{1\mu}'] \quad (4)$$
$$+m_\mu[(q^2-2qk)(2p_{1\mu}'-\gamma_\mu\hat{q})$$
$$-(\omega^2-2qk)(\hat{q}\gamma_\mu-2k_\mu)]\}u(\mathbf{p}_1),$$

where $\omega^2 = (p_1' + k)^2$ is the squared invariant mass of the (M^0, μ^-) system, l_μ is the nuclear electromagnetic current, and $\Psi(0) = 1/\sqrt{\pi a_0^3}$. The amplitude squared includes the tensor

$$R_{\mu\nu} = 4\left\{f_{1Z}^2(q^2)\left[2p_{2\mu}p_{2\nu}-(p_{2\mu}q_\nu+p_{2\nu}q_\mu)+\frac{q^2}{2}g_{\mu\nu}\right]\right.$$
$$+F_{2Z}^2(q^2)\left[2q^2m_Z^2g_{\mu\nu}+q^2(p_{2\mu}q_\nu+p_{2\nu}q_\mu)\right. \quad (5)$$
$$\left.\left.-q_\mu q_\nu\left(\frac{q^2}{2}+2m_Z^2\right)-2q^2p_{2\mu}p_{2\nu}\right]\right\},$$

which describes the lower block in the diagrams in Fig. 1 and involves the nuclear electromagnetic form factors F_{1Z} and F_{2Z}.

Let us introduce $x = \cos\theta$, where θ is the angle between the momentum of M^0 in the c.m.s. of the (M^0, μ^-) system and the momentum of e^- in the c.m.s. of the (e^-, Z) system. Using Eqs. (4) and (5), one can easily obtain the cross-section distribution over ω^2 and x in the form

$$\frac{d\sigma}{d\omega^2dx} = 4F_{1Z}^2(0)|\Psi(0)|^2\pi\alpha^4\frac{m_\mu}{m_e^2}\sqrt{1-\frac{4m_\mu^2}{\omega^2}}$$
$$\times\ln\left(\frac{S^3}{m_Z^2\omega^4}\right)\frac{1}{1+x\sqrt{1-4m_\mu^2/\omega^2}}\frac{S-\omega^2}{S\omega^6} \quad (6)$$
$$\times\left\{1+\frac{8m_\mu^2\sqrt{1-4m_\mu^2/\omega^2}[(1-x^2)\sqrt{1-4m_\mu^2/\omega^2}+2x]}{\omega^2[1-x^2(1-4m_\mu^2/\omega^2)](1-x\sqrt{1-4m_\mu^2/\omega^2})^2}\right\},$$

where $F_{1Z}(0) = Z$ and the approximation corresponds to the Weizsäcker–Williams method. One can see from this distribution that muonium is produced predominantly backwards in the (M^0, μ^-) c.m.s. Integration of

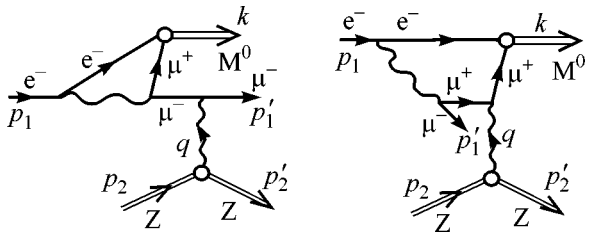

Fig. 1. Feynman diagrams making the dominant contribution to the amplitude of process (1).

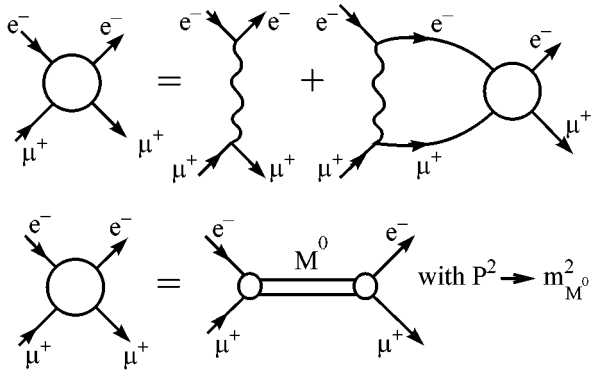

Fig. 2. Diagrammatic representation of the Bethe–Salpeter equation.

Eq. (6) with respect to x yields the cross-section distribution over ω^2

$$\frac{d\sigma}{d\omega^2} = 2Z^2\alpha^7\left(\frac{m_e}{m_\mu}\right)\sqrt{1-\frac{4m_\mu^2}{\omega^2}}\ln\left(\frac{S^3}{r_Z^2\omega^4}\right)\frac{S-\omega^2}{S\omega^4}$$
$$\times\left\{1-12\left(\frac{m_\mu^2}{\omega^2}\right)+\left[4\left(\frac{m_\mu^2}{\omega^2}\right)^2\left(1-6\frac{m_\mu^2}{\omega^2}\right)+2\frac{m_\mu^2}{\omega^2}\right]\right. \quad (7)$$
$$\left.\times\frac{1}{\sqrt{1-4m_\mu^2/\omega^2}}\ln\frac{1+\sqrt{1-4m_\mu^2/\omega^2}}{1-\sqrt{1-4m_\mu^2/\omega^2}}\right\}.$$

It follows from Eq. (7) that the distribution maximum occurs near the (M^0, μ^-)-production threshold $\omega^2 \sim 4m_\mu^2$. As ω^2 increases, the quantity $d\sigma/d\omega^2$ decreases noticeably and behaves as $d\sigma/d\omega^2 \sim 1/\omega^4$.

Finally, let us determine the total cross section for processes (1). Introducing $\xi = 4m_\mu^2/\omega^2$ and integrating Eq. (7) with respect to ξ, one obtains

$$\sigma = \left(\frac{Z^2\alpha^7m_e}{16m_\mu^3}\right)\int_0^1 f(\xi)d\xi,$$

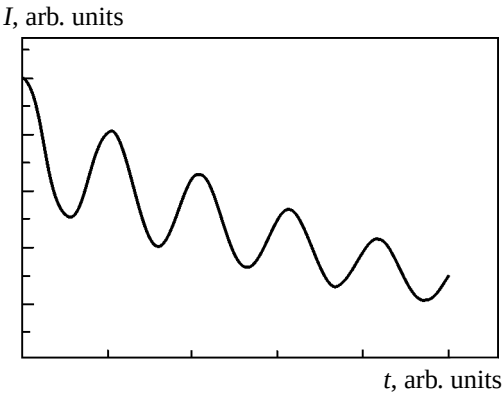

Fig. 3. The muonium decay curve with allowance made for the excited state.

$$f(\xi) = \ln\left(\frac{S^3\xi^2}{16m_Z^2m_\mu^4}\right) \tag{8}$$

$$\times\left\{2(4-3\xi^2)\sqrt{1-\xi}+\xi(4+2\xi-\xi^2)\ln\left(\frac{1+\sqrt{1-\xi}}{1-\sqrt{1-\xi}}\right)\right\}.$$

Let us estimate the cross sections for processes (1) for Tevatron-DIS (FNAL) [7], LHC [8], and Muon Collider [9] (secondary-lepton beams are implied). Cross section (8) is proportional to Z^2 and, therefore, can be increased by using a gaseous target with large Z [5], e.g., radon with spin 1/2. The cross sections, the differential luminosities, and the number of events expected in a year are given in the table.

Consider the method for detecting muonium M^0 and antimuonium $\overline{M}^0$, which are produced in processes (1) in the ground and excited states:

$$\Psi_{M^0}(0) = C_1\Psi_1(0) + C_2\Psi_2(0). \tag{9}$$

Note that solution (3) of the Bethe–Salpeter equation was obtained for the production of ground-state muonium. The production of excited muonium through the mechanisms for which C_2 includes additional smallness will be discussed below. Taking into account the muonium decay, the muonium wave function can be represented in the form

$$\Psi_{M^0}(t) = (C_1\Psi_1(t) + C_2\Psi_2(t))\exp(-\Gamma_{M^0}t/2\hbar). \tag{10}$$

Here, with $\tau_{M^0} \sim 10^{-6}$ s being the muonium lifetime, $\Gamma_{M^0} = \hbar/\tau_{M^0}$ is the decay width and $\Psi_1(t)$ and $\Psi_2(t)$ are determined as

$$\begin{aligned}\Psi_1(t) &= \Psi_1\exp\left(-\frac{i}{\hbar}E_1t\right),\\ \Psi_2(t) &= \Psi_2\exp\left(-\frac{i}{\hbar}E_2t\right),\end{aligned} \tag{11}$$

where E_1 and E_2 are the muonium energies in the ground and excited states, respectively.

The wave function of M^0 is normalized to the flux density:

$$\begin{aligned}\left|\Psi_{M^0}(0)\right|^2 &= |C_1|^2 + |C_2|^2 + 2|C_1C_2|\cos\delta\\ &= n_0 = I_0/v_{M^0},\end{aligned} \tag{12}$$

where I_0 is the muonium initial flux density, v_{M^0} is the muonium velocity, n_0 is the muonium concentration M^0 at $t = 0$, and δ is the relative phase of the complex coefficients C_1 and C_2. Because the I_0 measurement can start at an arbitrary time, one can set $\delta = 0$. The degree of muonium excitation is defined as

$$\varepsilon = \frac{I_{\text{exit}}}{I_0} = \frac{|C_2|^2}{|C_1+C_2|^2}. \tag{13}$$

Expressing C_1 and C_2 with the help of Eqs. (12) and (13) and taking into account Eqs. (10) and (11), one can easily obtain the flux density M_0 at arbitrary time t

$$\begin{aligned}I(t) = I_0\left\{1-2\sqrt{\varepsilon}(1-\sqrt{\varepsilon})\left[1-\cos\left(\frac{E_2-E_1}{\hbar}t\right)\right]\right\}\\ \times\exp\left(-\frac{\Gamma_{M^0}t}{\hbar}\right).\end{aligned} \tag{14}$$

It is seen that the decay curve $I(t)$ shown in Fig. 3 displays oscillations. Let us estimate the spatial period of oscillations, i.e., the distance corresponding to one oscillation in the curve in Fig. 3. According to Eq. (14), $\omega = (E_2 - E_1)/\hbar = 2\pi/T$, giving $T \approx 4\times10^{-16}$ s for $E_2 - E_1 = 10.1$ eV. Comparing T with τ_{M^0}, one sees that the time period of the oscillations is ten orders of magnitude shorter than τ_{M^0}; i.e., many oscillations shown in Fig. 3 fall within the M^0 lifetime.

Because the muonium is produced in process (1) with $E_{M^0} \gg m_{M^0}c^2$ (e.g., $E_{M^0} \sim 225$ GeV for Tevatron-

Data on the cross sections for processes (1) and the number N of events expected in a year

Accelerator	$\sqrt{S}$, GeV	σ, fb	L, cm^{-2} s^{-1}	N
FNAL (Tevatron-DIS)	477	17	2.1×10^{32}	1.1×10^2
LHC	14 000	28	10^{33}–10^{34}	8.8×10^2–8.8×10^3
Muon Collider	350	16	10^{32}	50

DIS), one has $T_{\text{lab}} = TE_{M^0}/m_{M^0}c^2 \approx 10^{-12}$ s. In this time, muonium covers a distance coinciding with the spatial oscillation period of about 300 μm. Effects at these distances are quite measurable.

Let us estimate the quantity ε that determines the contribution of the wave function Ψ_2 corresponding to the production of excited muonium M^{0*} in Eq. (10). There are two mechanisms of M^{0*} production: creation in the recombination vertex $e^- + \mu^+ \longrightarrow M^{0*}$ in the diagrams in Fig. 1 and the interaction in the final state with inelastic rescattering of M^0 by μ^- or the nucleus. Consider the first mechanism. Let M^{0*} be produced in the 2^1S_0 state. In this case, Eq. (3) includes $\Psi(\mathbf{p})$ of the form

$$\Psi(\mathbf{p}) = -\frac{32\sqrt{2\pi a_0^3}(1 - 4\mathbf{p}^2 a_0^2)}{(1 + 4\mathbf{p}^2 a_0^2)^3}, \qquad (15)$$

where a_0 is defined following Eq. (3) and the corresponding $\Psi(0) = 1/\sqrt{8\pi a_0^3}$. This gives ε = 1/256; i.e., the admixture of the excited Ψ_2 state in Eq. (10) is on the order of 10%. For the production of M^{0*} in one of the 2*P* states, the ε value is of the same order of magnitude. The second mechanism makes a noticeably smaller contribution.

Thus, a comparison of the decay curves with several oscillation periods for muonium and antimuonium will make it possible to establish whether the *CPT* invariance is obeyed for the bound states in QED.

We are grateful to V.G. Baryshevskiĭ for his idea of detecting muonium and antimuonium and to D. Roshchin for discussion of the solution to the Bethe–Salpeter equation.

REFERENCES

1. A. I. Akhiezer and V. B. Berestetskii, *Quantum Electrodynamics* (Nauka, Moscow, 1969; Wiley, New York, 1965).
2. N. N. Bogoliubov and D. V. Shirkov, *Introduction to the Theory of Quantized Fields* (Nauka, Moscow, 1976; Wiley, New York, 1980).
3. R. Jost, *The General Theory of Quantized Fields* (American Mathematical Society, Providence, Rhode Island, 1965; Mir, Moscow, 1967).
4. Particle Data Group, AIP Booklet, 1, 1998.
5. C. T. Munger, S. J. Brodsky, and I. Schmidt, Phys. Rev. D **49**, 3228 (1994).
6. E. A. Choban, Proc. SPIE **3345**, 162 (1998).
7. CERN Yellow Report **4**, 25 (2000).
8. P. Chiapetta, G. T. Gounaris, T. Luyssac, *et al.*, Phys. Rev. D **59**, 014016 (1999).
9. J. F. Gunion, Preprint UCD-98-5, hep-ph/9802258.

Translated by R. Tyapaev

JETP Letters, Vol. 74, No. 4, 2001, pp. 200–203. Translated from Pis'ma v Zhurnal Éksperimental'noĭ i Teoreticheskoĭ Fiziki, Vol. 74, No. 4, 2001, pp. 220–223.

Pair Radial Distribution Function of Simple Classical Liquids

Yu. V. Petrov and E. A. Shuryashkina*

Landau Institute for Theoretical Physics, Russian Academy of Sciences, Chernogolovka, Moscow region, 142432 Russia

** Moscow Institute of Physics and Technology, Institutskiĭ per. 9, Dolgoprudnyĭ, Moscow region, 171700 Russia*

Received June 21, 2001; in final form, July 16, 2001

The system of ordinary differential equations is derived for the self-consistent potential and pair radial distribution function of a simple classical liquid, for which the pair potential energy of "bare" particles is the sum of Yukawa potentials accounting for the repulsion at small distances and attraction at large distances. The number of parameters in the interaction potential is large enough for the interatomic interaction to be approximated in real fluids. The model suggested accounts for the vapor–liquid phase transition at the condensation curve on the temperature–concentration coordinates. © *2001 MAIK "Nauka/Interperiodica".*

PACS numbers: 61.20.Ne

The pair correlation function (pair radial distribution function) is of fundamental importance in the physics of simple classical liquids consisting of particles with pair central interaction potential $v(r)$ [1]. The pair radial distribution function $w(r)$ is defined as a number of particles dN in elementary volume dV at a distance r from a given particle in a liquid with mean particle concentration n_0:

$$dN = n_0 w(r) dV. \tag{1}$$

Taking into account that $dN/dV = n(r)$ is the particle concentration at a distance r from a given particle, one obtains

$$w(r) = \frac{n(r)}{n_0}. \tag{2}$$

Knowing function $w(r)$, it is easy to express the important thermodynamic functions such as pressure p (equation of state) and internal energy per atom ε as functions of n_0 and temperature T [2]:

$$p = n_0 T - \frac{1}{6} n_0^2 \int r \frac{dv(r)}{dr} w(r) d\mathbf{r}, \tag{3}$$

$$\varepsilon = \frac{3}{2} T + \frac{1}{2} n_0 \int v(r) w(r) d\mathbf{r}. \tag{4}$$

These thermodynamic functions suffice, e.g., for studying shock waves in liquids.

The pair central potential $v(r)$ of simple liquids is usually approximated by certain functions allowing for the repulsion caused by the overlap of atomic orbitals at small r and the dispersion interaction leading to the attraction at large r. A hard-sphere potential

$$v_{\text{hs}} = \begin{cases} \infty, & r \le d \\ 0, & r > 0 \end{cases} \tag{5}$$

is widely used. The absence of attraction is its drawback, but then the Percus–Yevik integral equation [3] for the pair correlation function with this potential can be solved exactly [4, 5]. This solution is used as a basis in the perturbative treatment of the thermodynamic properties of fluids [6–8]. The well-known Lennard-Jones potential

$$v_{LD}(r) = 4\epsilon\left(\left(\frac{\sigma}{r}\right)^{12} - \left(\frac{\sigma}{r}\right)^{6}\right) \tag{6}$$

includes the dipole–dipole attraction at large r in nonpolar liquids, but its repulsion term has a nonphysical singularity at $r \longrightarrow 0$. The Kratzer potential

$$v_K(r) = 2\epsilon\left(\frac{1}{2}\left(\frac{\sigma}{r}\right)^2 - \frac{\sigma}{r}\right), \tag{7}$$

describes well the interaction in polar liquids at $r \longrightarrow \infty$, but it contains a term that also has a nonphysical singularity at $r \longrightarrow 0$. Indeed, the interatomic potential should behave at $r \longrightarrow 0$ as $v(r) \sim 1/r$. For example, the interaction energy of two hydrogen atoms at distances $r \ll a_B$ (a_B is the Bohr radius) can be written as

$$v_{\text{HH}}(r) = e^2/r + E_{\text{He}} - 2E_{\text{H}} + O(r), \tag{8}$$

where e is the electron charge and $E_{\text{He}} = -78.9$ eV and $E_{\text{H}} = -13.6$ eV are, respectively, the energies of helium and hydrogen atoms in the ground state.

In this work, the pair central potential of interatomic interaction in liquid is chosen in the form

$$v(r) = \epsilon \frac{p e^{-a\alpha r} - e^{-b\alpha r}}{\alpha r}, \tag{9}$$

where the parameter α has dimension of reciprocal length and ϵ is the energy parameter; p, a, and b are dimensionless numbers, with $a > b$ and $p > 1$. The inter-

action potentials of real atoms can be approximated by the appropriate choice of parameters in Eq. (9), which includes the asymptotic Coulomb repulsion at $r \longrightarrow 0$, the exchange repulsion decreasing exponentially with an increase in r, and the attraction at large r. By way of example, let us consider the potential

$$v(r) = \epsilon\frac{2e^{-2\alpha r} - e^{-\alpha r}}{\alpha r}. \quad (10)$$

Denote

$$v_1(r) = e^{-2\alpha r}/r, \quad v_2(r) = e^{-\alpha r}/r, \quad (11)$$

so that

$$v(r) = \frac{\epsilon}{\alpha}(2v_1(r) - v_2(r)). \quad (12)$$

It is particularly important that $v_1(r)$ and $v_2(r)$ are the Green's functions of equations

$$\Delta v_1(\mathbf{r}) - 4\alpha^2 v_1(\mathbf{r}) = -4\pi\delta(\mathbf{r}), \quad (13)$$

$$\Delta v_2(\mathbf{r}) - \alpha^2 v_2(\mathbf{r}) = -4\pi\delta(\mathbf{r}). \quad (14)$$

Let us introduce the functions

$$\varphi_1(\mathbf{r}) = \int n(\mathbf{r}')v_1(\mathbf{r} - \mathbf{r}')d\mathbf{r}', \quad (15)$$

$$\varphi_2(\mathbf{r}) = \int n(\mathbf{r}')v_2(\mathbf{r} - \mathbf{r}')d\mathbf{r}'. \quad (16)$$

It is convenient to introduce $1/\alpha$ as a length unit, $\alpha^3/4\pi$ as a number density unit, and α as a measurement unit for the functions φ_1 and φ_2. Taking into account that $v_1(r)$ and $v_2(r)$ obey Eqs. (13) and (14), one obtains for $\varphi_1(\mathbf{r})$ and $\varphi_2(\mathbf{r})$

$$\Delta\varphi_1(r) - 4\varphi_1(r) = -n(r), \quad (17)$$

$$\Delta\varphi_2(r) - \varphi_2(r) = -n(r), \quad (18)$$

where $n(r)$ is the particle number density at a distance r from the particle chosen as the origin. For the classical particles, $n(r)$ obeys the Boltzmann distribution

$$n(r) = \xi n_0 e^{-\epsilon\varphi(r)/\alpha T}, \quad (19)$$

where

$$\frac{\epsilon}{\alpha}\varphi(r) = \frac{\epsilon}{\alpha}\int n(\mathbf{r}')v(\mathbf{r} - \mathbf{r}')d\mathbf{r}' = \frac{\epsilon}{\alpha}(2\varphi_1(r) - \varphi_2(r)) \quad (20)$$

is the self-consistent potential energy of a particle situated at a distance r from the origin. Let us choose ϵ as the temperature unit and replace the unit of measurement of φ_1, φ_2, and φ by $\frac{4\pi n_0}{\alpha^3}\alpha = \frac{4\pi n_0}{\alpha^2}$. One finally has the following units of measurement: $1/\alpha$ for length; $\alpha^3/4\pi$ for number density; $4\pi n_0/\alpha^2$ for φ_1, φ_2, and φ; and ϵ for temperature. In these units, the system of ordinary differential equations for φ_1 and φ_2 is written as

$$\Delta\varphi_1 - 4\varphi_1 = -\xi e^{-\nu(2\varphi_1 - \varphi_2)}, \quad (21)$$

$$\Delta\varphi_2 - \varphi_2 = -\xi e^{-\nu(2\varphi_1 - \varphi_2)}. \quad (22)$$

In these equations,

$$\nu = 4\pi n_0/\alpha^3 T, \quad (23)$$

where Δ is the radial part of the Laplace operator in spherical coordinates, $\Delta = \frac{1}{r}\frac{\partial^2}{\partial r^2}r$. The parameter ξ in Eqs. (21) and (22) is determined from the condition that the particle concentration at $r \longrightarrow \infty$ is equal to the particle mean number density n_0; i.e.,

$$\xi e^{-\nu(2\varphi_1 - \varphi_2)} = 1 \quad (24)$$

at $r \longrightarrow \infty$. The functions $\varphi_1(r)$ and $\varphi_2(r)$ tend towards the following limiting values:

$$\varphi_{10} = \frac{1}{4}, \quad \varphi_{20} = 1. \quad (25)$$

Then,

$$\xi = e^{\nu(2\varphi_{10} - \varphi_{20})} = e^{-\nu/2}. \quad (26)$$

One finally arrives at the following system of ordinary differential equations for φ_1 and φ_2:

$$\Delta\varphi_1 - 4\varphi_1 = -e^{\nu(\varphi_2 - 2\varphi_1 - 1/2)}, \quad (27)$$

$$\Delta\varphi_2 - \varphi_2 = -e^{\nu(\varphi_2 - 2\varphi_1 - 1/2)}. \quad (28)$$

It is of interest to clarify how the functions φ_1 and φ_2 behave at large r. Let us write $\varphi_1 = \frac{1}{4} + \bar{\varphi}_1$ and $\varphi_2 = 1 + \bar{\varphi}_2$ and then linearize the system of Eqs. (27) and (28) at small $\bar{\varphi}_1$ and $\bar{\varphi}_2$. Introducing new functions

$$\bar{f}_1(r) = r\bar{\varphi}_1(r), \quad \bar{f}_2(r) = r\bar{\varphi}_2(r), \quad (29)$$

one obtains the system of equations

$$\bar{f}_1'' - (2\nu + 4)\bar{f}_1 + \nu\bar{f}_2 = 0, \quad (30)$$

$$\bar{f}_2'' - 2\nu\bar{f}_1 + (\nu - 1)\bar{f}_2 = 0, \quad (31)$$

or, after expressing $\bar{f}_2$ in terms of $\bar{f}_1$, the following linear equation for $\bar{f}_1$:

$$\bar{f}_1^{(4)} - (\nu + 5)\bar{f}_1'' - (2\nu - 4) = 0. \quad (32)$$

The roots q of its characteristic equation are

$$q_{1,2}^2 = \frac{1}{2}(\nu + 5 \pm \sqrt{(\nu + 5)^2 + 4(2\nu - 4)}). \quad (33)$$

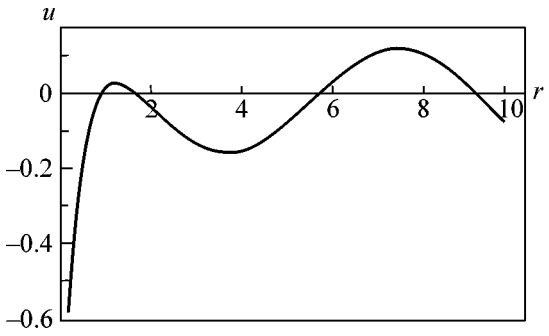

Fig. 1. The function $u(r)$ for $\nu = 6$.

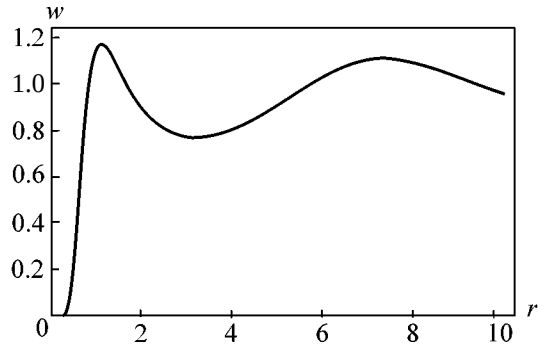

Fig. 2. The radial distribution function $w(r) = e^{\nu u(r)/r}$ ($\nu = 6$).

The discriminant $(\nu + 5)^2 + 4(2\nu - 4) = \nu^2 + 18\nu + 9 > 0$ for all $\nu > 0$. However, whereas $q_1^2 = \frac{1}{2}(\nu + 5 + \sqrt{(\nu + 5)^2 + 4(2\nu - 4)}) > 0$ for all ν, $q_2^2 = \frac{1}{2}(\nu + 5 - \sqrt{(\nu + 5)^2 + 4(2\nu - 4)}) > 0$ only for $\nu < 2$, while, at $\nu > 2$, $q_2^2 < 0$. This signifies that the asymptotic behavior of $\bar{f}_1$ and $\bar{f}_2$ at large r can be represented at $\nu < 2$ as a sum of two decaying exponentials, whereas for $\nu > 2$ one should add the oscillating solution $C_2\sin(\sqrt{-q_2^2}r) + C_3\cos(\sqrt{-q_2^2}r)$ to the exponentially decaying function $C_1\exp(-q_1 r)$. These solutions can naturally be attributed to the gaseous phase at $\nu < 2$ and to the condensed phase at $\nu > 2$; i.e., the liquid state is possible only for $\nu > 2$. Therefore, one can conclude from the analytic solution to the system of Eqs. (27) and (28) that at large r this model allows the phase transition to a liquid condensed phase. The equation for the condensation curve on the temperature–concentration coordinates reads $\nu = 2$.

To calculate the pair correlation function at an arbitrary r, it is necessary to solve the system of differential Eqs. (27) and (28). These equations should be complemented by the boundary conditions at $r \longrightarrow 0$. The potential v_{10} of a particle placed at the origin ($r = 0$) has the following form at $r \longrightarrow 0$:

$$v_{10} = e^{-2r}/r \approx 1/r - 2. \tag{34}$$

To this potential must be added the potential $\tilde{\varphi}_1$ created at the point $r = 0$ by the remaining particles. It will be calculated on the assumption that the concentration $n(r) = 0$ at $r \le d$ ($d < 1$) and $n(r) = n_0$ at $r > d$:

$$\tilde{\varphi}_1(0) = \int n(r)v_1(r)d\mathbf{r} = 4\pi n_0 e^{-2d}\frac{1}{4}(1 + 2d). \tag{35}$$

Similarly, one has at $r \longrightarrow 0$

$$v_{20} = \frac{e^{-r}}{r} \approx \frac{1}{r} - 1, \tag{36}$$

$$\tilde{\varphi}_2(0) = \int n(r)v_2(r)d\mathbf{r} = 4\pi n_0 e^{-d}(1 + d). \tag{37}$$

In the concentration units adopted in this work,

$$\begin{aligned} \tilde{\varphi}_1(0) &= \frac{1}{4}e^{-2d}(1 + 2d), \\ \tilde{\varphi}_2(0) &= e^{-d}(1 + d). \end{aligned} \tag{38}$$

Denote $\tilde{\varphi}_2(0) = c$. Then $\tilde{\varphi}_1(0) \approx c^2/4$, so that

$$\begin{aligned} \varphi_1(r) &\simeq 1/r - 2 + c^2/4, \\ \varphi_2(r) &\simeq 1/r - 1 + c. \end{aligned} \tag{39}$$

at $r \longrightarrow 0$.

To solve the system of Eqs. (27) and (28), let us pass to the functions

$$f_1(r) = r\varphi_1(r), \quad f_2(r) = r\varphi_2(r). \tag{40}$$

The system of equations for f_1 and f_2 reads

$$f_1'' - 4f_1 = -r\exp\left\{\nu\left(\frac{f_2 - 2f_1}{r} - \frac{1}{2}\right)\right\}, \tag{41}$$

$$f_2'' - f_2 = -r\exp\left\{\nu\left(\frac{f_2 - 2f_1}{r} - \frac{1}{2}\right)\right\}. \tag{42}$$

At $r \longrightarrow 0$,

$$\begin{aligned} f_1(r) &\simeq 1 + (c^2/4 - 2)r, \\ f_2(r) &\simeq 1 + (c - 1)r. \end{aligned} \tag{43}$$

The final system of equations can conveniently be written using the function

$$u(r) = f_2(r) - 2f_1(r) - \frac{1}{2}r. \tag{44}$$

Then, denoting $u'(r) = g(r)$ and $f_2'(r) = g_2(r)$, one arrives at the following system of ordinary differential equations:

$$u' = g, \quad g' = 4u - 3f_2 + r(2 + e^{\nu u/r}), \qquad f_2' = g_2, \quad g_2' = f_2 - re^{\nu u/r} \tag{45}$$

with the boundary conditions at $r \longrightarrow 0$

$$u(r) = -1 + \left(\frac{5}{2} + c - \frac{c^2}{2}\right)r, \quad g(r) = \frac{5}{2} + c - \frac{c^2}{2}, \qquad f_2(r) = 1 + (c-1)r, \quad g_2(r) = c - 1. \tag{46}$$

The appropriate choice of parameter c provides φ_1 and φ_2 approaching, respectively, φ_{10} and φ_{20} at $r \longrightarrow \infty$ (this corresponds to the sinusoidal asymptotic behavior of the function u). As an example, the function $u(r)$ is shown for $\nu = 6$ in Fig. 1. One can see that the function $u(r)$ behaves at large r like a sinusoid with a period equal to $2\pi/\sqrt{-q_2^2}$. The pair correlation function $w(r) = e^{\nu u(r)/r}$ is depicted in Fig. 2. Starting, e.g., at the coordinate of the second maximum, $w(r)$ is nicely described by its asymptotic expression at $r \longrightarrow \infty$, which can be written using the asymptotic form of $u(r)$:

$$u(r) = u(r_2)\cos(\sqrt{-q_2^2}(r - r_2)). \tag{47}$$

Therefore, instead of the integral equations that are commonly used for calculating the correlation function in fluids, we have derived a system of ordinary differential equations with boundary conditions, which can be solved numerically by standard methods. Moreover, we have obtained an analytical expression for the asymptotic behavior of the pair radial distribution function for large distances between atoms.

This work was supported by the Russian Foundation for Basic Research and the program for the Support of Leading Scientific Schools.

REFERENCES

1. L. D. Landau and E. M. Lifshitz, *Course of Theoretical Physics*, Vol. 5: *Statistical Physics* (Nauka, Moscow, 1976; Pergamon, Oxford, 1980).
2. R. Balescu, *Equilibrium and Nonequilibrium Statistical Mechanics* (Wiley, New York, 1975; Mir, Moscow, 1978).
3. J. K. Percus and G. J. Yevik, Phys. Rev. **110**, 1 (1958).
4. E. Thiele, J. Chem. Phys. **39**, 474 (1963).
5. M. S. Wertheim, Phys. Rev. Lett. **10**, 321 (1963).
6. J. D. Weeks, D. Chandler, and H. C. Andersen, J. Chem. Phys. **54**, 5237 (1971).
7. V. Verlet and J. J. Weis, Phys. Rev. A **5**, 939 (1972).
8. M. Banaszak, Y. C. Chiew, R. O'Lenick, and M. Radosz, J. Chem. Phys. **100**, 3803 (1994).

Translated by V. Sakun

JETP Letters, Vol. 74, No. 4, 2001, pp. 204–208. Translated from Pis'ma v Zhurnal Éksperimental'noĭ i Teoreticheskoĭ Fiziki, Vol. 74, No. 4, 2001, pp. 224–228.

On the Boundary Conditions to the Ginzburg–Landau Equations at the Interface of Two Superconductors with Different Transition Temperatures

E. A. Shapoval

All-Russia Research Institute of Metrological Service, Moscow, 117334 Russia

Received June 20, 2001; in final form, July 13, 2001

The generalized Wiener–Hopf method was used to derive, on the basis of the microscopic BCS theory of superconductivity, the effective boundary conditions to the Ginzburg–Landau equations at the interface of two (including uncommon) superconductors with different transition temperatures in the absence of reflection from the boundary. According to these conditions, the order parameter and its derivative undergo jumps at the interface. © *2001 MAIK "Nauka/Interperiodica".*

PACS numbers: 74.20.De; 74.20.Fg; 74.50.+r

The boundary conditions to the Ginzburg–Landau (GL) equations for common superconductors were deduced by de Gennes [1] and Zaĭtsev [2] on the basis of microscopic theory of superconductivity. The conditions at the boundary with vacuum (insulator) were obtained for anisotropic superconductors (including uncommon superconductors with an order parameter of *d* symmetry) by the author in [3, 4]. In recent years, a number of works have been published in which the conditions at the boundary of uncommon superconductors with insulator and metal were considered without taking account of the electron–electron interaction in the latter, i.e., with zero transition temperature [5–7]. In this work, the effective boundary conditions to the GL equations are derived for an arbitrary ratio between the superconducting transition temperatures of contacting metals, but in the absence of a potential barrier, allowing the integral equation of the problem to be exactly solved by the Wiener–Hopf (WH) method.

The effective boundary conditions to the GL equations are determined from the linearized equation for the order parameter $\Delta^*(\mathbf{p}_f, \mathbf{r})$ near the superconducting transition temperature:

$$\Delta^*(\mathbf{p}, \mathbf{r}) = \sum_{\mathbf{p}', \mathbf{p}''} V(\mathbf{p} - \mathbf{p}'') \times \int dr' \Delta(\mathbf{p}', \mathbf{r}') \pi T \sum_{\omega} \Phi_{\omega}(\mathbf{r}, \mathbf{p}''; \mathbf{r}', \mathbf{p}'), \quad (1)$$

where $\mathbf{p}$ is the Fermi momentum defining the anisotropy of the order parameter; the summation over $\mathbf{p}$ implies the integration over the Fermi surface with inclusion of the local density of states; V is the electron–electron interaction potential; ω are the Matsubara frequencies; and the functions Φ_ω are defined through the Green's functions in the normal state:

$$\Phi_{\omega}(\mathbf{r}, \mathbf{p}; \mathbf{r}', \mathbf{p}') = \sum_{\mathbf{q}, \mathbf{q}'} G_{\omega}(\mathbf{p}' + \mathbf{q}'/2, \mathbf{p} + \mathbf{q}/2) \times G_{-\omega}(-\mathbf{p}' + \mathbf{q}'/2, -\mathbf{p} + \mathbf{q}/2) \exp i(\mathbf{q}'\mathbf{r}' - \mathbf{q}\mathbf{r}). \quad (2)$$

The electron–electron interaction potential can be decomposed into a set of mutually orthogonal normalized functions at the Fermi surface:

$$V(\mathbf{p} - \mathbf{p}') = \sum_{\lambda} \lambda \phi_{\lambda}(\mathbf{p}) \phi_{\lambda}(\mathbf{p}'), \quad (3)$$

where positive λ's correspond to the attraction. In the weak-binding approximation, one can retain near the transition temperature only the leading term with maximal λ in this decomposition [8]; then the order parameter $\Delta^*(\mathbf{p}, \mathbf{r}) = \Delta(\mathbf{r})\phi_\lambda(\mathbf{p})$.

Let us assume that the interface is positioned at $x = 0$; in this case, all quantities in integral Eq. (1) depend only on the coordinate x, and the equation takes the form

$$\Delta(x) = \lambda(x)\nu(x) \int_{-\infty}^{\infty} K(x, x')\Delta(x')dx, \quad (4)$$

where ν is the density of states at the Fermi surface, and

$$K(x, x') = \pi T \sum_{\omega} \Phi_{\omega}(x, x'). \quad (5)$$

0021-3640/01/7404-0204$21.00 © 2001 MAIK "Nauka/Interperiodica"

For a homogeneous superconductor, Φ_ω depends only on the difference in coordinates,

$$\Phi_\omega(x-x') = \left\langle \frac{\phi^2(\mathbf{p})}{|v_x(\mathbf{p})|}\exp\left(-2\frac{|\omega||x-x'|}{|v_x(\mathbf{p})|}\right)\right\rangle, \quad (6)$$

where the angular brackets stand for the averaging over the Fermi surface and $v_x(\mathbf{p})$ is the projection of the Fermi velocity onto the x axis [3, 4].

In particular, for the isotropic Fermi surface one has

$$\Phi_\omega(x) = \frac{1}{v_f}\int_0^1 \exp\left(\frac{-2|\omega x|}{v_f\eta}\right)\frac{d\eta}{\eta}, \quad (7)$$

for the three-dimensional superconductor,

$$\Phi_\omega(x) = \frac{2}{\pi v_f}\int_0^{\pi/2} \exp\left(\frac{-2|\omega x|}{v_f\cos\theta}\right)\frac{\phi^2(\theta)}{\cos\theta}d\theta, \quad (8)$$

for the two-dimensional superconductor, and

$$\Phi_\omega(x) = \frac{1}{v_f}\exp\left(-\frac{2|\omega x|}{v_f}\right), \quad (9)$$

for the one-dimensional superconductor, where v_f is the Fermi velocity and $\phi^2(\theta) = 1$, $2\cos^2 2\theta$, and $2\sin^2 2\theta$ for the s, $d_{x^2-y^2}$ and d_{xy} pairing, respectively.

Assume that electrons are not reflected from the interface and that the effective electron–electron coupling constant is λ_1 to the right of interface ($x > 0$) and λ_2 to its left ($x < 0$), with $\lambda_1 > \lambda_2$. Then $T_{c1} > T_{c2}$ and the left metal is in the normal state at the temperature $T = T_{c1}$ at hand.

Let us introduce the Cooper-pair wave function that relates to the anomalous Green's function in the Gor'kov method as

$$f(\mathbf{r}) = T\sum_\omega F_\omega(\mathbf{r},\mathbf{r}) = \Delta^*(\mathbf{r})/\lambda(\mathbf{r}). \quad (10)$$

Contrary to the usual order parameter, this function can be nonzero in the normal metal with $\lambda = 0$ and account for the penetration of Cooper pairs from the neighboring superconductor. Using this function, Eq. (4) can be written in the form of the generalized WH equation

$$f(x) = \lambda_1\nu\int_0^\infty K(x-x')f(x')dx' + \lambda_2\nu\int_{-\infty}^0 K(x-x')f(x')dx'. \quad (11)$$

Representing the Cooper-pair function as the sum of two functions $f(x) = f^+(x) + f^-(x)$ which differ from zero to the right and left of the interface, respectively, and applying the Fourier transform, one obtains

$$(1-\lambda_1\nu K(k))f^+(k) + (1-\lambda_2\nu K(k))f^-(k) = 0. \quad (12)$$

The functions $f^\pm(q)$ are analytic, respectively, in the lower and upper half-plane of the complex plane q and, simultaneously, analytic in a certain common strip along the real axis, thereby satisfying the WH conditions.

Let us first consider the simple case of $\lambda_2 = 0$, for which Eq. (11) reduces to the usual WH equation. The effective boundary conditions can be found from the solution to this equation at $T_{c1} = T$ away from the interface. It is related to the coupling constant by the BCS equation

$$\ln(2\gamma\omega_D/\pi T) = 1/\lambda\nu. \quad (13)$$

The corresponding solution to the WH equation at $x > 0$ is $f^+(x) \propto b + x +$ terms decreasing exponentially at distances on the order of $\xi_0 = v_f/2\pi T$. The extrapolation length b determines the effective boundary conditions; it is given by the expression

$$\frac{b}{\xi_0} = \int_{-\infty}^\infty \left(\frac{2}{q^2} - \frac{R'(q)}{qR(q)}\right)\frac{dq}{2\pi}. \quad (14)$$

Here, $q = \xi_0 k$ is the dimensionless momentum and $R(q) = 1 - \lambda\nu K(q)$. This expression was obtained by Zaĭtsev [2] for the particular case of an isotropic three-dimensional superconductor. It will be derived below by a simple method. For the above symmetries of the order parameter, one finds, using Eq. (5):

$$\frac{R(q)}{\lambda\nu} = \frac{i}{2q}\ln\frac{\Gamma(1/2+iq/2)}{\Gamma(1/2-iq/2)} + \psi(1/2),$$

for the three-dimensional superconductor,

$$\frac{R(q)}{\lambda\nu} = \frac{2}{\pi}\int_0^{\pi/2}\phi^2(\theta)[\psi(1/2) - \mathrm{Re}\,\psi(1/2+iq\cos\theta/2)]d\theta, \quad (15)$$

for the two-dimensional superconductor, and

$$\frac{R(q)}{\lambda\nu} = \psi(1/2) - \mathrm{Re}\,\psi(1/2+iq/2)$$

for the one-dimensional superconductor.

Using Eq. (14), one can determine the extrapolation lengths for the superconductors of interest (in units of ξ_0): $b/\xi_0 = 0.916$, 0.754, 0.814, 0.696, and 0.620 for the one-dimensional, two-dimensional (s, $d_{x^2-y^2}$, and d_{xy}), and three-dimensional superconductors, respectively. An insignificant disparity with the Zaĭtsev result [2] for the three-dimensional superconductors may be explained by the vigorous development of computer engineering in the past decades.

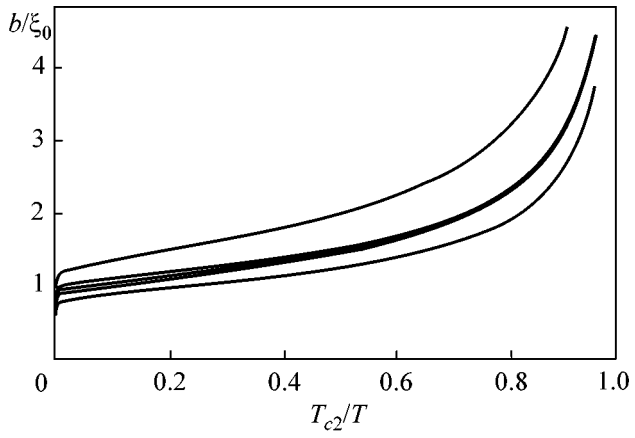

Fig. 1. Fractional extrapolation length b/ξ_0 as a function of the ratio of transition temperatures of the contacting superconductors. The curves are for (from the top to down) the one-dimensional, two-dimensional (d_{xy}, s, and $d_{x^2-y^2}$), and three-dimensional superconductors.

Let us now consider the case $\lambda_2 \neq 0$; i.e., the metal to the left of the interface is a superconductor with transition temperature $T_{c2} < T$. One can show that the corresponding expression for the extrapolation length given by the solution to the generalized WH equation (11) is similar to Eq. (14):

$$\frac{b}{\xi_0} = \int_{-\infty}^{\infty}\left(\frac{2}{q^2} - \frac{R'(q)}{qR(q)} + \frac{R_2'(q)}{qR_2(q)}\right)\frac{dq}{2\pi}, \tag{16}$$

where $R_2(q) = 1 - \nu\lambda_2 K(q) = 1 - (1 - R(q))\lambda_2/\lambda$. Equation (16) then takes the form

$$\frac{b}{\xi_0} = \int_{-\infty}^{\infty}\left[\frac{2}{q^2} - \frac{R'(q)}{q}\left(\frac{1}{R(q)} - \frac{1}{R(q) + \lambda\nu\ln(T/T_{c2})}\right)\right]\frac{dq}{2\pi}. \tag{17}$$

It was taken into account that

$$1/\lambda_2\nu - 1/\lambda\nu = \ln(T/T_{c2}). \tag{18}$$

The dependences of the reduced extrapolation lengths on T_{c2}/T are shown in Fig. 1 for the superconductors of different symmetry considered in this work. On the whole, they are quite similar. A comparison with the results obtained above for $\lambda_2 = 0$ shows that the extrapolation length increases dramatically even at small $T_{c2} \ll T$, indicating that the electron–electron interaction in the second metal must be taken into account even at low T_{c2}. It follows from Eq. (17) that at $T_{c2} \ll T$ the extrapolation length is $b(T_{c2}/T) = b(0) + b_1/\ln(T/T_{c2})$, where the coefficient b_1 is given by

$$\frac{b_1}{\xi_0} = \frac{1}{\lambda\nu}\int_{-\infty}^{\infty}\frac{R'(q)dq}{2\pi q}. \tag{19}$$

For the superconductors considered, this coefficient equals 1.234, 0.785, 0.732, 0.837, and 0.671 for the one-dimensional, two-dimensional (s, $d_{x^2-y^2}$, and d_{xy}), and three-dimensional superconductors, respectively.

The extrapolation length increases as $T_{c2} \longrightarrow T$. The penetration depth in the second superconductor increases likewise. If the transition temperature T_{c2} of the second superconductor is close to (but lower than) the temperature T ($0 < T - T_{c2} \ll T$), then, as it follows from Eq. (17), the extrapolation length for the first superconductor ($x > 0$) becomes analogous to the temperature-dependent coherence length entering the GL equations but defined here by the transition temperature of the second superconductor,

$$b = \sqrt{\frac{7\zeta(3)}{4D(1 - T_{c2}/T)}}\xi_0 = \xi(|\tau_2|), \tag{20}$$

where D is the system dimensionality. In the GL approximation (i.e., at distances $|x| \gg \xi_0$), the same quantity defines the penetration depth in the left superconductor at $x < 0$: $f(x) \propto \exp(x/b)$+ terms decreasing exponentially at distances on the order of ξ_0.

Let us now consider the case where both metals are in the superconducting state and the GL equations apply: $0 < \tau_{1,2} = \ln(T_{1,2}/T) \ll 1$. To solve WH Eq. (12), it is convenient to represent the kernel $K(q)$ in the form

$$K(q) = \sum_{n=1}^{N}\frac{b_n}{q^2 + a_n^2}, \quad K(0) = \sum_{n=1}^{N}\frac{b_n}{a_n^2} = \frac{1}{\nu\lambda}. \tag{21}$$

One has for $\lambda_{1,2} > \lambda$:

$$R_{1,2}(q) = 1 - \nu\lambda_{1,2}K(q) = (q^2 - \alpha_{1,2}^2)\frac{\prod_{n=1}^{N-1}(q^2 + B_n^{(1,2)^2})}{\prod_{n=1}^{N}(q^2 + a_n^2)}, \tag{22}$$

where $B_n^{(1,2)} \geq 1$ and $\alpha_{1,2} \ll 1$. The functions $R_{1,2}(q)$ can easily be factorized, giving

$$(q^2 - \alpha_1^2)\prod_{n=1}^{N-1}\frac{q - iB_n^{(1)}}{q - iB_n^{(2)}}f^+(q) = -(q^2 - \alpha_2^2)\prod_{n=1}^{N-1}\frac{q + iB_n^{(2)}}{q + iB_n^{(1)}}f^-(q) \propto 1; q. \tag{23}$$

As a result, one obtains two linearly independent solutions in the momentum representation, from which one finds, after passing to the coordinate representation, that, in particular, both solutions for the Cooper-pair wave function $f(x) = \Delta(x)/\lambda(x)$ are continuous at the interface ($x = 0$), with the first solution ["odd," because it becomes odd for $\lambda_1 = \lambda_2$] being $f_1(0) = 0$ and the second solution ["even," $f_2(x) = \partial f_1(x)/\partial x$] being nonzero at $x = 0$. An analogous result was obtained by de Gennes for "dirty" superconductors [1]. As to the clean superconductors considered in this work, the effective boundary conditions for the GL equations are determined by the behavior of $f(x)$ and $\Delta(x)$ at distances $\xi_0 \ll x \ll \xi(T)$ [1, 2], as is schematically illustrated in Fig. 2.

In the region where the terms corresponding to the poles at $\pm iB_n^{(1,2)}$ and decreasing exponentially at distances on the order of ξ_0 vanish, the solutions to the WH equation have the form

$$f_1^{\pm}(x) = \left(\prod_{n=1}^{N-1}\frac{B_n^{(1)}B_n^{(2)} + \alpha_{1,2}^2 + i\alpha_{1,2}(B_n^{(2)} - B_n^{(1)})}{B_n^{(1,2)^2} + \alpha_{1,2}^2}\right)$$

$$\times \frac{\exp(i\alpha_{1,2}x)}{2i\alpha_{1,2}} + \text{k.c.} \approx \left(\prod_{n=1}^{N-1}\frac{B_n^{(2,1)}}{B_n^{(1,2)}}\right)\Bigg[(1 + O(\alpha^4)) \times \frac{\sin\alpha_{1,2}x}{\alpha_{1,2}} + \alpha_{1,2}S\cos\alpha_{1,2}x\Bigg]; \quad (24)$$

$$|x| \gg \xi_0; \quad f_2^{\pm}(x) = \frac{\partial}{\partial x}f_1^{\pm}(x).$$

For simplicity, the coordinate x in Eq. (24) is expressed in units of coherence length ξ_0, so that $\alpha_{1,2} = \xi_0/\xi(\tau_{1,2}) = \sqrt{4D\tau_{1,2}/7\zeta(3)}$, and

$$S = \sum_{n=1}^{N-1}\left(\frac{1}{B_n^{(2)}} - \frac{1}{B_n^{(1)}}\right) = (\tau_1 - \tau_2)\int_{-\infty}^{\infty}\frac{dq}{2\pi}\left[\frac{R'(q)}{qR^2(q)} - \frac{8D}{7\zeta(3)q^4}\right]. \quad (25)$$

This result was also used in estimating the coefficient of sine in Eq. (24). The integral in Eq. (25) is equal to 0.030 for the one-dimensional superconductors; 0.056, 0.076, and 0.085 for the two-dimensional $d_{x^2-y^2}$, s, and d_{xy} superconductors, respectively; and 0.126 for the three-dimensional superconductors.

It follows from the definitions of $R_{1,2}(q)$ (22) and $\tau_{1,2} = 1/\nu\lambda - 1/\nu\lambda_{1,2}$ that

$$\frac{R_1(0)}{R_2(0)} = \frac{1 - \lambda_1/\lambda}{1 - \lambda_2/\lambda} = \frac{\lambda_1\tau_1}{\lambda_2\tau_2} = \frac{\alpha_1^2}{\alpha_2^2}\prod_{n=1}^{2N-1}\frac{B_n^{(1)^2}}{B_n^{(2)^2}}. \quad (26)$$

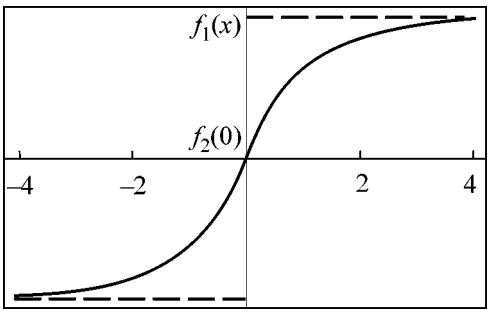

Fig. 2. Solid line is the result of microscopic analysis of the behavior of Cooper-pair wave function $f_2(x) = \partial f_1(x)/\partial x$ near the interface [$|x| \ll \xi(T)$] between two superconductors with different transition temperatures. The dashed straight lines correspond to the asymptotic behavior of the solid line at $|x| \gg \xi_0$; it determines the effective boundary conditions to the macroscopic GL equations.

Then

$$\prod_{n=1}^{N-1}\frac{B_n^{(1)}}{B_n^{(2)}} = \sqrt{\frac{\lambda_1\tau_1/\alpha_1^2}{\lambda_2\tau_2/\alpha_2^2}} = \sqrt{\frac{\lambda_1(1 - C\tau_1)}{\lambda_2(1 - C\tau_2)}}. \quad (27)$$

Equation (27) is obtained using the second term in the momentum expansion of $K(q)$, which gives

$$\tau_{1,2} = \frac{7\zeta(3)}{4D}\alpha_{1,2}^2 - c\frac{31\zeta(5)}{32}\alpha_{1,2}^4, \quad (28)$$

where $c = 2/5$, 3/4, 7/8, 5/8, and 2 for the one-dimensional, two-dimensional (s, $d_{x^2-y^2}$, and d_{xy}), and three-dimensional superconductors, respectively. This gives $C = 31\zeta(5)/49\zeta^2(3)cD^2/2$. Neglect of this term leads to the trivial result: the order parameters and their derivatives are equal on both sides of the interface, as if $\tau_1 = \tau_2$. On the other hand, if the metals on both sides of the boundary are different, then the unavoidable electron reflection from the surface leads to the boundary conditions, for which the correction for the difference in the transition temperatures proves to be negligible in many cases.

Taking into account that the Cooper-pair wave function is related to the order parameter by Eq. (10), one can formulate the desired boundary conditions to the GL equations as follows:

$$(1 - C\tau_1)\Delta_1 = (1 - C\tau_2)\Delta_2; \quad (1 - C\tau_1)\Delta_1' = (1 - C\tau_2)\Delta_2'. \quad (29)$$

In a magnetic field, the second boundary condition can be obtained in the usual way by substituting $\partial/\partial x \longrightarrow \mathbf{n}(\nabla + 2ie\mathbf{A})$, where $\mathbf{n}$ is the normal to the interface. It follows from Eq. (29) that, even in the absence of reflection from the interface, the effective order param-

eter and its derivative undergo jumps proportional to the difference in the transition temperatures:

$$\frac{\Delta_1 - \Delta_2}{\Delta_1 + \Delta_2} = C\frac{\tau_1 - \tau_2}{2}; \quad \frac{\Delta_1' - \Delta_2'}{\Delta_1' + \Delta_2'} = C\frac{\tau_1 - \tau_2}{2}. \quad (30)$$

The above boundary conditions are also valid for $T_{c2} < T < T_{c1}$, provided that the GL equations apply to the second superconductor ($|1 - T_{c2}/T| \ll 1$); in this case, however, τ_2 is negative.

The results obtained in this work are consistent with the continuity condition for a current passing through the interface. In the general case, the boundary conditions at the interface of two superconductors can be written as

$$\Delta_1 = M_{11}\Delta_2 + M_{12}\Delta_2', \quad \Delta_1' = M_{21}\Delta_2 + M_{22}\Delta_2'. \quad (31)$$

If the metals on both sides are identical, except for their transition temperatures, then the calculation of a current passing though the interface shows that, for an arbitrary transmission coefficient

$$M_{11}M_{22} - M_{12}M_{21} = \sqrt{\frac{1 + C\tau_1}{1 + C\tau_2}} \quad (32)$$

to the terms on the order of τ which are negligible in other problems. At $\tau_1 = \tau_2$, i.e., for the identical transition temperatures, this result reduces to the well-known de Gennes result presented in [1a].

I am grateful to R.O. Zaĭtsev for discussion and valuable remarks. This work was supported by the Scientific Council of the direction “Superconductivity” and by the State Scientific and Technical Program “Topics in Physics of Condensed Media.”

REFERENCES

1. P. G. de Gennes, Rev. Mod. Phys. **36**, 225 (1964); P. G. de Gennes, *Superconductivity of Metals and Alloys* (Benjamin, New York, 1966; Mir, Moscow, 1968).
2. R. O. Zaĭtsev, Zh. Éksp. Teor. Fiz. **48**, 664 (1965) [Sov. Phys. JETP **21** (1965)]; Zh. Éksp. Teor. Fiz. **48**, 1759 (1965) [Sov. Phys. JETP **21**, 1178 (1965)].
3. E. A. Shapoval, Zh. Éksp. Teor. Fiz. **88**, 1073 (1985) [Sov. Phys. JETP **61**, 630 (1985)].
4. E. A. Shapoval, Pis’ma Zh. Éksp. Teor. Fiz. **64**, 350 (1996) [JETP Lett. **64**, 381 (1996)].
5. M. Alber, B. Bauml, R. Ernst, *et al.*, Phys. Rev. B **53**, 5863 (1996).
6. D. F. Agterberg, J. Phys.: Condens. Matter **9**, 7435 (1997).
7. J. Mannhaft and H. Hilgenkamp, Physica C (Amsterdam) **317–318**, 383 (1999).
8. V. L. Pokrovskiĭ, Zh. Éksp. Teor. Fiz. **40**, 641 (1961) [Sov. Phys. JETP **13**, 447 (1961)].

Translated by V. Sakun

JETP Letters, Vol. 74, No. 4, 2001, pp. 209–212. Translated from Pis'ma v Zhurnal Éksperimental'noĭ i Teoreticheskoĭ Fiziki, Vol. 74, No. 4, 2001, pp. 229–233.

Coulomb Oscillations of the Ballistic Conductance in a Quasi-One-Dimensional Quantum Dot

V. A. Tkachenko[1]*, D. G. Baksheyev[1], O. A. Tkachenko[1,2], and C.-T. Liang[3]

[1] *Institute of Semiconductor Physics, Siberian Division, Russian Academy of Sciences, Novosibirsk, 630090 Russia*

[2] *Novosibirsk State University, Novosibirsk, 630090 Russia*

[3] *Department of Physics, National Taiwan University, 106 Taipei, Taiwan*

* *e-mail: vtkach@isp.nsc.ru*

Received July 16, 2001

It is demonstrated that localized states of an open quasi-one-dimensional quantum dot can be charged by the Coulomb blockade mechanism. A new effect—Coulomb oscillations of the ballistic conductance—is observed because of the high sensitivity of the ballistic current to single-electron variations of the self-consistent potential of the dot. The model proposed explains experimental results [C.-T. Liang, M. Y. Simmons, C. G. Smith, *et al.*, Phys. Rev. Lett. **81**, 3507 (1998)]. © *2001 MAIK "Nauka/Interperiodica".*

PACS numbers: 73.21.La; 73.23.Ad

It is known that a lateral quantum dot with a gate-controlled inlet/outlet is the most suitable system for studying the transition between the Coulomb blockade [1–3] and quantum ballistic [4–6] regimes. Initially, the single-electron charging effects were observed in the low-conductance limit ($G < e^2/h$) [3, 6], that is, in the case of weak coupling between the dot and the electron reservoirs, which corresponded to the orthodox Coulomb blockade theory [1, 2]. The possibility of dot charging in the open regime has been studied theoretically, and it has been predicted that the effect is weak or is even absent [7–9]. However, the case when scattering between one-dimensional subbands is suppressed and ballistic transport through the quantum dot is one-dimensional has not been considered in these articles. In this work, we will show that the charging of localized states of a quasi-one-dimensional dot is possible even when the background conductance comprises several quanta e^2/h. In this case, a new effect—Coulomb oscillations of the ballistic conductance—can be observed instead of sharp peaks of sequential tunneling current. A simple modification of the Landauer formula and the Coulomb blockade theory is proposed for the description of the effect. The model proposed is used for interpreting experimental results: frequent oscillations of the quantum dot conductance were observed in the wide range $0 < G < 6e^2/h$ in a zero magnetic field [10].

A quasi-one-dimensional dot can be considered as a section of a quantum wire with a two-barrier potential $U(x, y) \approx V(x) + \frac{1}{2} m^*(\omega^2 y^2)$, which allows separation of variables in the Schrödinger equation. Then, the motion of electrons in one-dimensional subbands $E_i(x) = V(x) + \left(\frac{1}{2} + i\right)\hbar\omega$ is independent, and the quantization with respect to x is found from the condition that the potential $V(x)$ in the central region of the dot has the form $\frac{1}{2} m^*(\Omega^2 x^2)$. In the case of ballistic transport, the quasi-levels of this quantization are revealed as broad resonances of the Fabry–Perot interference [11, 12]. In addition, there are many localized states of the closed subbands at the Fermi level of the reservoirs (Fig. 1). These states are hardly revealed in resonance scattering, because their lifetime is large. However, these states can trap an electron and release it back to the reservoirs, changing the dot charge in a discrete way because of tunneling through the effective barrier of the residual intersubband mixing. The tunnel resistances of such barriers are high ($R_{1,2} > h/e^2$), and the quantum charge fluctuations of localized states at $G > 2e^2/h$ are suppressed. Thus, the quasi-one-dimensional nature of the open dot provides the possibility of charging localized states through the mechanism of Coulomb blockade of sequential tunneling [1]. In the case of suppressed mixing of the current-carrying and localized states, the charging current is small for the Coulomb oscillations to be observed in it. However, charging causes single-electron variations of the electrostatic potential of the dot, and these variations, in accordance with the Landauer formula, will result in a change in ballistic conductance. That is, Coulomb oscillations following the number of electrons in the quantum dot

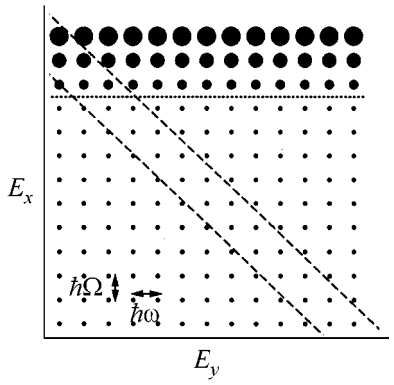

Fig. 1. Schematic diagram of a single-particle spectrum of a quasi-one-dimensional dot. E_x and E_y are the energy components along and across the dot. Columns correspond to one-dimensional subbands. The range of the total energy E corresponding to ballistic transport is singled out by dashed lines. The boundary between the localized and delocalized states is denoted by dots.

will appear against the background of the broad Fabry–Perot resonances.

Actually, the system of localized states of the quantum dot resides in one of the several states of electrostatic equilibrium between tunneling events. In the first approximation, the localized states form one structureless Coulomb island. Let P_n be the probability that an island contains n electrons. The stationary distributions P_n are found from the principle of detailed balance and the Fermi golden rule for the tunneling rate through effective barriers [1]. In our case, for the resistance of these barriers, $R_1 = R_2 = R$, it is only known that $R > h/e^2$; however, under this assumption, the P_n distribution is determined almost unambiguously. The charging current of localized states is proportional to R, but it is small in comparison with the ballistic current. The description of the ballistic current requires that averaging over the charge states be introduced into the Landauer formula, because the potential of the dot $U_n(x, y)$, which determines its penetrability, changes at each sequential tunneling event

$$G = \frac{2e^2}{h}\sum_n P_n \int \sum_i T_i(E, U_n) F(E - E_F) dE, \qquad (1)$$

where the function $F(E) = (1/4k_BT)\mathrm{sech}^2(E/2k_BT)$ takes into account the thermal spread in the energies E of the incident particles. Because of the quasi-one-dimensional nature of the system, all the contributions from higher subbands are expressed through the transmission coefficient for the zero subband $T_i = T_0(E - i\hbar\omega, U_n)$. The states over which the averaging in Eq. (1) is performed are characterized by the difference eV_b between the Fermi levels of the Coulomb island and the reservoirs

$$(C_1 + C_2 + C_g)V_b = ne + C_gV_g + q_0, \qquad (2)$$

where C_1, C_2, and C_g are the dot capacitance with respect to the reservoirs and the gate, n is the number of electrons that belong to the localized states, V_g is the gate voltage, and q_0 is the dot polarization charge, which determines the phase of Coulomb oscillations. In the Coulomb blockade theory [1], q_0 is considered to be constant, and it describes the interaction of the closed dot charge with uncontrolled charges and dipoles of the surrounding insulator. In the case of an open system, the Coulomb blockade theory should be modified, because the charge q_0 becomes a variable parameter and depends on the self-consistent variations of V_b and the charge belonging to the delocalized states of the dot (Fabry–Perot resonances). For simplicity, let us define q_0 as the charge of the open one-dimensional subbands of the dot in the quasi-classical approximation

$$q_0 = \frac{2e}{\hbar\Omega}\sum_i \frac{\Delta E_i}{1 - \exp(-\Delta E_i/k_BT)}, \qquad (3)$$

where ΔE_i is the position of the ith subband bottom at the center of the barrier in reference to the Fermi level of the reservoirs E_F. The denominator takes into account the possibility of a thermally activated electron transition to a subband when $\Delta E_i < 0$. The distance $\hbar\Omega$ between the quasi-discrete levels of the longitudinal motion in the dot is considered to be constant (Fig. 1), and the maximal charge on a quasi-level equals $2e$. In order to calculate q_0, we will use the semiempirical approximation of the dependence $\Delta E_i(V_b, V_g)$

$$\Delta E_i = -\frac{eV_b}{2} + \hbar\omega_0 \frac{(V_g - V_{g0})/\delta V_g - i}{(V_g - V_{g0})/\Delta V_g + 1}. \qquad (4)$$

The first term in this equation reflects the decrease of $eV_b/2$ in the potential at the center of the barrier under the action of the voltage V_b. The factor $\hbar\omega_0$ corresponds to the onset of the filling of the zero subband. The numerator of the fraction takes into account the assumption that the subbands are opened with an equal step δV_g, starting with V_{g0}, which is a common assumption for quasi-one-dimensional channels. The denominator reflects the fact that the distance between the one-dimensional subbands $\hbar\omega$ decreases by one-half in a certain interval ΔV_g. It is implied that V_g determines the value of $\hbar\omega$ and hardly affects the potential profile along the dot [11]. Equations (3) and (4), introduced above, close the description of quantum dot electrostatics and allow one to find P_n.

Several conclusions can be made from the proposed model. Below the threshold of the zero subband opening, the quantum dot is in the closed state, and its charge is quantized with a step of e with respect to C_gV_g. According to Eq. (2), this gives a saw-toothed dependence $e\bar{V}_b(C_gV_g)$ with the amplitude in the limits of the charging energy $E_Q = e^2/2C_\Sigma$, $C_\Sigma = C_1 + C_2 + C_g$. For states with N open subbands, which are separated

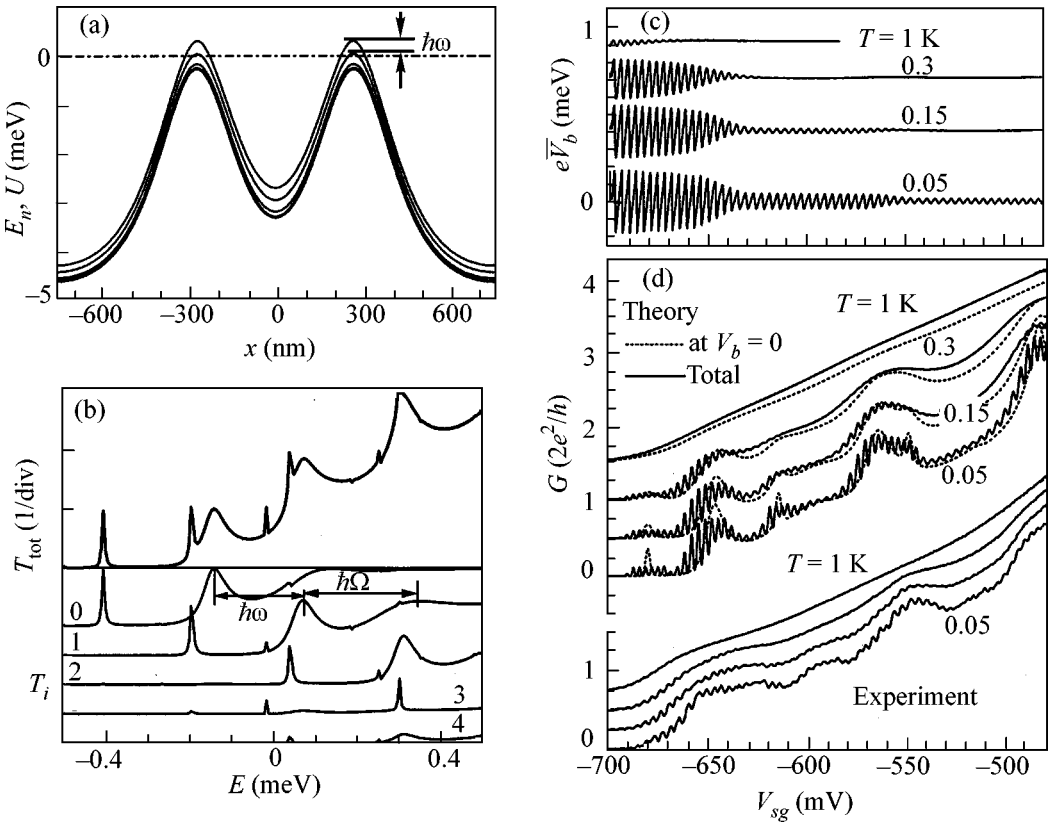

Fig. 2. Modeling of single-electron charging and Coulomb oscillations of the ballistic conductance in a quasi-one-dimensional quantum dot. Parameters of the model: $C_1 = C_2 = 150$ aF, $C_g = 44$ aF, $C_{open} = 1000$ aF, $\hbar\omega_0 = 0.5$ meV, $V_{g0} = -640$ mV, $\Delta V_g = 2\delta V_g = 170$ mV. (a) Longitudinal potential $U(x, y = 0)$ and the first three one-dimensional subbands $E_i(x)$ obtained at some gate voltages by calculating the three-dimensional electrostatics. (b) Total transmission coefficient as a function of the energy of incident particles and the contributions from 0–4 subbands for the situation in (a). (c) Saw-toothed dependence of the dot–reservoirs voltage on the gate voltage. (d) Calculated and measured conductance of the dot. Curves for different temperatures are displaced along the vertical axis. The dotted lines show the conductance without allowance made for single-electron oscillations of the dot potential ($V_b = 0$).

according to the gate voltage, the capacitances of the open subband states $C_{open} = e^2/\hbar\Omega$ are summed up according to Eq. (3), and $q_0 = -NV_bC_{open}$. Substituting this equation into Eq. (2) gives a stepwise renormalization of the effective charging energy $E_{Q_{eff}} = e^2/2(C_\Sigma + NC_{open})$. Thus, the oscillation amplitude $e\bar{V}_b$ and the critical temperature $k_BT_c = E_{Q_{eff}}$ (the temperature at which the charge quantization of the localized states disappears and the common Fermi level is settled in the entire system) decrease with increasing N. The oscillations of eV_b in the open regime indicate that the Fermi levels of the electrons delocalized and localized in the dot differ from each other. In order to enhance the effect and to create a ballistic single-electron transistor, the longitudinal dimension of a quasi-one-dimensional dot must be decreased, which will lead to an increase in $\hbar\Omega$ and a decrease in the capacitance C_{open}. Note that the highest sensitivity of $T_i(E)$ to variations in the potential relates to the instants of the opening of the subsequent one-dimensional subbands, when one should expect the largest Coulomb oscillations of the ballistic conductance. Because these oscillations are the result of a continuous transformation of the saw and the smoothed function $\bar{V}_b(V_g)$ according to Eq. (1), they will be more diffuse in shape than the common sharp peaks of the Coulomb blockade of the sequential tunneling current. We believe that the charging of quantum dots [3, 6] is not commonly observed in the open regime because of the strong intermode mixing of one-dimensional subbands. Because of this mixing, the localized states with energies higher than the barrier heights transform to the decaying states. These states are revealed in the transmission coefficient as Fano resonances [11], and they cannot be already assigned to particular subbands.

Let us use the proposed approach for modeling the conductance of a new type of quantum dot created by a two-layer system of metallic gates in an ultraclean channel of a GaAs/AlGaAs heterojunction [10]. The split gate lying on the semiconductor surface forms a one-dimensional channel, and three narrow continuous

finger gates separated from the lower gate by a resist (PMMA) layer and aligned across the channel create barriers between the quantum dot and the reservoirs. Continuous periodic oscillations on the gate voltage were observed in this device upon variations of the background conductance in the range $0 < G < 6e^2/h$ (the lower part of Fig. 2). Based on calculating a three-dimensional electrostatic potential and solving the problem of two-dimensional scattering [11], we have found that the main distinction of this device from the others is its quasi-one-dimensionality, that is, the suppression of mixing of one-dimensional subbands (Figs. 2a, 2b). By determining the dot capacitance with respect to the gates and reservoirs with a two-dimensional electron gas, we have confirmed that the period of oscillations corresponds to one electron added to the dot. Below, when modeling the conductance, we will use the values of C_1, C_2, and C_g capacitances and also $\hbar\Omega$ and $\hbar\omega$ quanta calculated in [11] for the quantum dot discussed here.

Figures 2c and 2d present the dependences of the average dot–reservoirs voltage $\bar{V}_b(V_g)$ and the conductance $G(V_g)$ for various temperatures. It is evident that the entire working range of split-gate voltages at T = 0.05 K is filled with single-electron oscillations of $\bar{V}_b(V_g)$ and $G(V_g)$. The amplitude of $\bar{V}_b(V_g)$ oscillations decreases in a stepwise manner with the opening of new one-dimensional subbands (Fig. 2c). The distance $\hbar\omega$ between one-dimensional subbands in this device (Fig. 2a) is comparable with the charging energy $\hbar\omega \approx E_Q = 0.2$ meV. Therefore, the variations of V_b that accompany the events of electron tunneling through localized states of the closed subbands must produce drastic changes in the transmission coefficient (Fig. 2d). As a result, Coulomb oscillations of the ballistic current appear, which are especially pronounced in the vicinity of large-scale singularities of resonance transmission. In order to simplify calculations by Eq. (1), we used the approximation $T_i(E, U_n) \approx T_0(E - \Delta E_i)$ and took the numerical dependence obtained at a certain characteristic $U(x, y)$ as $T_0(E)$ (Fig. 2b). The presence of factors providing the nonthermal smoothing of saw teeth in $\bar{V}_b(V_g)$, narrow resonance singularities in $G(V_g, V_b = 0)$, and Coulomb oscillations of the ballistic conductance was taken into account by additional uniform smoothing of the final curves with respect to the running average. The resulting overall picture is close to that observed experimentally (the lower part of Fig. 2d). The calculation reproduces the essential features of the actual behavior of the background and oscillations upon variations of the gate voltage V_g and temperature T. It is necessary to emphasize that, even at $G < e^2/h$, oscillations are revealed in the ballistic conductance rather than the sequential tunneling current, which has been taken into account in the calculations, but small. Note that a similar effect was already observed in a system of a quantum dot and a one-dimensional channel arranged in parallel and coupled by only electrostatic interaction [13]. The one-dimensional channel at $G < e^2/h$ was used as a detector measuring variations of the electrostatic potential caused by the single-electron charging processes in the quantum dot. In this case, it turned out that the detector signal continued to demonstrate single-electron oscillations even when the conventional Coulomb peaks of the sequential tunneling current through the quantum dot became too small for measurements.

In conclusion, we have shown that Coulomb oscillations of the ballistic conductance can be observed in a quasi-one-dimensional quantum dot, which are predicted by a simple modification of the Coulomb blockade theory and the Landauer formula. The reason for oscillations is the response of the transmission coefficient of ballistic electrons to variations of the electrostatic potential of the dot caused by the single-electron charging of localized states. It has been found that the oscillations of this type can embrace the range from the threshold to several conductance quanta with a stepwise decrease in the critical temperature on the opening of new subbands.

The authors are grateful to Z.D. Kvon for discussion. This work was supported by the program "Physics of Solid-State Nanostructures" (project no. 98-1102), the program "Micro- and Nanoelectronics" (project no. 02.04.5.1) and the program "Universities of Russia–Basic Research" (1994).

REFERENCES

1. K. K. Likharev, IBM J. Res. Dev. **32**, 144 (1988).
2. L. I. Glazman and R. I. Shekhter, J. Phys.: Condens. Matter **1**, 5811 (1989).
3. U. Meirav, M. A. Kastner, and S. J. Wind, Phys. Rev. Lett. **65**, 771 (1990).
4. R. Landauer, in *Localization, Interaction, and Transport Phenomena*, Ed. by G. Bergramm *et al.* (Springer-Verlag, Berlin, 1985).
5. D. A. Wharam *et al.*, J. Phys. C **21**, L209 (1988); B. J. van Wees *et al.*, Phys. Rev. Lett. **60**, 848 (1988).
6. C. G. Smith *et al.*, J. Phys. C **21**, L893 (1988).
7. K. A. Matveev, Phys. Rev. B **51**, 1743 (1995).
8. Y. V. Nazarov, Phys. Rev. Lett. **82**, 1245 (1999).
9. I. L. Aleiner and L. I. Glazman, Phys. Rev. B **57**, 9608 (1998).
10. C.-T. Liang, M. Y. Simmons, C. G. Smith, *et al.*, Phys. Rev. Lett. **81**, 3507 (1998).
11. D. G. Baksheyev, O. A. Tkachenko, and V. A. Tkachenko, Physica E (Amsterdam) **6**, 414 (2000).
12. Z. D. Kvon, L. V. Litvin, V. A. Tkachenko, and A. L. Aseev, Usp. Fiz. Nauk **169**, 471 (1999).
13. J. Cooper, C. G. Smith, D. A. Ritchie, *et al.*, Physica E (Amsterdam) **6**, 457 (2000).

Translated by A. Bagatur'yants

JETP Letters, Vol. 74, No. 4, 2001, pp. 213–215. Translated from Pis'ma v Zhurnal Éksperimental'noĭ i Teoreticheskoĭ Fiziki, Vol. 74, No. 4, 2001, pp. 234–236.

Formation of Submicron Cylindrical Structures at Silicon Surface Exposed to a Compression Plasma Flow

V. V. Uglov[1]*, V. M. Anishchik[1], V. V. Astashynski[1], V. M. Astashynski[2], S. I. Ananin[2], V. V. Askerko[2], E. A. Kostyukevich[2], A. M. Kuz'mitski[2], N. T. Kvasov[3], and A. L. Danilyuk[3]**

[1] *Belarussian State University, ul. Leningradskaya 14, Minsk, 220080 Belarus*
** e-mail: uglov@phys.bsu.unibel.by*
[2] *Institute of Molecular and Atomic Physics, National Academy of Sciences of Belarus, 70 Fkaryna Avenue, Minsk, 220072 Belarus*
*** e-mail: ast@imaph.bas-net.by*
[3] *Belarussian State University of Informatics and Radioelectronics, ul. P. Brovki 6, Minsk, Belarus*

Received July 16, 2001

Submicron-sized cylindrical structures were obtained at the surface of silicon single crystal exposed to a compression plasma flow. A periodic structure formed by channels oriented normally to the surface was observed inside the modified surface layer. The period of the structure corresponded to the spacing of the surface formations. © *2001 MAIK "Nauka/Interperiodica"*.

PACS numbers: 52.40.Hf; 79.20.Rf; 52.77.Bn; 68.35.Bs

Introduction. At present, the formation of submicron- and nano-sized structures of various compounds is being intensively studied, because their use can open up a qualitatively new stage in the development of microelectronics [1–4]. The formation of such structures in silicon is of prime interest because of its widespread use in microelectronics. However, despite the great diversity of the existing (chemical, laser, and plasma) methods, the cylindrical structures failed to be formed in silicon so far [4].

This work reports the results of studying the structural modification of a silicon surface under the action of a quasistationary compression plasma flow. Such flows are obtained using quasistationary plasma accelerators of the magnetoplasma compressor (MPC) type [5]. The advantages of the MPC over the other accelerator types are high stability of the generated compression flow, the possibility of controlling flow composition, plasma size and plasma parameters, and a long discharge time sufficient for practical use [6–9].

Experimental methodology. Compression plasma flows were obtained using a compact gas-discharge MPC whose energy storage system consisted of a capacitor bank with a capacity of 1200 μF at an initial voltage changing from 3 to 5 kV [7]. The MPC operated in the residual-gas regime wherein the accelerator chamber was preliminary pumped out after which it was filled with nitrogen to a preset pressure (100–1300 Pa). Under these conditions, a compression plasma flow 6–10 cm in length and with a diameter of 1 cm in the maximum compression zone was formed at the output of the MPC discharge device. Plasma flow in the MPC is compressed due to the interaction between the longitudinal component of a discharge current flowing out from the discharge device and the self-magnetic azimuthal field. The presence of a "flow-out" current in the plasma flow is caused by the magnetic field freezing in plasma.

The plasma velocity in a compression flow is in the range of $(4–7) \times 10^6$ cm/s, depending on the initial parameters of the MPC. The concentration of charged particles in the maximum compression zone is as high as $(5–10) \times 10^{17}$ cm^{-3}, and the temperature is 1–3 eV [6–8]. The compression flow is stable for about 80 μs, after which it starts to decay.

Samples of (111)-oriented 280-μm-thick silicon single crystals with an area of 10×10 mm^2 were placed perpendicularly to the compression flow at distances 6–16 cm from the cut of the MPC discharge device and exposed to the compression plasma flow. The incident compression flow gives rise to a shock-compressed plasma layer near the sample surface. Note that the deceleration of a compression plasma flow with the frozen-in magnetic field is accompanied by the formation of current loops (vortices) [10, 11].

The plasma density in the zone of interaction with the sample changed from 10^{18} cm^{-3} (in the maximum compression region) to 10^{16} cm^{-3} (in the region of strong flow divergence). Calorimetric measurements showed that the energy absorbed by the sample decreased, accordingly, from 25 to 5 J, which corresponded to a change of $(3–0.5) \times 10^5$ W/cm^2 in the

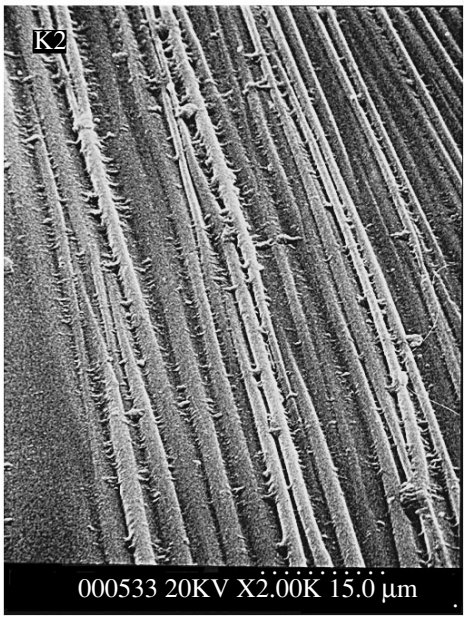

Fig. 1. Surface morphology of silicon exposed to a compression plasma flow.

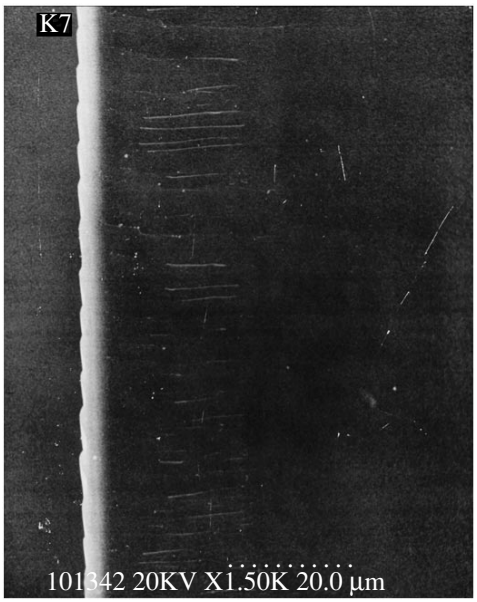

Fig. 2. Structure of the near-surface region of silicon.

plasma flow power density under the conditions of our experiments.

The surface microrelief and the slices of silicon single-crystal samples were photographed using high-resolution scanning electron microscopy on a Hitachi S806 microscope.

Results. Under the action of the compression plasma flow on the sample, silicon melts and its surface is modified to a depth of 6 μm. A periodic structure formed by the cylindrically shaped fragments is clearly seen in the microphotographs of the surface layer (Fig. 1). The length of these fragments exceeds 50 μm, and their diameter is 0.7–1.0 μm. The spacing between the fragments at the sample surface is in the range of 1–2 μm, and their density is $(2–6) \times 10^6$ cm^{-2}. The presence of the offshoots between the cylindrical fragments of the structure gives evidence for the influence of the external force factors on the process of structural phase transformation.

Periodic structures formed by the channels oriented normally to the surface are observed inside the modified layer (Fig. 2). The channels are ~6–12 μm in length, their diameter is ~0.1–0.2 μm, and spacing (1–2 μm) corresponds to the spacing of the cylindrical surface formations.

The formation of observed structures is primarily caused by the energetic action of the compression flow on the surface, leading to its fast heating, melting of the surface layer, development of thermoelastic stresses, and plasma spreading over the surface under the action of the dynamic pressure (on the order of several atmospheres) of compression flow and the gradient of plasma parameters in the shock-compressed plasma layer. The silicon crystallization is characterized by fast cooling and high temperature gradients. These processes occur in the presence of magnetic fields induced by the "flow-out" currents in the incident plasma flow.

The interaction of the compression plasma flow with the surface is accompanied by the appearance of thermoelastic stresses in the silicon lattice; the corresponding stress gradient field generates dislocations through well-known mechanisms. At a certain concentration of dislocations, they form periodic aggregates. As is known, crystallizing melt inherits structural imperfections of the substrate and brings them out at the surface. The moving crystallization front represents a solidifying array of steps which, in turn, may become the nuclei of cylindrical formations in the presence of developing instability.

The instability arises due to the plasma flow pressure (on the order of several atmospheres) on the silicon melt. Under the pressure of the compression flow, light surface layers are pressed through the heavier melt layers, giving rise to Rayleigh–Taylor instability. Plasma pressure may also induce Benard convective instability in the molten silicon layer. In this case, pressure favors the convective mixing of layers heated to different temperatures, leading to the self-organization manifesting itself as structural formations [12]. Kelvin–Helmholtz instability arises at the interface of two fluids or gases with different densities upon their sliding relative to each other. This type of instability is typical for wave swinging in windy weather [13]. In our case, it arises due to spreading of the shock-compressed plasma layer over the silicon surface. In this case, two flows with different velocities run in the same direction. Since the flows are coulombic systems, the wave disturbance

scale must diminish. In our case, the character of the disturbances, whose wavelength corresponds to a frequency on the order of 10^{14} Hz, correlates with the ion plasma oscillations in the ionized surface layer.

In addition, the silicon plate undergoes sign-variable bending under the action (and during the lifetime) of thermoelastic stress, as a result of which the molten substance crystallizes at the substrate of a variable shape. In conjunction with the surface tension effects, this leads to a complex surface morphology and gives rise to formations of the offshoot type between the cylinders.

Conclusions. As a result of our studies, the submicron-sized cylindrical structures have been formed at the silicon surface under the action of a compression plasma flow. A periodic array of channels oriented normally to the surface were observed inside the modified silicon layer, with the period corresponding to the spacing of the cylindrical formations. The structural phase transformations of the silicon surface state may be associated with fast crystallization of the molten layer on the background of various instabilities that develop in the presence of the induced magnetic field.

REFERENCES

1. W. Hang, Y. Bando, K. Kurashima, *et al.*, Appl. Phys. Lett. **73**, 3085 (1998).
2. T. Laude, A. Marraud, Y. Matsui, *et al.*, Appl. Phys. Lett. **76**, 3239 (2000).
3. M. Zhang, Y. Bando, and K. Wada, J. Mater. Res. **15**, 387 (2000).
4. S. B. Fagan, R. J. Baierle, R. Mota, *et al.*, Phys. Rev. B **61**, 9994 (2000).
5. A. I. Morozov, Nuclear Fusion, Special Suppl. (1969), p. 111.
6. S. I. Ananin, V. M. Astashynski, G. I. Bakanovich, *et al.*, Fiz. Plazmy **16**, 186 (1990) [Sov. J. Plasma Phys. **16**, 102 (1990)].
7. V. M. Astashynski, V. V. Efremov, E. A. Kostyukevich, *et al.*, Fiz. Plazmy **17**, 1111 (1991) [Sov. J. Plasma Phys. **17**, 645 (1991)].
8. V. M. Astashynski, G. I. Bakanovich, A. M. Kuz'mitski, *et al.*, Inz.-Fiz. Zh. **62**, 714 (1992).
9. V. M. Astashynski, A. A. Man'kovskiĭ, L. Ya. Min'ko, and A. I. Morozov, Fiz. Plazmy **18**, 90 (1992) [Sov. J. Plasma Phys. **18**, 47 (1992)].
10. S. I. Ananin, Fiz. Plazmy **21**, 966 (1995) [Plasma Phys. Rep. **21**, 913 (1995)].
11. S. I. Ananin, V. M. Astashynski, E. A. Kostyukevich, *et al.*, Fiz. Plazmy **24**, 1003 (1998) [Plasma Phys. Rep. **24**, 936 (1998)].
12. H. Haken, *Synergetics: an Introduction* (Springer-Verlag, Berlin, 1977; Nauka, Moscow, 1985).
13. Yu. A. Stepanyants and A. L. Fabrikant, *Propagation of Waves in Shear Flows* (Nauka, Moscow, 1996).

Translated by V. Sakun

JETP Letters, Vol. 74, No. 4, 2001, pp. 216–221. Translated from Pis'ma v Zhurnal Éksperimental'noĭ i Teoreticheskoĭ Fiziki, Vol. 74, No. 4, 2001, pp. 237–243.

Dynamic Light Scattering Study of the Interface Evolution in Porous Media

D. A. Zimnyakov*, P. V. Zakharov, V. A. Trifonov, and O. I. Chanilov

Saratov State University, ul. Astrakhanskaya 83, Saratov, 410026 Russia

** e-mail: zimnykov@sgu.ssu.runnet.ru*

Received May 8, 2001; in final form, July 17, 2001

The interface evolution during the evaporation of a liquid from a saturated layer of porous medium (paper) was experimentally studied using spectral analysis of intensity fluctuations of a laser radiation scattered by the layer. The data obtained were compared with the results of modeling the irreversible growth in three-dimensional lattices. The dependences of the spectral halfwidth of intensity fluctuations on the drying time demonstrate the characteristic features of drying front evolution, which proved to be similar to those found in the modeling of irreversible growth front. A comparison of the maximal halfwidths for two different saturating liquids suggests that the motion of local interfaces during the liquid evaporation from a layer of porous medium is close to the "classical" diffusion. © *2001 MAIK "Nauka/Interperiodica".*

PACS numbers: 68.03.Fg; 78.35.+c

The study of transport processes in the disordered systems is an intensively progressing direction in condensed matter physics. Mass transfer in porous media during the evaporation of a liquid or its propagation in a pore system under the action of capillary forces is a typical example of such processes. They are accompanied by an intriguing physical phenomena (e.g., the formation of fractal growth boundaries [1, 2]), which are universal in nature and have been the subject of theoretical and experimental investigations over the past two decades. The elaboration of experimental methods for analyzing mass transfer dynamics in heterogeneous multiphase systems is an important aspect of these studies. In this work, the possibility of using dynamic coherent light scattering in studying the evolution of the interface between the gaseous and liquid phases during the evaporation of a liquid from a layer of a porous medium is considered. In this system, the intensity fluctuations of scattered light at the observation point are caused by the scattering of probe radiation from moving local interfaces in the pore system. Figure 1 is the illustration of a model of multiple scattering in the drying zone; the scatter of the velocities and motion directions of local boundaries, which thus form an ensemble of nonstationary scatterers, gives rise, as a result of the interference between the partial field components with different scattering multiplicities, to a speckle pattern, for which the spectral width of intensity fluctuations is determined by the average mobility of the local boundaries and their bulk concentration in the drying zone. The propagation of probe radiation in regions *1*, *1'*, and *3*, where the system of scatterers is stationary, does not lead to frequency modulation for the partial components. At the same time, the Doppler shifts caused by the scattering of partial components from the moving local interfaces in the drying zones (*2*, *2'*) give rise, as a result of multiple scattering, to a nonstationary speckle pattern in the observation plane. It was found in [3] that the drying fronts of fluids in porous media can be treated as fractal growth boundaries with clusters of liquid-filled pores located nearby. The evolution of such structures during the drying process should influence the bulk concentration of scattering centers in the drying zone and, hence, lead to tangible changes in the spectrum of scattered intensity fluctuations.

Figure 2 presents the scheme of experimental setup for studying spectral characteristics of the scattered intensity fluctuations during the course of liquid evaporation from an originally saturated layer of porous medium. A single-mode He–Ne laser (λ = 632.8 nm, output 0.5 mW) was used as a radiation source. The laser beam was focused to a $\approx$200 μm-diameter spot at the surface of a layer which was placed in the horizontal plane. Paper samples differing in the degree of porosity and in thickness were used as layers of porous medium. The intensity fluctuations were detected in the transmission geometry using a computer image-locking system with a lensless EDC-1000L (Electrim Corp., USA) CCD chamber. The number of pixels was 484×753 with a pixel size of 9.5×10 μm^2. The distance between the sample and the CCD chamber was 60 cm; the chamber was placed on the beam axis; the average speckle size in the image detection plane was $\approx$500 μm. The images of dynamic speckles were recorded in the wrap mode, for which the intensity fluctuations at fixed points were mapped as brightness distributions over image columns written in the bit-map format; the fragments of these images are shown in the insets in Fig. 3. The image writing time varied from 40 to 120 s depend-

0021-3640/01/7404-0216$21.00 © 2001 MAIK "Nauka/Interperiodica"

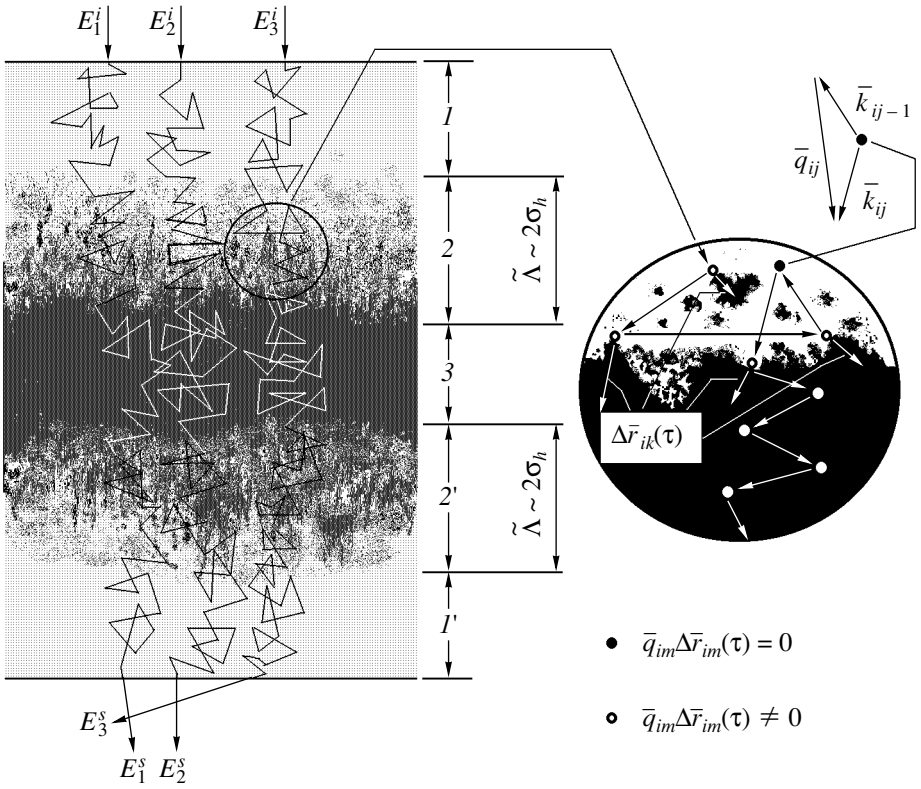

Fig. 1. Model of coherent radiation multiple scattering by a layer of porous medium during the evaporation of a liquid. The detected nonstationary speckle patterns are formed as a result of the interference between partial scattered-field components (E_1^s, E_2^s, …) propagating in the periaxial zone of the illuminating beam. The frequency of partial components is modulated due to the scattering by the nonstationary scatterers (moving local interfaces) with $\bar{q}_{im}\Delta\bar{r}_{im}(\tau) \neq 0$. The interface between the liquid and gaseous phases in the layer is a fractal surface [2, 3].

ing on the line exposure time T_E; the Nyquist frequency [4] corresponding to the separation between pixels along a column changed from 2 to 6 Hz. To minimize the effects (in particular, the frequency overlap or masking effect [4]) caused by the finite fetch time and finite T_E-controlled digitizing rate of intensity distribution over columns on the results of spectral analysis of the narrow-band random process of intensity fluctuations, the line exposure time for each image was chosen, after preliminary experiments, in such a way that the sampling rate exceeded the halfwidth of the fluctuation spectrum by no less than a factor of ten for the image fragment having maximal spectral width. Further analysis consisted in the calculation of the modulus of the Fourier-transform $|F_1(\nu)|$ of the intensity fluctuations by applying the discrete Fourier transform to the sets of column data for the image areas obtained by breaking images into partially overlapping fragments of size $W_1 \times W_2 = 100 \times 753$ pixels. The values of the modulus of the Fourier transform were averaged over the columns for each fragment; the halfwidths $\nu_{0.5}$ were estimated for the average spectra. Checking for the influence of the recording and image processing regimes (line exposure time T_E and size W_1 of the fragment chosen) showed that the estimates of $\nu_{0.5}$ were stable to the variations of T_E and W_1 if $T_E < (10\nu_{0.5})^{-1}$ and $W_1 = 80$–120; in particular, a change in $\nu_{0.5}$ for the image fragments characterized by the maximal spectral width of intensity fluctuations did not exceed 8% upon a decrease in T_E from 150 to 100 ms and an increase in the pixel number from 80 to 120. Typical frequency dependences obtained for the normalized average spectrum $|F_1(\nu)|$ after processing the experimental dynamic speckle images are shown in the inset in Fig. 2.

Experiments were performed at room temperature [(20 ± 1)°C]; ethyl alcohol C_2H_5OH and acetone C_3H_6O were used as saturating liquids. The thickness $\tilde{H}$, the porosity ϕ, and the characteristic removal time t_r corresponding to the *e*-fold drop in the weight of the liquid phase were preliminarily determined for each sample. The values of ϕ and t_r were found by weighing the originally saturated samples on an electronic balance with sampling of the data at 1 s. Typical experimental depen-

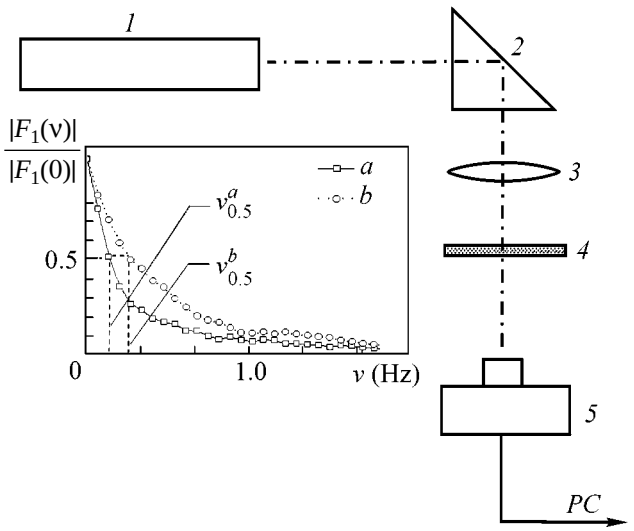

Fig. 2. Scheme of experimental setup. (*1*) Single-mode He–Ne laser; (*2*) turning prism; (*3*) focusing lens; (*4*) sample; and (*5*) CCD chamber. Inset: typical frequency dependences of the normalized intensity fluctuation spectra obtained by averaging over the set of columns for image fragments of size 100 × 753 pixels; ethyl alcohol is taken as a saturating liquid; sample parameters: $\tilde{H} = 71 \pm 3$ μm and $\phi = 0.68 \pm 0.04$; (*a*) $t_{dr} = 23$ s and $\nu_{0.5}^{a} \approx 0.14$ Hz and (*b*) $t_{dr} = 150$ s and $\nu_{0.5}^{b} \approx 0.26$ Hz. Digitizing rate 6.7 Hz.

dences of the halfwidth $\nu_{0.5}$ on the drying time t_{dr} are presented in Fig. 3. The following characteristic features of the $\nu_{0.5}(t_{dr})$ curves are noteworthy:

(1) The frequency of scattered intensity fluctuations drastically increases and achieves a maximum at a certain stage of the drying process; the relationship between the time $t_{dr\,\max}$ corresponding to the maximal $\nu_{0.5}$ and the time t_r can be approximated by the linear dependence (Fig. 4);

(2) A decrease in the characteristic removal time t_r is accompanied by the decrease in the maximal value of $\nu_{0.5}$ (Fig. 2; the t_r values for C_3H_6O are 4–6 times shorter than for C_2H_5OH, and the corresponding $\nu_{0.5}$ values are shorter by a factor of 1.2 to 2);

(3) The $\nu_{0.5}(t_{dr})$ dependence is pronouncedly asymmetric for small t_r; at the final stage of the drying process, $\nu_{0.5}$ decreases jumpwise at some frequencies; the $\nu_{0.5}(t_{dr})$ curves become more symmetric with increasing t_r, and the jumpwise changes in $\nu_{0.5}$ are greatly suppressed at large t_{dr} times.

The study of the heating effect caused by the absorption of the laser probe radiation on the drying process showed that a twofold increase in the spot diameter and the corresponding decrease in the probe radiation flux density (by a factor of four) after displacing the samples from the focal plane of lens *3* along the beam axis and, hence, beam defocusing (Fig. 2) did not affect the measured $t_{dr\,\max}$ values to within the experimental accuracy (±5%). Likewise, a change in the beam power with the help of attenuators (neutral filters) also did not change noticeably $t_{dr\,\max}$. This was so because of the low probe radiation power (<0.5 mW with allowance made for the additional losses in optical elements *2* and *3*) and the small absorption coefficient of the layers (the absorption coefficients of paper in the visible region are typically 0.005–0.03 mm^{-1} [5]). Therefore, the heating effect of the probe radiation on the evaporation of a liquid from the layer can be ignored under the experimental conditions used in this work.

To interpret the experimental results, we invoke the approach used in [6] for the description of the time correlation function for the fluctuations of coherent light undergoing multiple scattering in a nonstationary system of statistically independent scatterers. For a fixed point, this function can be written as

$$G_1(\tau) = \langle E(t)E^*(t+\tau)\rangle \sim \exp(-j\omega\tau) \times\left\langle\left(\sum_i\prod_m \exp\{i\bar{q}_{im}\bar{r}_{im}(t)\}\right) \times\left(\sum_i\prod_m \exp\{i\bar{q}_{im}\bar{r}_{im}(t+\tau)\}\right)^*\right\rangle,$$

where the summation over *i* goes over the contributions from the partial scattered components with different optical paths to the complex field amplitude at the observation point; the multiplication index *m* corresponds to the phase incursion for each partial component after it goes through a series of scattering events at the moving local interfaces; $\bar{q}_{im}$ is a change in the wave vector of the *i*th partial component in the *m*th scattering event at the boundary whose position is specified by the radius vector $\bar{r}_{im}$; and ω is the probe beam frequency. Averaging is done over the ensemble of possible configurations of the moving scattering centers. Assuming that the scattering events are statistically independent, one arrives at the following expression for the time correlation function $G_2(\tau) = \langle\{I(t+\tau) - \langle I\rangle\}\{I(t) - \langle I\rangle\}\rangle$ at a large number of scattering events:

$$G_2(\tau) = |G_1(\tau)|^2 \sim \left|\left\langle \sum_i \exp\{-\Xi_i\langle\bar{q}^2\rangle\langle\Delta\bar{r}^2(\tau)\rangle/6\}\right\rangle\right|^2, \quad (1)$$

where Ξ_i is the number of scattering events for the *i*th partial component and $\Delta\bar{r}^2(\tau)$ is the scatterer displacement variance at time τ.

The fluctuation dynamics of the scattered intensity depends on the effective value of Ξ, which is determined by the number of moving local interfaces in the beam scattering region (Fig. 1). An increase in Ξ results

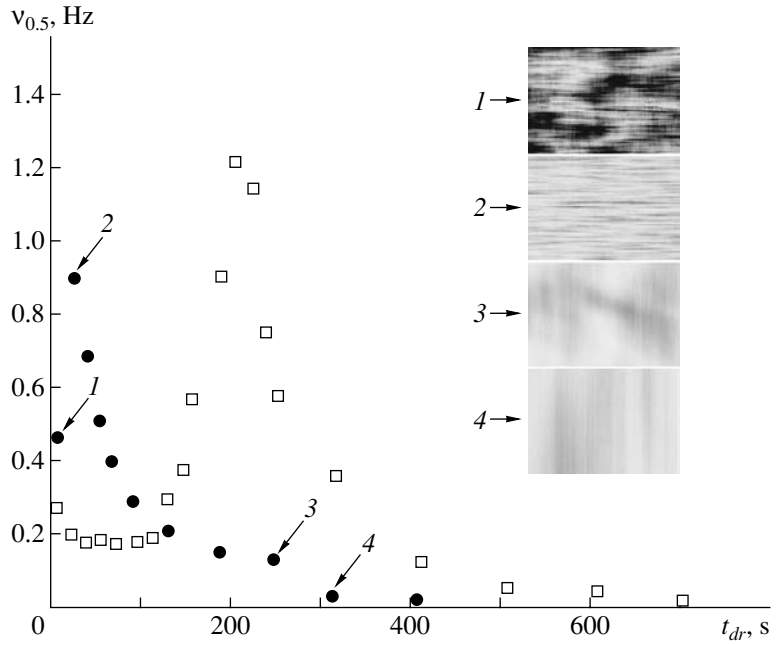

Fig. 3. Spectral halfwidths $\nu_{0.5}$ of the scattered intensity fluctuations vs. drying time t_{dr} for the paper samples of thickness $\tilde{H} = 88 \pm 3$ μm and porosity $\phi = 0.56 \pm 0.03$; saturating liquid: (●) acetone (C_3H_6O) and (□) ethyl alcohol (C_2H_5OH).

in shortening the correlation time and broadening the fluctuation spectrum of scattered intensity. Thus, the development of the drying zone should manifest itself in the dependence of the width of fluctuation spectrum on the time of liquid evaporation from the layer. To write $G_2(\tau)$ in the analytic form, the Ξ_i statistics must be known for the scattering system; in particular, for a moving scattering layer of thickness Λ illuminated by a plane wave with wavenumber k, $G_2(\tau)$ for the forward-scattered radiation can be written as $G_2(\eta) \sim \exp(-2\eta)$, where $\eta = (\Lambda/l^*)\sqrt{k^2\langle\Delta\bar{r}^2(\tau)\rangle}$ and l^* is the transport mean free path of the scattering layer [7, 8]. For the generalized Brownian dynamics of the scattering centers [2], one has $\langle\Delta\bar{r}^2(\tau)\rangle = K\tau^\vartheta$, where $0 \le \vartheta \le 2$ and K characterizes the scatterer mobility, so that the fluctuation correlation time can be defined as

$$\tau_c \approx (l^{*2}/4Kk^2\Lambda^2)^{1/\vartheta} \sim \nu_{0.5}^{-1}. \qquad (2)$$

Note that the dependence of τ_c and $\nu_{0.5}$ on the radiation wavelength λ is due not only to the dependence on k but also, implicitly, to the dependence on the transport mean free path l^*, because $l^* = [\sigma(\lambda)c\{1 - g(\lambda)\}]^{-1}$ [7, 8], where c is the bulk concentration of the nonstationary scatterers (moving local interfaces) in the drying zone and $\sigma(\lambda)$ and $g(\lambda)$ are, respectively, the wavelength-dependent effective values of the scattering cross section and the scatterer anisotropy parameter.

Assuming that the exponent ϑ does not depend on the properties of the saturating fluid and setting $\Lambda \sim \tilde{\Lambda}$, where $\tilde{\Lambda}$ is the width of the drying zone, one finds, with the scattering model adopted (Fig. 1), that, when probing at a fixed wavelength, the following relationship should take place between the maximal $\nu_{0.5}$ values for

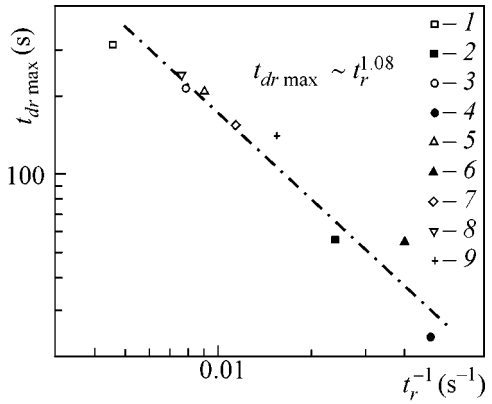

Fig. 4. Relationship between the parameters $t_{dr\,\max}$ and t_r for the paper samples; (*1*) $\tilde{H} = 135 \pm 3$ μm, $\phi = 0.84 \pm 0.04$ (filter paper), and acetone (C_3H_6O) as a saturating liquid; (*2*) the same for ethyl alcohol (C_2H_5OH); (*3*) $\tilde{H} = 71 \pm 3$ μm, $\phi = 0.68 \pm 0.04$, and acetone; (*4*) the same for ethyl alcohol; (*5*) $\tilde{H} = 88 \pm 3$ μm, $\phi = 0.56 \pm 0.03$, and acetone; (*6*) the same for ethyl alcohol; (*7*) $\tilde{H} = 73 \pm 3$ μm, $\phi = 0.52 \pm 0.03$, and ethyl alcohol; (*8*) $\tilde{H} = 77 \pm 3$ μm, $\phi = 0.63 \pm 0.03$, and ethyl alcohol; and (*9*) $\tilde{H} = 72 \pm 3$ μm, $\phi = 0.39 \pm 0.02$, and ethyl alcohol.

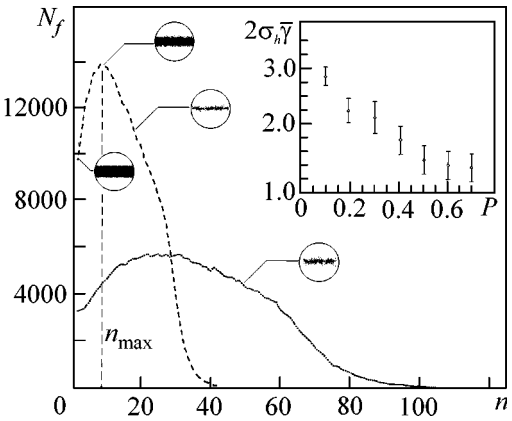

Fig. 5. Plots of N_f as functions of the irreversible growth time (number of modeling steps) for a $100 \times 100 \times 30$ lattice with $\Theta = 6$; the dashed curve is for $P = 0.3$, and the dotted line is for $P = 0.1$ (results of statistical modeling). Inset: P dependence of the surface concentration $2\sigma_h\bar{\gamma}$ of occupied sites at the growth front for $n = n_{\max}$ (obtained for the $100 \times 100 \times 30$ lattice with $\Theta = 6$).

two different saturating fluids with close refraction indices (and, hence, with $\sigma_1 \approx \sigma_2$, $g_1 \approx g_2$, and $l_1^*/l_2^* \approx c_2/c_1$):

$$\frac{(\nu_{0.5})_{1\,\max}}{(\nu_{0.5})_{2\,\max}} \approx \left(\frac{K_1\tilde{\Lambda}_{\max\,1}^2 c_{\max\,1}^2}{K_2\tilde{\Lambda}_{\max\,2}^2 c_{\max\,2}^2}\right)^{1/\vartheta}, \qquad (3)$$

where $\tilde{\Lambda}_{\max}$ and $c_{\max}$ correspond to the maximal development of the drying zone (for $t_{dr} = t_{dr\,\max}$). It is worth noting that, if the scattering geometry is changed (in particular, if the layer is illuminated by a localized source rather than by the plane wave), the dependence of the time correlation function on the dimensionless parameter η will be other than $G_2(\eta)\exp(-2\eta)$. At the same time, according to the similarity principle, $\tau_c \sim (l^{*2}/Kk^2\Lambda^2)^{1/\vartheta}$, and relationship (3) should also hold in the case.

Of interest was to estimate the exponent ϑ for the system of nonstationary scatterers. With the aim of analyzing the drying zone evolution in a liquid-saturated layer of a porous medium, the irreversible growth process was statistically modeled for three-dimensional lattices of finite size; the model used was a modification of the Eden model [9]. The process of escaping from the occupied sites starting at the surface was considered for the lattices of size $L \times L \times H$ ($L \gg H$) with a varied number Θ of bonds between the neighboring sites and varied escape probability P. The irreversible growth was characterized by the number of sites N_f that were left at each time step. It was assumed that each escape event was statistically independent and occurred with the probability P if there was at least one bond with a vacant site.

Plots of typical dependences of N_f on the dimensionless time (number n of modeling steps) for the vacant region growing from the surface of the $L \times L \times H$ lattice are shown in Fig. 5. For $P \le P_c \approx 0.7$, the curves display maxima corresponding to the maximal number of sites that are left in the "active" zone of the growth front of thickness $\sigma_h(n) = \overline{(\{h(x,y) - \bar{h}\}^2)}^{0.5} \sim \tilde{\Lambda}$, where $h(x, y)$ is the front "height" in the propagation direction. For $P > P_c$, the maximal value of N_f occurs at $n = 0$, and $n_{\max}$ depends on P as

$$n_{\max} \sim P^{-\alpha}, \qquad (4)$$

where α is close to unity and shows little dependence on Θ, L, and H. The occurrence of a maximum in a certain range a is caused by the competition of two processes: development of the active growth zone, i.e., an increase in σ_h and in the average concentration $\bar{\gamma}$ of the occupied sites in the active zone, and a decrease in the volume of the active zone because of an increasing number of vacant sites: $d\{(a - \bar{h}(n))^2\sigma_h(n)\bar{\gamma}(n)\} = 0$.

Another feature of the $N_f(n)$ dependence in the irreversible growth is that dN_f/dn changes near-jumpwise at the final stages of the process, because the filled region breaks into separate clusters [see dots *3* and *4* in Fig. 3]. The changes in the form of the $N_f(n)$ dependences with a decrease in P are qualitatively similar to those observed experimentally for the $\nu_{0.5}(t_{dr})$ dependences with an increase in t_r (Fig. 3): the asymmetry is smoothed out and a portion corresponding to the clustering stage becomes less pronounced (dotted line in Fig. 5). The sections of the filled region at the initial stage of irreversible growth, at the instant of time corresponding to the maximal development of the growth active zone, and at the clustering instant n_c are given in Fig. 5. In the quasi-one-dimensional front-propagation regime (for the irreversible growth in a layer with $L \longrightarrow \infty$), N_f monotonically increases and tends towards saturation [because of the saturation of $\sigma_h(n)\bar{\gamma}(n)$] at a level corresponding to clustering. In this case, the relationship between $n_{\max}$ and P is also given by Eq. (4). The parameter $2\sigma_h(n_{\max})\bar{\gamma}(n_{\max})$ characterizing the effective surface concentration of occupied sites at the front at $n = n_{\max}$ is shown as a function of P in the inset in Fig. 5. It was found by modeling that for the models with different Θ, L, and H, the relationship between $n_{\max}$ and n_r corresponding to the e-fold drop in the number of occupied sites can be approximated by the linear dependence of the form $n_{\max} \sim n_r^{1.05 \pm 0.10}$ for $0.01 \le P \le 0.5$ (Fig. 6); this is consistent with the experimentally obtained relationship between $t_{dr\,\max}$ and t_r (Fig. 4).

The analogy between the experimentally measured $\nu_{0.5}(t_{dr})$ and $t_{dr\,\max}(t_r)$ dependences and the $N_f(n)$ and $n_{\max}(n_r)$ dependences obtained in the irreversible growth model allows the use of this model in interpret-

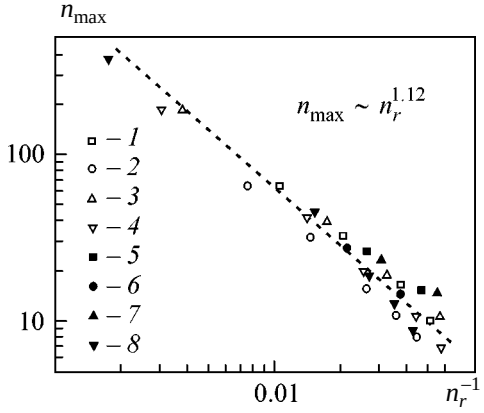

Fig. 6. Relationship between the parameters n_{max} and n_r for the irreversible growth in three-dimensional lattices with different probabilities of escaping from the occupied sites (modeling results); $0.01 \le P \le 0.5$; (*1*) $L = 100$, $H = 30$, and $\Theta = 4$; (*2*) $L = 100$, $H = 50$, and $\Theta = 4$; (*3*) $L = 100$, $H = 30$, and $\Theta = 8$; (*4*) $L = 100$, $H = 50$, and $\Theta = 8$; (*5*) $L = 100$, $H = 30$, and $\Theta = 14$; (*6*) $L = 100$, $H = 50$, and $\Theta = 14$; (*7*) $L = 150$, $H = 20$, and $\Theta = 14$; and (*8*) $L = 400$, $H = 50$, and $\Theta = 6$.

ing the experimental results on the basis of the correspondence between $\bar{\gamma}$ and c. With this approach, the following relationship may be considered: $\sigma_h(n)\bar{\gamma}(n) \sim c(t_{dr})\tilde{\Lambda}(t_{dr})$. For two saturating liquids with essentially different times t_r ($t_{r1} \gg t_{r2}$), we assume, based on the modeling results (inset in Fig. 5), that $\Lambda_{1\,max}c_{1\,max}/\Lambda_{2\,max}c_{2\,max} \approx 3$ for the maximal intensity fluctuation frequency at $t_{dr} = t_{dr\,max}$.

When estimating K_1/K_2, we assume the relation $K \sim t_r^{-\beta}$ between K and t_r, with parameter β depending on ϑ. In particular, one has $K \sim t_r^{-2}$ for $\vartheta = 2$, which can be interpreted as a directed motion of local interfaces with root-mean-square velocity $\langle \bar{v}^2 \rangle^{0.5} = K^{0.5}$. One can readily show that the experimentally observed ratio $(\nu_{0.5})_{1\,max}/(\nu_{0.5})_{2\,max} > 1$ does not hold for the measured values $t_{r1}/t_{r2} = 4.5$–6. In the case of $\vartheta = 1$, corresponding to the classical Brownian motion of local scatterers, the parameter $K/6$ has a meaning of the diffusivity of scattering centers, and the β value can be obtained by analyzing the well-known relation between the concentration gradient of diffusing particles and the respective mass flow J in the form $K(\mathrm{grad}\,c)_z = -J$, where z is the propagation direction of the diffusion front. For the irreversible growth model adopted in this work, the use of the approximate relationship $(\mathrm{grad}\,c)_z \sim \gamma/\sigma_h$ in the growth zone gave $K \sim n_r^{-\beta}$ in the course of modeling, with $\beta \approx 0.70$–1.00 (depending on the model parameters). In this case, the estimate of the ratio $(\nu_{0.5})_{1\,max}/(\nu_{0.5})_{2\,max}$ using Eq. (3) gives a value of the order 0.4–0.7 for $t_{r1}/t_{r2} = 4.5$–6, which is in satisfactory agreement with the experiment. On the other hand, the estimate of parameter ϑ with the use of the results of statistical modeling and the experimentally measured ratios $(\nu_{0.5})_{1\,max}/(\nu_{0.5})_{2\,max}$ yields values ranging from 0.83 to 1.17 for the six samples studied.

Thus, with the assumptions adopted in this work, the motion of local interfaces in the drying zone can be interpreted as a generalized Brownian motion with parameter ϑ close to unity, i.e., close to the value inherent in classical Brownian motion. The local boundary dynamics observed in the experiment on dynamic coherent radiation scattering can be caused by a considerable scatter of the directions and velocities of boundary motion, as well as by the finite lifetimes of local boundaries in individual pores.

This work was supported by the Russian Foundation for Basic Research and the Belarussian Foundation for Basic Research (project no. 00-02-81014), the Russian Foundation for Basic Research (project no. 01-02-17493), the AFGIR (grant no. REC-006), and the program "Fundamental Research in Natural and Humanitarian Sciences. Russian Universities" [project no. 015.01.01.20 (990632)].

REFERENCES

1. *Fractals in Physics*, Ed. by L. Pietronero and E. Tozatti (Elsevier, Amsterdam, 1986; Mir, Moscow, 1988).
2. J. Feder, *Fractals* (Plenum, New York, 1988; Mir, Moscow, 1990).
3. T. M. Shaw, Phys. Rev. Lett. **59**, 1671 (1987).
4. R. Otnes and L. Enochson, *Applied Time Series Analysis*, Vol. 1: *Basic Techniques* (Wiley, New York, 1978; Mir, Moscow, 1982).
5. J. Plucinski, *Optical Parameters Estimation of Paper and Pulp by Time-resolved Spectroscopy (Technical Report)* (Optoelectronics and Measurement Technology Laboratory, University of Oulu, Finland, 2000).
6. G. Maret and P. E. Wolf, Z. Phys. B **65**, 409 (1987).
7. F. C. MacKintosh and S. John, Phys. Rev. B **40**, 2383 (1989).
8. P.-A. Lemieux, M. U. Vera, and D. J. Durian, Phys. Rev. E **57**, 4498 (1998).
9. M. Eden, in *Proceedings of the Fourth Berkeley Symposium on Mathematical Statistics and Probabilities*, Ed. by F. Newman (Univ. Of California Press, Berkeley, 1961), Vol. IV, p. 233.

Translated by V. Sakun

JETP Letters, Vol. 74, No. 4, 2001, pp. 222–225. Translated from Pis'ma v Zhurnal Éksperimental'noĭ i Teoreticheskoĭ Fiziki, Vol. 74, No. 4, 2001, pp. 244–247.

Crystal Structure and Optical Activity of $La_3Nb_{0.5}Ga_{5.5}O_{14}$ and $Sr_3Ga_2Ge_4O_{14}$ Single Crystals of the Langasite Family

V. N. Molchanov, B. A. Maksimov, A. F. Kondakov, T. S. Chernaya, Yu. V. Pisarevskiĭ, and V. I. Simonov

Shubnikov Institute of Crystallography, Russian Academy of Sciences, Leninskiĭ pr. 59, Moscow, 117333 Russia

Received July 17, 2001

Precision X-ray structural studies of the $La_3Nb_{0.5}Ga_{5.5}O_{14}$ and $Sr_3Ga_2Ge_4O_{14}$ single crystals were carried out. The space group *P*321 was confirmed. The anomalous X-ray scattering was taken into account to establish the absolute structures (chirality) of the crystals; they proved to be of different sign. The structural features responsible for the optical activity of crystals were revealed, and the dependence of the magnitude and sign of specific rotation on the structural parameters of these compounds were determined. *© 2001 MAIK "Nauka/Interperiodica".*

PACS numbers: 61.66.Fn; 61.10.Eq; 78.20.Ek

Ca gallogermanate $Ca_3Ga_2Ge_4O_{14}$ was the parent of a rich family of trigonal acentric crystals [1, 2]. More recently, the members of this family were named langasites, a shorthand for the chemical composition of $La_3Ga_5SiO_{14}$ [3, 4]. One of the latest reviews devoted to the materials of this family was published in the Proceedings of Frequency Control Symposium [5]. The growing interest in langasites is caused by the unique physical properties of their pure samples and samples activated with transition ions: piezoelectricity, elastic properties, luminescence, lasing, and, especially, composition-controlled optical properties [6–8]. The purpose of this work was to refine atomic structures of the $La_3Nb_{0.5}Ga_{5.5}O_{14}$ and $Sr_3Ga_2Ge_4O_{14}$ single crystals using X-ray diffraction analysis. Of interest was also to determine the chirality of the samples; to reveal structural origins of their optical activity and the substantial difference in specific rotations, which, according to the data in [8], are, respectively, 16.8 and 4.42 deg/mm at $\lambda = 0.55$ μm; and to refine the distribution of cations over the voids of anionic packing. Single crystals of $La_3Nb_{0.5}Ga_{5.5}O_{14}$ and $Sr_3Ga_2Ge_4O_{14}$ were grown by the Czochralski method.

Samples of $La_3Nb_{0.5}Ga_{5.5}O_{14}$ and $Sr_3Ga_2Ge_4O_{14}$ single crystals chosen for X-ray structural analysis were shaped into a sphere by rolling. Sphere diameters were, respectively, 0.22(1) and 0.27(1) mm. Integrated intensities of X-ray reflections were measured on an Enraf-Nonius CAD-4F diffractometer (MoK_α radiation, graphite monochromator, $\omega/2\theta$ scan mode in the full range of reflections for $\sin\theta/\lambda \le 0.9$ Å^{-1}). A total of 7571 and 7527 reflections, respectively, were measured. After averaging symmetry-related reflections, working arrays of 1184 and 1149 unique reflections with $I > 3\sigma(I)$ were formed. The discrepancy factors for the averaging of equivalent structure amplitudes were 1.88 and 1.39%. Bievout pairs of reflections with indices hkl and $\bar{h}\bar{k}\bar{l}$ were not averaged, because only their differences carry information about crystal chirality in the presence of anomalous scattering. With allowance made for the anomalous components f' and f'', the atomic scattering factors have the form $f = f_0 + f' + if''$. For the MoK_α radiation with $\lambda = 0.7107$ Å, the real and imaginary corrections for anomalous X-ray scattering are $f' = -0.2871$ and $f'' = 2.4523$ for the La atom, $f' = -2.0727$ and $f'' = 0.6215$ for Nb, $f' = 0.231$ and $f'' = 1.608$ for Ga, $f' = -1.5307$ and $f'' = 3.2498$ for Sr, and $f' = 0.1547$ and $f'' = 1.8001$ for Ge; for the O atoms, the corrections are negligible: $f' = 0.0106$ and $f'' = 0.0060$ [9].

Analysis of the full arrays of experimental data did not reveal any deviations from space group *P*321. When converting intensities into moduli of structure amplitudes, the data were corrected, apart from absorption, for the kinematic and polarization effects. All calculations were performed using the SDS program package [10]. Structure parameters were refined by the full-matrix least-squares method. In the experiments and calculations, the right-handed coordinate system was used. Crystal chirality was calculated for the full (not averaged) arrays of structure amplitudes, allowing the anisotropic extinction to be taken into account for the samples. Maximal corrections for the anomalous scattering of X-rays used in this work were observed for the Sr atoms. For this reason, the chirality of the $Sr_3Ga_2Ge_4O_{14}$ sample was determined more reliably than for the La compound.

Refinement of the original crystal structure of the Sr compound converged to the discrepancies (unweighed) $R = 5.65\%$ and (weighed) $R_w = 6.51\%$ between the experimental and model structure amplitudes. The weighing scheme used in all refinements was $w = 1/(\sigma F)^2$. Refinement of the inverted model converged to the smaller discrepancy factors: $R = 1.75\%$ and $R_w = 1.98\%$. Thus, the absolute structure of the crystal differs from the original structure [7] in chirality sign, so that the coordinates of the basis atoms in the right-handed coordinate system (table) correspond to the absolute atomic model of this crystal.

Analogous calculations for the $La_3Nb_{0.5}Ga_{5.5}O_{14}$ structure gave $R = 2.57\%$ and $R_w = 3.27\%$ for the original model [11] and $R = 3.38\%$ and $R_w = 4.23\%$ for the inverted model. In this case, the absolute structure corresponds to the original model.

Crystals of the langasite family have layered structure. The alternating layers of two types are perpendicular to the threefold axis. The cations at $z = 0$ are positioned in the two types of polyhedra: octahedra and the larger polyhedra shaped like distorted Thomson cubes. The second layer consists of two types of crystallographically independent tetrahedra. The z coordinate of cations in the tetrahedra of one of these types is exactly equal to 0.5, and it is close to this value in the second type (Fig. 1). The ionic radii of the largest cations La^{3+} and Sr^{2+} are 1.16 and 1.26 Å, respectively, and they occupy the Thomson cubes. The remaining (smaller) cations are distributed among the tetrahedra and octahedra in a certain way.

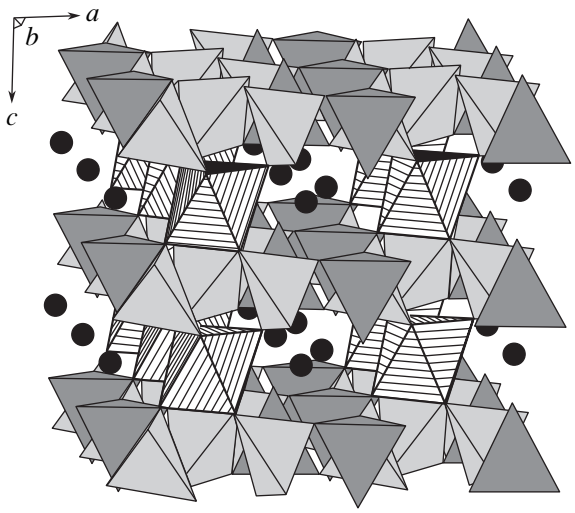

Fig. 1. Model of atomic structure of langasite. Layers of two types alternate perpendicularly to the crystal c axis; one is composed of the separate octahedra and large cations' and the other is composed of the crystallographically independent tetrahedra of two types.

In the original structure of $La_3Nb_{0.5}Ga_{5.5}O_{14}$, niobium and gallium (ionic radii of Nb^{5+} and Ga^{3+} are, respectively, 0.64 and 0.62 Å) randomly occupy octahedra (next-in-size polyhedra). The remaining gallium ions are positioned in the two types of tetrahedra. This model was proved by the least-squares refinement of the structure. The octahedron occupancy was found to be $(Nb_{0.50}Ga_{0.50})$. This was reliably established by the X-ray method, because the difference in the number of

Coordinates (in the right-handed system), point symmetries (S), site multiplicities (n), and equivalent thermal parameters (B) of the basis atoms in the $La_3Nb_{0.5}Ga_{5.5}O_{14}$ and $Sr_3Ga_2Ge_4O_{14}$ structures

Atoms	S	n	x/a	y/a	z/c	B
			$La_3Nb_{0.5}Ga_{5.5}O_{14}$			
La	2	3	0.42459(2)	0	0	0.678(3)
$(Nb_{0.50}Ga_{0.50})$	32	1	0	0	0	0.687(8)
Ga2	3	2	1/3	2/3	0.53124(7)	0.605(6)
Ga3	2	3	0.76176(4)	0	1/2	0.790(7)
O1	3	2	1/3	2/3	0.1784(5)	0.92(4)
O2	1	6	0.4563(3)	0.3088(3)	0.3054(3)	1.14(5)
O3	1	6	0.2188(3)	0.0773(3)	0.0727(3)	1.16(5)
			$Sr_3Ga_2Ge_4O_{14}$			
Sr	2	3	0.57683(2)	0	0	0.719(3)
$(Ge_{0.87}Ga_{0.13})$	32	1	0	0	0	0.650(4)
Ge	3	2	2/3	1/3	0.47974(4)	0.553(3)
$(Ge_{0.38}Ga_{0.62})$	2	3	0.23643	0	1/2	0.634(3)
O1	3	2	2/3	1/3	0.8187(3)	0.86(2)
O2	1	6	0.5408(1)	0.6994(1)	0.6687(2)	1.03(2)
O3	1	6	0.7874(1)	0.9132(1)	0.2301(2)	1.14(2)

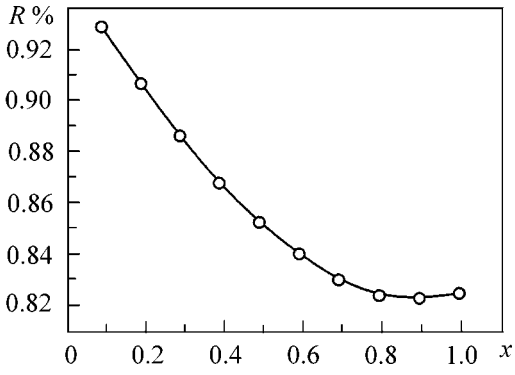

Fig. 2. Structure of $Sr_3Ga_2Ge_4O_{14}$. Least-squares refinement of occupancy factors for Ga and Ge in tetrahedra and octahedra with scan step $x = 0.1$. The minimum of the discrepancy factor R corresponds to the occupancy factor $x = 0.87$ for Ge in $(Ge_{0.87}Ga_{0.13})$ octahedron and the occupancy $(Ge_{0.38}Ga_{0.62})$ for each of the three tetrahedra.

electrons in these atoms Z(Ga) = 31 and Z(Nb) = 41 is large, while the X-ray scattering intensity is proportional to the square of this number. Next, a possible positional splitting (small difference in coordinates) was checked for the Ga and Nb atoms in octahedra, the only polyhedra in this structure that are randomly occupied by the atoms of two sorts. An analysis of the difference electron density map did not reveal any traces of splitting.

The identification of the Ga and Ge atoms in the $Sr_3Ga_2Ge_4O_{14}$ structure is hampered because of their neighborhood in the periodic table: Z(Ga) = 31 and Z(Ge) = 32. The ionic radii of these elements are r_0(Ga) = 0.62 Å and r_0(Ge) = 0.53 Å in the octahedral oxygen environment and r_1(Ga) = 0.47 Å and r_1(Ge) = 0.39 Å in the tetrahedra. The challenge was to distribute two Ga and two Ge atoms among one octahedron and three tetrahedra arranged on the twofold axes. The multiplicity values for Ga and Ge in the tetrahedra and octahedra were determined by least-squares refinement with a step-by-step scan [12]. The stoichiometric composition of the $Sr_3Ga_2Ge_4O_{14}$ crystal with 100% occupancies of all crystallographic sites was taken as a basis for occupancy refinement. The parameter x was scanned with step $\Delta x = 0.1$ in the range from 0 to 1.0. At each fixed x, all remaining structural parameters were refined by the least-squares method. The residual R as a function of occupancy factor (x) for Ge in the octahedral site is shown in Fig. 2. The discrepancy between the experimental and calculated structure amplitudes is minimal at $x = 0.87(9)$. Therefore, the octahedron occupancy is $(Ge_{0.87}Ga_{0.13})$, and the occupancies of each of the three tetrahedra are $(Ge_{0.38}Ga_{0.62})$. The final refinement of the structural models for the averaged arrays of experimental data containing, respectively, 1184 and 1149 independent structure amplitudes was performed by the least-squares method with the anisotropic thermal parameters in harmonic approximation and converged to residual R = 1.32% and R_w = 1.59% for $La_3Nb_{0.5}Ga_{5.5}O_{14}$ and R = 0.83% and R_w = 0.99% for $Sr_3Ga_2Ge_4O_{14}$. The total number of refined parameters was 37 for each structure. The final fractional atomic coordinates of the basis atoms, their equivalent isotropic thermal parameters B, and the symmetry and multiplicity of atomic positions are given in the table.

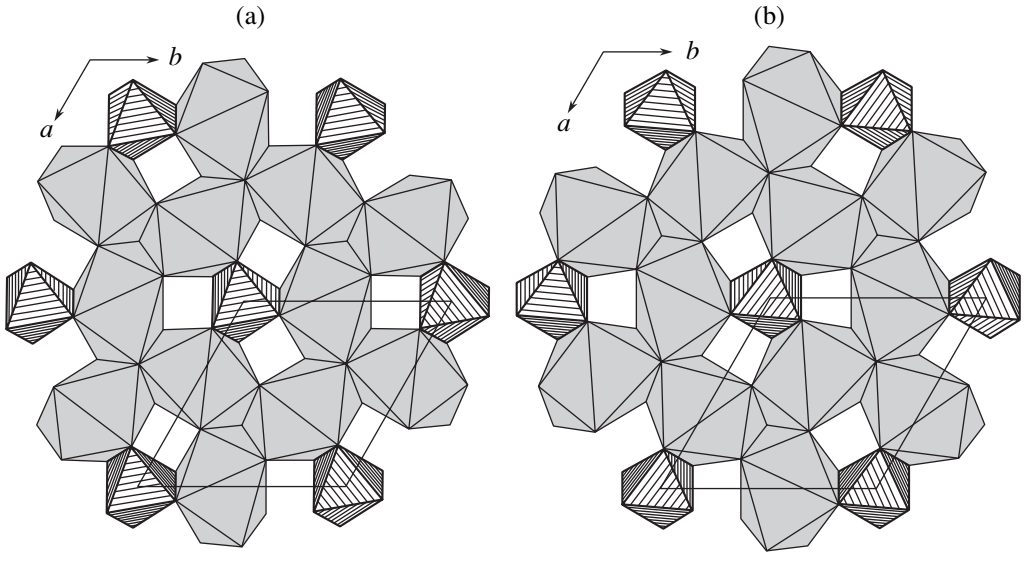

Fig. 3. Structure of (a) a layer of the $(Nb_{0.50}Ga_{0.50})$ octahedra and La polyhedra in the $La_3Nb_{0.5}Ga_{5.5}O_{14}$ structure and (b) a layer of the $(Ge_{0.87}Ga_{0.13})$ octahedra and Sr polyhedra in the $Sr_3Ga_2Ge_4O_{14}$ structure. The triangular octahedron faces perpendicular to the crystal c axis are turned (a) counterclockwise and (b) clockwise through different angles.

The space group *P*321 does not contain screw axes. The optical activity of langasites is caused by the special features of their atomic structure, namely, by the geometric configurations of octahedra and Thomson cubes. The structure of a layer composed of the ($Nb_{0.50}Ga_{0.50}$) octahedra and La polyhedra (Thomson cubes) in the $La_3Nb_{0.5}Ga_{5.5}O_{14}$ structure is shown in Fig. 3a. The analogous layer of the ($Ge_{0.87}Ga_{0.13}$) octahedra and Si polyhedra in the $Sr_3Ga_2Ge_4O_{14}$ structure is shown in Fig. 3b. In a regular centrosymmetric octahedron, the opposing faces (regular triangles) are turned through 60° relative to each other. One can see from Figs. 3a and 3b that the upper regular triangular face of the octahedron in the structure with lanthanum is turned counterclockwise through 19.3° from its position in a regular centrosymmetric octahedron. In the $Sr_3Ga_2Ge_4O_{14}$ structure, the analogous turn in the layer is clockwise and equals 12.1°. The absolute values of specific rotation for the wavelength $\lambda = 0.55$ μm are equal in these crystals to 16.8 and 4.42 deg/mm, respectively [8]. Thus, the specific rotation of the crystals studied correlates with the degree of deviation from the centrosymmetric configuration of an octahedron structure.

We are deeply indebted to B.V. Mill for growing and kindly providing us with high-quality $La_3Nb_{0.5}Ga_{5.5}O_{14}$ and $Sr_3Ga_2Ge_4O_{14}$ crystals. We are also grateful to him for active and fruitful discussion of the results. This work was supported by the Russian Foundation for Basic Research (project no. 99-02-17242) and the Leading Scientific School (project no. 00-15-96633).

REFERENCES

1. E. L. Belokoneva, M. A. Simonov, A. V. Butashin, *et al.*, Dokl. Akad. Nauk SSSR **255**, 1099 (1980) [Sov. Phys. Dokl. **25**, 954 (1980)].
2. B. V. Mil', A. V. Butashin, A. M. Éllern, and A. A. Maĭer, Izv. Akad. Nauk SSSR, Neorg. Mater. **17**, 1648 (1981).
3. I. A. Andreev and M. F. Dubovik, Pis'ma Zh. Tekh. Fiz. **10**, 487 (1984) [Sov. Tech. Phys. Lett. **10**, 205 (1984)].
4. E. L. Belokoneva, S. Yu. Stefanovich, Yu. V. Pisarevskiĭ, and A. V. Mogunov, Zh. Neorg. Khim. **45**, 1786 (2000).
5. B. V. Mill and Yu. V. Pisarevsky, in *Proceedings of the International IEEE Frequency Control Symposium, Kansas City, 2000*, p. 133.
6. I. M. Sil'vestrova, Yu. V. Pisarevskiĭ, B. V. Mill', and A. A. Kaminskiĭ, Dokl. Akad. Nauk SSSR **283**, 575 (1985).
7. A. A. Kaminskii, E. L. Belokoneva, B. V. Mill, *et al.*, Phys. Status Solidi A **86**, 345 (1984).
8. O. A. Baturina, B. N. Grechushnikov, A. A. Kaminskiĭ, *et al.*, Kristallografiya **32**, 406 (1987) [Sov. Phys. Crystallogr. **32**, 236 (1987)].
9. *International Tables for Crystallography*, Ed. by A. J. C. Wilson (Kluwer, Dordrecht, 1992), Vol. C, p. 219.
10. V. Petricek, *Computing System SDS*, Ed. by C. Novak (Czech Academy of Sciences, Prague, 1994).
11. A. A. Kaminskiĭ, B. V. Mill', E. L. Belokoneva, *et al.*, Izv. Akad. Nauk SSSR, Neorg. Mater. **20**, 2058 (1984).
12. T. S. Chernaya, N. N. Bydanov, L. A. Muradyan, *et al.*, Kristallografiya **33**, 75 (1988) [Sov. Phys. Crystallogr. **33**, 40 (1988)].

Translated by V. Sakun

JETP Letters, Vol. 74, No. 4, 2001, pp. 226–230. Translated from Pis'ma v Zhurnal Éksperimental'noĭ i Teoreticheskoĭ Fiziki, Vol. 74, No. 4, 2001, pp. 248–252.

Singularity in High-Frequency Susceptibility of Thin Magnetic Films with Uniaxial Anisotropy

B. A. Belyaev[1]*, A. V. Izotov[1], and S. Ya. Kiparisov[2]

[1] *Kirenskiĭ Institute of Physics, Siberian Division, Russian Academy of Sciences, Akademgorodok, Krasnoyarsk, 660036 Russia*

[2] *Kristall NIITs, Krasnoyarsk State University, Krasnoyarsk, 660062 Russia*

* *e-mail: belyaev@iph.krasn.ru*

Received July 24, 2001

A sharp peak of magnetic susceptibility has been observed in the ferromagnetic resonance spectra of uniaxial magnetic films placed in a planar field directed orthogonal to the easy magnetization axis, along which a pumping high-frequency magnetic field has been oriented. The peak width is considerably narrower than the line width of the uniform ferromagnetic resonance, and its position in a field equal to the film anisotropy field does not depend on the pumping frequency. The nature of the peak is associated with a drastic increase in the static transverse susceptibility of the film in the vicinity of the anisotropy field. It is shown phenomenologically that the peak can be observed only for quality samples with small angular and amplitude dispersion of the uniaxial anisotropy. © *2001 MAIK "Nauka/Interperiodica"*.

PACS numbers: 75.70.Ak; 76.50.+g; 75.30.Cr

It is known that one or two resonance peaks, depending on the pumping frequency, are observed in the ferromagnetic resonance (FMR) spectrum of magnetic films in the single-domain state possessing uniaxial magnetic in-plane anisotropy when a planar magnetic field is swept perpendicular to the easy magnetization axis (EMA) [1].The magnitude of the resonance fields for these peaks can be determined from the equations

$$\left(\frac{\omega}{\gamma}\right)^2 = \left(\frac{H_k^2 - H^2}{H_k}\right)(4\pi M_s + H_k), \quad H \le H_k,$$
$$\left(\frac{\omega}{\gamma}\right)^2 = (H - H_k)(4\pi M_s + H_k), \quad H \ge H_k, \qquad (1)$$

where ω is the circular frequency of the pumping magnetic field, γ is the gyromagnetic ratio, H_k is the uniaxial magnetic anisotropy field, H is the FMR field, and M_s is the saturation magnetization.

We found another sharp peak in the FMR spectra of magnetic Co–Ni–P films. Its line width was an order of magnitude smaller than the line width of the uniform ferromagnetic resonance. The spectra were measured from local areas of samples on an automated scanning FMR spectrometer [2]. The locality of measurements was determined by the diameter of the measuring hole in the microstrip resonator of the detector with an area of ≈1 mm^2.

Magnetic films 0.05–1.0 μm thick were obtained by chemical deposition from a solution [3] at a temperature of 96–97°C on substrates 10 × 10 mm^2 in size. Glasses, fused quartz, and single-crystal GaAs wafers were used as substrate materials, and the structure of the films was X-ray amorphous, regardless of the substrate material. Microstructural studies of films were performed on a PRÉM-200 electron transmission microscope. These studies showed that a film consisted of microcrystallites 20–60 Å in size. The film composition was measured in the range $Co_{65–70}$–$Ni_{32–27}P_{3–5}$ wt % and was controlled by X-ray fluorescence analysis [4]. A planar uniaxial magnetic anisotropy field H_k = 25–30 Oe was induced by a uniform magnetic field H = 3 kOe applied in the substrate plane during film deposition. Measurements of magnetic properties in local areas of samples [5] showed their high uniformity in the central part ~6 × 6 mm^2 in size. For example, the effective saturation magnetization for a sample 0.3 μm thick varied from point to point within the range as small as M_s = 1100 ± 20. The deviation of the directions of the easy magnetization axes in local areas of the film did not exceed ±0.4°, and the deviation of the anisotropy field from the average H_k = 28 Oe was less than 0.5 Oe. Ferromagnetic resonance spectra measured for this sample at three pumping frequencies in its central area

0021-3640/01/7404-0226$21.00 © 2001 MAIK "Nauka/Interperiodica"

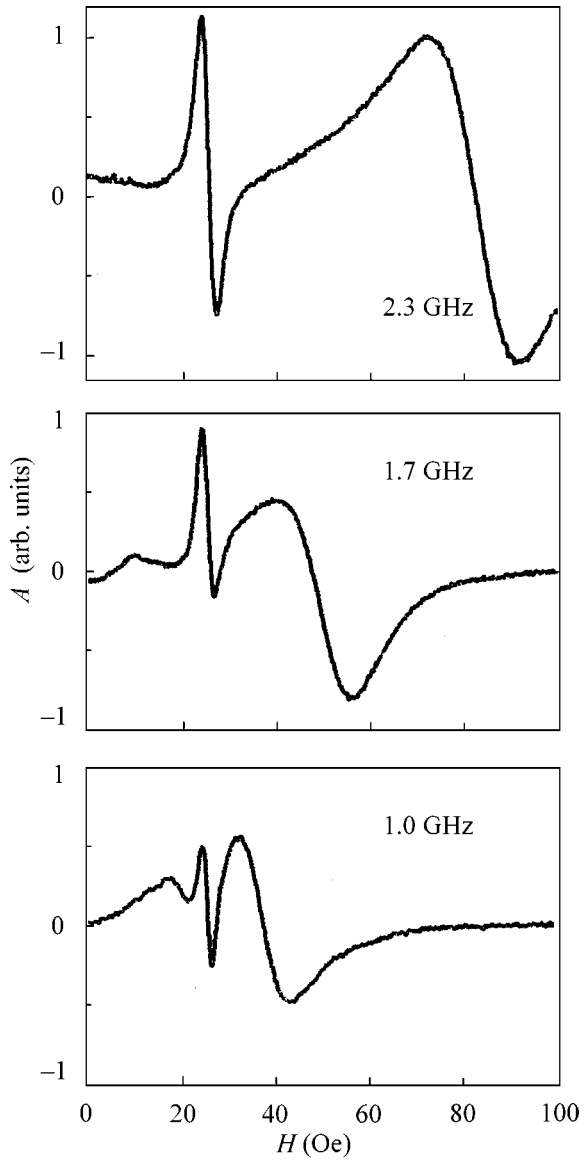

Fig. 1. Ferromagnetic resonance spectra at various pumping frequencies.

are presented in Fig. 1. The magnetic field in the experiment was oriented strictly perpendicular to the easy magnetization axis. Regardless of the pumping frequency, an intense sharp peak is observed in all spectra at the same magnetic field equal to the uniaxial magnetic anisotropy field H_k = 28 Oe. Its width is considerably smaller than the line width of the uniform magnetic resonance. The dependences of the resonance frequency of the uniform ferromagnetic resonance for the sample area under study calculated by the formulas in Eq. (1) are shown in Fig. 2. Points present the results of measurements. The vertical dashed line connects the points corresponding to the maximal susceptibility of the new peak found in the FMR spectrum. It should be

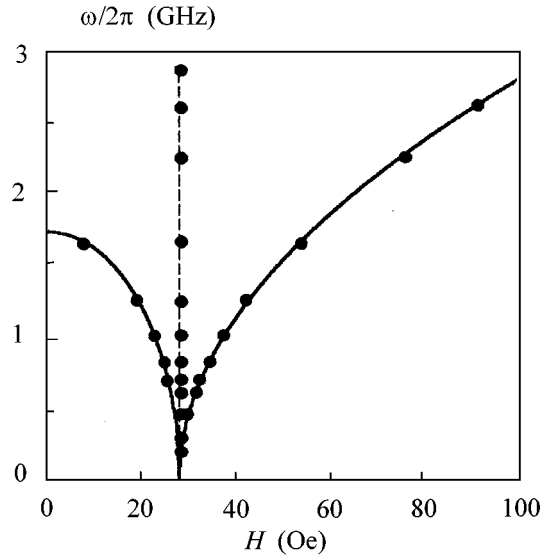

Fig. 2. Dependence of the resonance frequencies on the FMR field.

noted that the amplitude of this peak drops rapidly with decreasing pumping frequency below 1 GHz because of its suppression by the uniform ferromagnetic resonance peaks moving closer together. As a result, this peak is hardly observed at a frequency of 0.2 GHz. With increasing pumping frequency above 2.6 GHz, the peak amplitude drops monotonically; this, evidently, can be explained by the manifestation of the skin effect. It is also important to note that the peak found in our work virtually disappears if the easy magnetization axis deviates from the orthogonality to the field H in one or another direction by only 1° (Fig. 3).

The revealed regularities in the behavior of the peak found in this work allow the suggestion that its nature is associated with the static susceptibility of the magnetic film. Actually, a kink is observed in the curve of film magnetization perpendicular to the EMA at a magnetic field equal to the anisotropy field of the sample [1]. This kink demonstrates instability of the magnetic moment at this point. Therefore, it is reasonable to expect here an increase in the transverse magnetic susceptibility.

Consider a model of an infinite magnetic film in the x–y plane, in which an external magnetic field H is directed at an angle θ_H to the x axis, and the easy magnetization axis of uniaxial magnetic anisotropy is directed at an angle θ_n to x. In this case, the equilibrium angle θ_M that characterizes the slope of the magnetization vector M_s to the x axis is determined from the equation

$$H\sin(\theta_H - \theta_M) + \frac{1}{2}H_k \sin 2(\theta_n - \theta_M) = 0. \qquad (2)$$

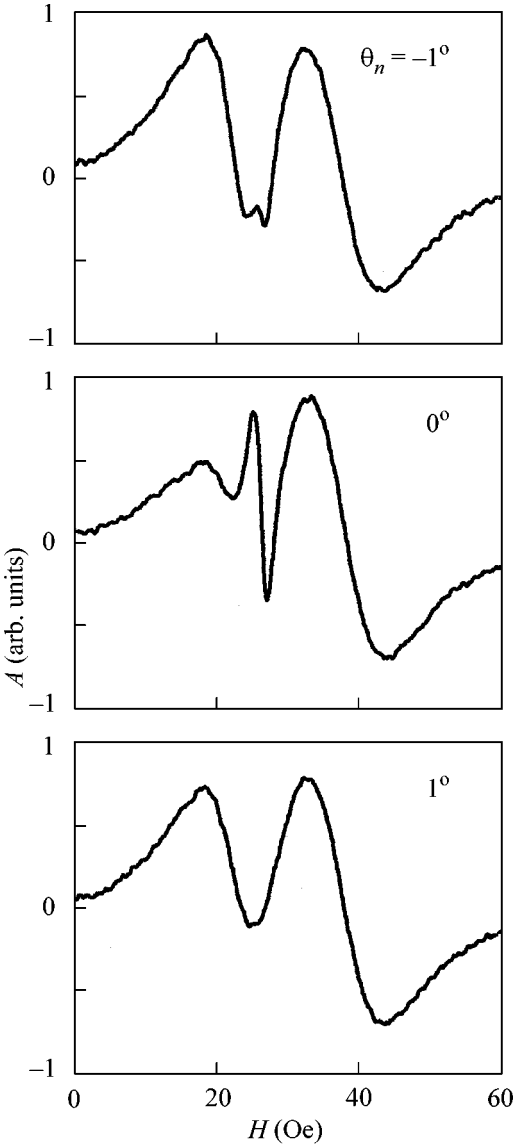

Fig. 3. FMR spectra for various orientation angles of the easy magnetization axis.

Equation (2) is obtained from the minimum condition for the free energy density of the film

$$F = -(\mathbf{M}\cdot\mathbf{H}) + \frac{1}{2}(\mathbf{M}\cdot\overleftrightarrow{N}\cdot\mathbf{M}) - \frac{H_k}{2M}(\mathbf{M}\cdot\mathbf{n})^2. \quad (3)$$

Here, **M** is the magnetic moment vector, **n** is the unit vector that coincides with the EMA direction, and $\overleftrightarrow{N}$ is the tensor of demagnetization coefficients. This tensor is determined by the shape of the sample, and it has only one component $N_{zz} = 4\pi$ in the case of a magnetic film.

The static magnetic susceptibility of the film

$$\chi = m/h, \quad (4)$$

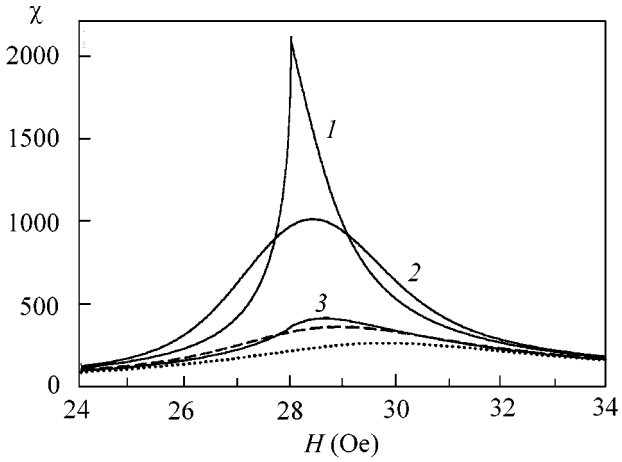

Fig. 4. Field dependences of magnetic susceptibility calculated numerically: (*1*) without anisotropy dispersion, (*2*) only amplitude dispersion of 1 Oe, and (*3*) only angular dispersion of 1°; dashed line designates that both angular and amplitude dispersions are present; and dots mean that dispersion is absent, but the EMA deviates by 1° from the initial direction.

where *m* is the deviation of the magnetization vector from an equilibrium under the action of a test magnetic field *h*. It can be calculated from the solution of the equation

$$[\mathbf{M}\times\mathbf{H}_{\text{eff}}] = 0, \quad (5)$$

where $\mathbf{H}_{\text{eff}} = dF/d\mathbf{M}$. This equation is reduced to an equation of the third degree in the quantity $\psi = m/M_s$. In the general case, this equation takes the form

$$\psi^3 + \frac{h\cos(\theta_H-\theta_M) + H_k\sin 2(\theta_n-\theta_M)}{H_k\sin^2(\theta_n-\theta_M)}\psi^2$$
$$+ 2\frac{H\cos(\theta_H-\theta_M) + H_k\cos 2(\theta_n-\theta_M) - h\sin(\theta_H-\theta_M)}{H_k\sin^2(\theta_n-\theta_M)} \quad (6)$$
$$\times\psi = 2\frac{h\cos(\theta_H-\theta_M)}{H_k\sin^2(\theta_n-\theta_M)}.$$

The dependence of the transverse magnetic susceptibility of the film on the external magnetic field (curve *1*) obtained by numerically solving Eq. (6) is presented in Fig. 4 for the case $\theta_H = \pi/2$ and $\theta_n = 0$. The following parameters of the film area, the experimental results for which are presented in Figs. 1–3, were used in the calculations: saturation magnetization M_s = 1100 G, anisotropy field H_k = 28 Oe, test field h = 0.1 Oe. It is evident that the calculated curves, as well as the experimental data, exhibit a pronounced sharp peak of susceptibility at a magnetic field equal to the anisotropy field. Moreover, as well as in the experimental results, the calculation indicates that the peak of susceptibility almost disappears if the easy axis deviates

by only one degree ($\theta_n = \pm 1°$) from the initial direction ($\theta_n = 0$) (see the dotted line in Fig. 4.) Our investigations also showed that the susceptibility monotonically grows as the anisotropy field decreases. It follows from these facts that both the angular and amplitude dispersions of uniaxial magnetic anisotropy must affect the susceptibility peak [6]. These dispersions may be significant in real samples because of imperfections in the technology of their preparation.

In order to estimate the anisotropy dispersion effect on the peak of magnetic susceptibility, we will use a Gaussian distribution for both the anisotropy field H_k and the direction of the easy magnetization angle θ_n [7]. The dependences of the transverse magnetic susceptibility on the external magnetic field also obtained by numerical calculations are shown in Fig. 4 for the cases when only the amplitude anisotropy dispersion Δ_k = 1 Oe (curve *2*), only the angular anisotropy dispersion $\Delta_\theta = 1°$ (curve *3*), and both the angular and amplitude dispersions of the same values (dashed line) are present in the film. It is evident that, if even a small angular dispersion of the uniaxial magnetic anisotropy occurs in the sample, the susceptibility peak under study almost disappears. This proves the fact that the effect found in this work can be observed only in high-quality samples. It should also be noted that a dispersion of anisotropy shifts the film susceptibility maximum toward the region of higher fields.

Note that, under the condition that $|H - H_k| \gg h$, the terms of the second order of smallness can be neglected when Eq. (5) is solved for the case when $\theta_H = \pi/2$ and $\theta_n = 0$ in the absence of the dispersion of uniaxial magnetic anisotropy.

Finally, we obtain

$$\chi \approx \frac{M_s H}{H_k^2 - H^2}, \quad H < H_k, \tag{7}$$

$$\chi \approx \frac{M_s}{H - H_k}, \quad H > H_k. \tag{8}$$

It is seen from Eqs. (7) and (8) that the dependence $\chi(H)$ in the region of "weak" fields is stronger than the same dependence in the region of "high" fields. This explains the asymmetry of the right and left slopes observed in the field dependence of the susceptibility numerically calculated without approximations (see Fig. 4). It is interesting that the occurrence of an amplitude dispersion in the magnetic anisotropy of the film decreases the asymmetry of the slopes of the $\chi(H)$ curve.

In the case when $H = H_k$, Eq. (6), under the condition that $\theta_H = \pi/2$ and $\theta_n = 0$, takes the simple form

$$\psi^3 + \frac{h}{H_k}\psi^2 = 2\frac{h}{H_k}. \tag{9}$$

Taking into account that $\psi = m/M_s$ and $h/H_k \ll 1$, we obtain the equation for the maximal susceptibility

$$\chi_{\max} \approx M_s \sqrt[3]{\frac{2}{H_k h^2}}. \tag{10}$$

Approximate Eq. (10) indicates that the maximal magnetic susceptibility decreases as $(h)^{-2/3}$ with increasing test field, and it decreases as $(H_k)^{-1/3}$ with increasing uniaxial magnetic anisotropy field. These regularities were confirmed sufficiently well by numerical calculations carried out without approximations.

Thus, a theoretical analysis showed that the narrow susceptibility peak found in the FMR spectrum is due to a drastic increase in the static transverse magnetic susceptibility of the film at the point of the instability of the magnetic moment observed in the field $H = H_k$. In this field, a kink is observed in the magnetization curve [1], which is leveled off with increasing angular and amplitude dispersion of anisotropy. The calculation also showed that the susceptibility peak almost disappears when the angular dispersion of the anisotropy field $\geq 1°$. Therefore, in spite of the high quality of the obtained films, the effect is revealed only in the local areas of samples where the dispersion of anisotropy is sufficiently small. A signal due to static susceptibility is also seen in Permalloy films with uniaxial magnetic anisotropy that were obtained by vacuum sputtering in a magnetic field. However, its amplitude is almost two orders of magnitude smaller than the amplitude of the uniform ferromagnetic resonance signal. This is explained by the relatively high angular dispersion of anisotropy in these films.

It is important to note that the effect of an increase in static susceptibility in the field $H = H_k$ found in this work can be observed only at relatively high frequencies in the microwave range when the resonance fields of the uniform ferromagnetic resonance peaks are sufficiently distant from H_k (see Fig. 2). As the pumping frequency decreases, the uniform ferromagnetic resonance approaches the static susceptibility peak and suppresses it.

In our opinion, the static susceptibility peak studied in this work provides an explanation for the sharp increase in amplitude of the nuclear magnetic resonance signal observed in anisotropic cobalt films [8, 9]. This effect was also observed in the field equal to the anisotropy field when a film was magnetized perpendicular to the easy magnetization axis. In this case, the signal virtually disappeared when the magnetic field deviated from the orthogonal direction by only 1°.

The authors are grateful to V.A. Ignatchenko for a fruitful discussion of the results of this work.

REFERENCES

1. N. M. Salanskiĭ and M. Sh. Erukhimov, *Physical Properties and Application of Magnetic Films* (Nauka, Novosibirsk, 1975).
2. B. A. Belyaev, A. A. Leksikov, I. Ya. Makievskiĭ, and V. V. Tyurnev, Prib. Tekh. Éksp., No. 3, 106 (1997).
3. S. Ya. Kiparisov, USSR Inventor's Certificate No. 1145050, Byull. Izobret., No. 10 (1985).
4. G. V. Bondarenko and A. P. Dolgarev, in *Apparatus and Methods of X-ray Analysis* (Mashinostroenie, Leningrad, 1983), pp. 128–132.
5. B. A. Belyaev, A. V. Izotov, and A. A. Leksikov, Zavod. Lab. **67** (9), 23 (2001).
6. M. Prutton, *Thin Ferromagnetic Films* (Butterworths, London, 1964; Sudostroenie, Leningrad, 1967).
7. A. G. Lesnik, Fiz. Met. Metalloved. **27**, 1000 (1969).
8. N. V. Baksheev and É. S. Mushailov, Fiz. Tverd. Tela (Leningrad) **21**, 2801 (1979) [Sov. Phys. Solid State **21**, 1612 (1979)].
9. E. M. Artem'ev, N. V. Baksheev, and É. S. Mushailov, Fiz. Met. Metalloved. **53**, 1224 (1982).

Translated by A. Bagatur'yants

JETP Letters, Vol. 74, No. 4, 2001, pp. 231–234. Translated from Pis'ma v Zhurnal Éksperimental'noĭ i Teoreticheskoĭ Fiziki, Vol. 74, No. 4, 2001, pp. 253–257.

Conductivity of Wigner Liquid

É. G. Batyev

Institute of Semiconductor Physics, Siberian Division, Russian Academy of Sciences, pr. akademika Lavrent'eva 13, Novosibirsk, 630090 Russia

e-mail: batyev@isp.nsc.ru

Received July 23, 2001

The conductivity of two-dimensional electron systems with low carrier concentration is considered on the basis of the previously suggested model (Fermi liquid with a soft mode) under the assumption that the equilibrium in each of the (fermion and boson) subsystems is established faster than the impurity relaxation and the relaxation between the subsystems (hydrodynamic approximation). The conductivity of the system depends on three characteristic times: $\tau_1(\tau_2)$ is determined by the fermion (boson) impurity scattering and τ_{12} is determined by the friction between the subsystems; the respective temperature dependences are obtained. The conductivity is related to the relaxation time τ in the usual way, and τ obeys the relationship $\tau^{-1} = \tau_1^{-1} + (\tau_2 + \tau_{12})^{-1}$. It follows from the results obtained that the resistivity of pure samples should increase with temperature and tend towards saturation. © *2001 MAIK "Nauka/Interperiodica".*

PACS numbers: 71.27.+a; 71.30.+h

In recent years, experimental and theoretical studies have emerged which are devoted to the two-dimensional low-density electron systems undergoing metal–insulator transition upon lowering the concentration of charge carriers. Various explanations were offered for this phenomenon and for the temperature, concentration, and magnetic-field dependences of conductivity (see review [1]). In many works, an important role of Coulomb interaction between carriers is emphasized; estimates suggest that this interaction may become stronger than the Fermi energy, and this fact is used, in one way or another, by many authors (see paper [2], which is not cited in review [1]).

In such a system, the correlation effects are *a fortiori* strong, and one can assert that, as in a Wigner crystal, there is a short-range order in the carrier arrangement, so that this system can be referred to as a Wigner liquid. It is natural to expect that this fact should manifest itself in the spectrum of elementary excitations, and the question is what these manifestations are. In [3], the idea is proposed that a new elementary excitation branch, a so-called "soft mode," may appear in such a system, so that, in addition to the Fermi-type excitations (fermions) that are inherent in Fermi liquids, low-energy Bose-type excitations with finite momenta may appear. The number of new excitations (bosons) and, hence, their contribution to the resistance depend on temperature, as was demonstrated in [3] for the simplest model of the system.

To gain more insight into the influence of bosons on the kinetic and other properties of the system, one should realize how the problem can be formulated in more general form than that in [3]. The corresponding phenomenological model was suggested in [4], where the temperature dependences of the equilibrium quasiparticle spectra were calculated. The results obtained in [4] are used in this work with the object of determining the temperature dependence of resistance in the metallic state.

Equations of motion. The problem is not only that there are two subsystems whose properties depend on temperature but also that the quasiparticle energy changes when the system moves, as contrasted to an ideal gas. This occurs in every system where interaction plays an important role. For example, in the Landau theory of Fermi liquid, the fermion energy for the moving system transforms as

$$\xi_{\mathbf{p}} \longrightarrow \tilde{\xi}_{\mathbf{p}} = \xi_{\mathbf{p}} + (\mathbf{pu})\left(1 - \frac{m}{m^*}\right), \qquad (1)$$

where $\xi_{\mathbf{p}}$ is the fermion energy in the system at rest, $\mathbf{u}$ is the liquid velocity, m is the mass of bare fermions, and m^* is the fermion effective mass that differs from m due to the interaction between particles. The energy refers to the rest (laboratory) frame.

In the soft-mode model, the above relationship is modified because of the influence of bosons, for which this effect should also be taken into account. This problem is solved by introducing the terms allowing for the motion of different subsystems, which is specified by the sum of operators H_3 and H_4 defined in [4], namely,

$$H_3 + H_4 \longrightarrow \frac{1}{V}\sum_{\mathbf{p},\,\mathbf{q}} \delta n(\mathbf{p}) \frac{(\mathbf{pq})}{\rho} \beta_{\mathbf{q}}^{+} \beta_{\mathbf{q}}$$

0021-3640/01/7404-0231$21.00

$$+\frac{1}{V}\sum_{\mathbf{q}',\mathbf{q}}\langle\beta^+_{\mathbf{q}'}\beta_{\mathbf{q}'}\rangle\frac{(\mathbf{q}'\mathbf{q})}{\rho}\beta^+_{\mathbf{q}}\beta_{\mathbf{q}}, \qquad (2)$$

$$\rho = mn, \quad n = \kappa p_F^2/4\pi$$

(the constant term is omitted). The following notation is used in Eq. (2): $\delta n(\mathbf{p})$ is the difference between the fermion distribution function and the equilibrium function; $\beta^+_{\mathbf{q}}(\beta_{\mathbf{q}})$ is the boson creation (annihilation) operator; the symbol $\langle\ldots\rangle$ denotes averaging over the system state; n is the carrier concentration; p_F is the Fermi momentum; and V is the volume (area) of the system. The summation over momenta includes also the summation over the fermion spin and the valley number (in the multivalley case), and the multiplier κ in the expression for n corresponds to the multiplicity of level degeneracy {$\kappa = 4$ for the (100) Si MOSFET surface: two spin projections and two valleys [1]}. It is assumed that the fermion distribution function is independent of spin (the magnetic field is absent) and of valley number Expressions (2) are in excess of what is inherent in the ordinary Fermi liquid and leads to Eq. (1).

Using Eq. (2) and the Fermi liquid correction of type (1), one obtains the following expressions, instead of the equilibrium fermion $\xi_{\mathbf{p}}$ and boson $\omega_{\mathbf{p}}$ energies:

$$\tilde{\xi}_{\mathbf{p}} = \xi_{\mathbf{p}} - (\mathbf{p}\mathbf{u}_1) + (\mathbf{p}\mathbf{u}), \quad \tilde{\omega}_{\mathbf{q}} = \omega_{\mathbf{q}} + (\mathbf{q}\mathbf{u});$$
$$\rho_1\mathbf{u}_1 = \mathbf{P}_1, \quad \rho\mathbf{u} = \mathbf{P}, \quad \rho_1 = \frac{m^*}{m}\rho. \qquad (3)$$

Here, $\mathbf{P}$ is the density (i.e., per unit area) of the total momentum and $\mathbf{P}_1$ is the momentum density in the fermion subsystem. These results depend only on the cited characteristics and not on the particular form of corrections to the distribution functions.

Let us simplify the problem. One of the possible ways is to assume that the fermion $n_{\mathbf{p}}$ and boson $N_{\mathbf{q}}$ distribution functions are known. We specify them as

$$n_{\mathbf{p}} = \left[\exp\left(\frac{\xi_{\mathbf{p}} - \mathbf{p}\mathbf{u}_1}{T}\right) + 1\right]^{-1},$$
$$N_{\mathbf{q}} = \left[\exp\left(\frac{\omega_{\mathbf{q}} - \mathbf{q}\mathbf{u}_2}{T}\right) - 1\right]^{-1}, \qquad (4)$$

where the fermion energy $\xi_{\mathbf{p}}$ is measured from the Fermi energy (a change in the chemical potential is quadratic in velocity $\mathbf{u}_1$ and, hence, can be ignored). Equations (4) are valid in the hydrodynamic approximation, which implies that the equilibrium in each of the subsystems (fermion and boson) is established faster than the impurity relaxation and the relaxation between the subsystems. However, the results obtained for the conductivity prove to be correct in the low- and high-temperature limits, irrespective of whether this approximation is valid or not.

The relationship between the momentum density $\mathbf{P}_2$ in a magnon subsystem and the velocity $\mathbf{u}_2$ is taken in the form

$$\mathbf{P}_2 = \mathbf{P} - \mathbf{P}_1 = \rho_2\mathbf{u}_2, \qquad (5)$$

where the quantity ρ_2 could be called the boson normal component if the system was superfluid.

Let us now write the equations of motion. One of them has the following general form:

$$\frac{\partial\mathbf{P}}{\partial t} = \left(\frac{\partial\mathbf{P}}{\partial t}\right)_i + ne\mathbf{E}, \qquad (6)$$

where e is the charge and $\mathbf{E}$ is the electric field. The first term on the right-hand side stands for a change in momentum due to the quasiparticle collisions with impurities. Let us first consider this contribution for fermions. For the equilibrium distribution function with energy $\tilde{\xi}_{\mathbf{p}}$ given by Eq. (3), this contribution is zero. In actuality, the fermion distribution function is different [see Eq. (4)], so that the desired term is proportional to the difference in momenta corresponding to these two distributions. The result can conveniently be written as

$$\left(\frac{\partial\mathbf{P}_1}{\partial t}\right)_i = -\frac{1}{\tau_1}\rho\mathbf{u}. \qquad (7)$$

Analogous considerations for bosons give

$$\left(\frac{\partial\mathbf{P}_2}{\partial t}\right)_i = -\frac{1}{\tau_2}\rho(\mathbf{u} + \mathbf{u}_2). \qquad (8)$$

In deriving these relationships, the velocity dependence was written in the explicit form, and the rest of the expression was written so that the possible temperature dependences are contained only in the relaxation times τ_1 and τ_2, which will further enter the expression for conductivity.

After Eq. (6) is specified, we can write the equation for the boson momentum. In doing so, one should take into account that bosons are subject only to the friction forces (due to the interaction with impurities and fermions) and not to the electric field. The corresponding equation is

$$\frac{\partial\mathbf{P}_2}{\partial t} = \left(\frac{\partial\mathbf{P}_2}{\partial t}\right)_i + \left(\frac{\partial\mathbf{P}_2}{\partial t}\right)_1, \qquad (9)$$

where the second term on the right-hand side corresponds to the friction with fermions. To determine the form of this contribution, note that it vanishes at $\mathbf{u}_2 = 0$ from the general considerations, as also follows from the energy conservation law in collisions of fermions and bosons with energies (3). For this reason, this contribution is proportional to $\mathbf{u}_2$, and, similar to Eqs. (7) and (8), it can be written as

$$\left(\frac{\partial\mathbf{P}_2}{\partial t}\right)_1 = -\frac{1}{\tau_{12}}\rho\mathbf{u}_2. \qquad (10)$$

Collecting together Eqs. (6)–(10) and passing from momenta to velocities using Eqs. (3) and (5), one arrives at the following equations in the homogeneous case:

$$\frac{\partial \mathbf{u}}{\partial t} + \left(\frac{1}{\tau_1} + \frac{1}{\tau_2}\right)\mathbf{u} + \frac{1}{\tau_2}\mathbf{u}_2 = \frac{e}{m}\mathbf{E},$$
$$\frac{\rho_2}{\rho}\frac{\partial \mathbf{u}_2}{\partial t} + \left(\frac{1}{\tau_2} + \frac{1}{\tau_{12}}\right)\mathbf{u}_2 + \frac{1}{\tau_2}\mathbf{u} = 0. \quad (11)$$

It is straightforward to obtain expressions for the current density ($\mathbf{j} = ne\mathbf{u}$) and the conductivity σ; in the stationary case,

$$\sigma = \frac{ne^2\tau}{m}, \quad \frac{1}{\tau} = \frac{1}{\tau_1} + \frac{1}{\tau_2 + \tau_{12}}. \quad (12)$$

An unusual combination of two times ($\tau_2 + \tau_{12}$) in this expression is noteworthy. Nevertheless, it must be so, because if one of these times tends towards infinity, then the boson characteristics must not affect conductivity. The fact that this condition is met in Eq. (12) gives evidence for the validity of the result. If one of these times tends towards zero, one also obtains the expected result.

It is seen from Eqs. (11) that the expression for conductivity $\sigma(\nu)$ in an alternating field with frequency ν can be obtained upon substituting in Eq. (12)

$$\sigma \longrightarrow \sigma(\nu), \quad \frac{1}{\tau_1} \longrightarrow \frac{1}{\tau_1} - i\nu, \quad \frac{1}{\tau_{12}} \longrightarrow \frac{1}{\tau_{12}} - i\nu\frac{\rho_2}{\rho}.$$

Temperature dependences. Let us start with the boson relaxation time τ_2. This quantity was considered in [3], where the expression for τ_m was obtained for the bare boson spectrum $\Omega_{\mathbf{q}}$. In the case at hand, this expression is also valid, though for the renormalized spectrum [4], i.e., upon substituting $\Omega_{\mathbf{q}} \longrightarrow \omega_{\mathbf{q}}$. This gives for τ_2

$$\frac{1}{\tau_2} \approx \frac{1}{\tau_2(0)}[\exp(\omega_0/T) - 1]^{-1},$$
$$\frac{1}{\tau_2(0)} \equiv \frac{n_i}{n}\frac{q_0^2}{\pi m}. \quad (13)$$

Here, n_i is the impurity concentration and ω_0 and q_0 are the parameters of the renormalized boson spectrum,

$$\omega_{\mathbf{q}} = \sqrt{\omega_0^2 + v_0^2(q - q_0)^2}.$$

The expression for τ_2 deduced in [3] is valid if the interaction with impurities is strong enough (but the impurity concentration is low to provide high mobility); such a situation likely occurs for two-dimensional electrons in metal–insulator–semiconductor structures (e.g., Si MOSFET [1]), but the general case will not be discussed in this work.

Let us turn to the fermion relaxation time τ_1. Assume that it is known at zero temperature, $\tau_1(0)$. Then the temperature dependence of τ_1 appears due to the effective mass m^*, which differs from the zero-temperature effective mass m_0^* [4] and enters the expression for the fermion relaxation time quadratically. Thus, one has

$$\frac{1}{\tau_1} = \left(\frac{m^*}{m_0^*}\right)^2 \frac{1}{\tau_1(0)}. \quad (14)$$

The effective mass squared appears for the following reasons. Equation (7) for the fermion distribution function (4) can be deduced if the momentum relaxation caused by impurity scattering obeys the Fermi "golden rule" (as, e.g., it was assumed for bosons in [3]). The corresponding expression includes a double sum over the fermion (initial and final) momenta, so that the square of effective mass appears after passing to the integration with respect to energies.

Let us now turn to τ_{12}. To calculate a change in the boson momentum owing to the interaction with fermions [Eq. (10)], it is convenient to apply the Fermi golden rule. The corresponding expression is

$$\left(\frac{\partial \mathbf{P}_2}{\partial t}\right)_1 = \frac{2\pi\kappa}{V}\sum_{\mathbf{p}+\mathbf{q}=\mathbf{p}'+\mathbf{q}'} |M|^2(\mathbf{q}' - \mathbf{q})$$
$$\times n_{\mathbf{p}}(1 - n_{\mathbf{p}'})N_{\mathbf{q}}(1 + N_{\mathbf{q}'})\delta(\tilde{\xi}_{\mathbf{p}} + \tilde{\omega}_{\mathbf{q}} - \tilde{\xi}_{\mathbf{p}'} - \tilde{\omega}_{\mathbf{q}'}), \quad (15)$$

where the multiplier κ allows for the spin and valley degeneracy [see Eq. (2)]. Since the boson momentum is larger than $2p_F$, only the scattering processes are possible and not the boson emission or absorption. The matrix element M is

$$M = \frac{1}{V}\frac{W}{\sqrt{\omega_{\mathbf{q}}\omega_{\mathbf{q}'}}}.$$

Here, the dependence on the boson energy is written in the explicit form, while the possible angular dependence of W is of no importance.

Analysis of Eq. (15) yields the following expression for τ_{12}:

$$\frac{1}{\tau_{12}} = \frac{1}{\tau_{12}(0)}\left(\frac{m^*}{m_0^*}\right)^2 J(x_0);$$
$$J(x_0) = \int_{x_0}^{\infty}\frac{dx}{\sqrt{x^2 - x_0^2}}\int_{x_0}^{\infty}\frac{dy}{\sqrt{y^2 - x_0^2}} \quad (16)$$
$$\times \frac{x - y}{\sinh[(x-y)/2]\sinh(x/2)\sinh(y/2)}, \quad x_0 \equiv \omega_0/T.$$

This expression determines the desired temperature dependence. The phenomenological parameter $\tau_{12}(0)$ is a certain temperature-independent characteristic of the substance.

To obtain the ultimate answer to the question of temperature dependence of relaxation times, one should supplement Eqs. (13), (14), and (16) with the expressions for the spectra obtained in [4], namely,

$$\Delta^2 = \left(\frac{m^*}{m_0^*}\right)^2 \alpha T^2 + \omega_1^2 F(x_0),$$

$$\frac{m_0^*}{m^*} = 1 + \gamma F(x_0);$$

$$F(x_0) = 2\int_{x_0}^{\infty} \frac{dx}{\sqrt{x^2 - x_0^2}} \frac{1}{\exp(x) - 1} - \ln(x_0 T/\Omega_0), \tag{17}$$

$$\omega_0 = \sqrt{\Omega_0^2 + \Delta^2}$$

(Ω_0 is the gap in the boson spectrum at zero temperature). The dimensionless constants α and γ are related by the relationship $\alpha \approx \gamma^2/\kappa^2$; the estimate (as in [4], but taking into account the multivalley character of the spectra) suggests that, probably, $\gamma \sim 1$; ω_1 is a certain constant of energy dimension (it is determined by the interaction of bosons).

In the high-temperature limit $T \gg \omega_0$, Eq. (17) gives

$$\frac{m^*}{m_0^*} \approx \frac{\omega_0}{\gamma \pi T}, \quad \omega_0 \approx (\pi \omega_1^2 T)^{1/3}.$$

It is assumed that both temperature and ω_1 are small compared to the degeneracy temperature. The assumed smallness of ω_1 can be justified by the following speculation: if this is not so, then the boson–boson interaction is anomalously strong, which would be unreasonable.

If ω_1 is proportional to Ω_0, then the temperature behavior of the equilibrium quantities (ω_0/Ω_0, m^*/m_0^*) is governed by the ratio T/Ω_0 and described by a universal function, which seems to be reasonable. However, this is scarcely true for the resistance, because it depends on the other parameters.

The following general conclusions can be drawn about the resistance. The time $\tau_{12}(0)$ in Eq. (16) characterizes the substance and is insensitive to impurities. By contrast, $\tau_1(0)$ and $\tau_2(0)$ depend on the interaction with impurities. The following inequality should be fulfilled in a sufficiently pure sample:

$$\tau_{12}(0) < \tau_1(0), \quad \tau_2(0). \tag{18}$$

The experimental dependences are usually measured for the resistivity $\rho = 1/\sigma$. Below, two limiting cases are considered, ρ_0 at $T = 0$ and ρ_∞ at $T \gg \omega_0$. In the first case, only $\tau_1 = \tau_1(0)$ is finite, while in the second case only τ_{12} is retained, because τ_1 increases with temperature, τ_2 decreases, whereas τ_{12} tends towards a constant value which can be determined by the approximate evaluation of the integrals in Eqs. (16) and (17). Therefore, the resistivities in the above limiting cases are

$$\rho_0 = \frac{m}{ne^2}\frac{1}{\tau_1(0)}, \quad \rho_\infty = \frac{m}{ne^2}\frac{2}{\gamma^2}\frac{1}{\tau_{12}(0)}. \tag{19}$$

One can see from Eqs. (18) and (19) that the inequality $\rho_\infty > \rho_0$ is possible, and this is just what is observed in the experiment. The inequality should strengthen with an increase in mobility, because the limiting resistivity ρ_∞ does not depend on the sample purity (it is determined by the fermion scattering from immobile bosons), while ρ_0 is determined by the fermion scattering from impurities and decreases for more pure samples.

Further conclusions can be drawn only after calculations with particular values of the phenomenological parameters involved in the problem; this is beyond the scope of this work. It should merely be pointed out that both monotonic and nonmonotonic behaviors of resistivity between limiting values (19) are possible.

Note in conclusion that the temperature dependences were obtained in this work in the hydrodynamic approximation. One can show, using the general expression for the corrections to the distribution function, instead of those following from Eq. (4), that the results obtained for the high-temperature conductivity are also valid in the general case (this is evident for the low-temperature limit, where the contribution from bosons can be neglected). This issue, as well as a comparison with the experiment, will be discussed elsewhere in more detail.

I am grateful to A.V. Chaplik and M.V. Éntin for discussion. This work was supported in part by the Russian Foundation for Basic Research (project no. 00-15-96800) and the State Program of the Russian Federation, “Physics of Solid-State Nanostructures.”

REFERENCES

1. E. Abrahams, S. V. Kravchenko, and M. P. Sarachik, Rev. Mod. Phys. **73**, 251 (2001).
2. B. Spivak, cond-mat/0005328.
3. É. G. Batyev, Pis’ma Zh. Éksp. Teor. Fiz. **72**, 727 (2000) [JETP Lett. **72**, 506 (2000)].
4. É. G. Batyev, Pis’ma Zh. Éksp. Teor. Fiz. **73**, 635 (2001) [JETP Lett. **73**, 566 (2001)].

Translated by V. Sakun

JETP Letters, Vol. 74, No. 4, 2001, pp. 235–239. From Pis'ma v Zhurnal Éksperimental'noĭ i Teoreticheskoĭ Fiziki, Vol. 74, No. 4, 2001, pp. 258–262.

One-Dimensional Quantum Chaos: Explicitly Solvable Cases[1]

Yu. Dabaghian*, R. V. Jensen, and R. Blümel

Department of Physics, Wesleyan University, CT 06459-0155, Middletown, USA

** e-mail: ydabaghian@wesleyan.edu*

Received July 9, 2001

We present quantum graphs with remarkably regular spectral characteristics. We call them *regular quantum graphs*. Although regular quantum graphs are strongly chaotic in the classical limit, their quantum spectra are explicitly solvable in terms of periodic orbits. We present analytical solutions for the spectrum of regular quantum graphs in the form of explicit and exact periodic orbit expansions for each individual energy level. © *2001 MAIK "Nauka/Interperiodica"*.

PACS numbers: 05.45.Mt; 03.65.Sq

Consider a point particle moving along a network of bonds and vertices. Schematically, the network is represented by a graph Γ (see Fig. 1 for an example), which consists of N_B bonds and N_V vertices. The vertices are denoted by V_i; a bond connecting vertices i and j is denoted by B_{ij}. The set of bonds and vertices of Γ defines its *geometry*. We define a set of the bond potentials, $U_{ij}(k, x)$, where x and k are, correspondingly, the coordinate and the momentum of the particle on the bond B_{ij}. The vertices of Γ may be equipped with δ sources among others. The geometry of Γ does not uniquely define the dynamics of a particle on Γ. In fact, since for any given geometry the graph may be "dressed" with arbitrary bond and vertex potentials, there exist infinitely many "dynamical realizations" of Γ. We call the set of bond and vertex potentials the "dynamical dressing" of the graph. Previously [1–5], mainly the "bare-bond" graphs were studied, where the particle moves freely on the bonds.

In this paper, we focus on cases that have no turning points on the bonds; i.e., the energy of the particle is larger than all of the bond potentials, $E > U_{ij}(x, k)$, $x \in B_{ij}$. A simple way to implement this condition is to require that the system is *scaling* [6–10]. This implies $U_{ij}(x, k) = \lambda_{ij}(x)k^2$, where the functions $\lambda_{ij}(x)$ are bounded for all x. In this paper, we consider only simple cases where the functions $\lambda_{ij}(x)$ are x independent constants,

$$U_{ij}(x, k) = \lambda_{ij}k^2. \tag{1}$$

This is very similar to moving on a free graph except for substituting the bond lengths with the action lengths

$$S_{ij}^0 = \beta_{ij}L_{ij}, \tag{2}$$

where L_{ij} is the length of the bond B_{ij}, and $\beta_{ij} = \sqrt{1 - \lambda_{ij}}$. Scaling assumption (1) is not an oversimplification of the problem. Plenty of room is left for very interesting phenomena. Moreover, scaling quantum systems of this kind are the analogues of certain electromagnetic ray-splitting systems which have already been investigated experimentally in the laboratory [7–9].

For all but the most trivial graphs, i.e., linear or circular graphs with vanishing bond and vertex potentials, the classical motion on a graph, independently of any particular dressing, is fully chaotic with positive topological entropy [11]. This means that the number of possible periodic orbits traced by the particle increases exponentially with their lengths. If no dynamical turning points are present, the topological entropy is independent of the dynamical dressing and depends only on the geometry of the graph. Since at any vertex different from a "dead-end" vertex the classical particle has to choose randomly between several possibilities (reflection, transmission, branching), the particle's dynamical evolution resembles a stochastic Markovian process.

Given their classical chaoticity, it is surprising that the density of states of quantum graphs can be obtained exactly in terms of periodic orbit expansion series [1, 3–5]. Furthermore, quantum graphs are considerably "more integrable" than all the previously known exactly solvable quantum systems. For example, we will show below that for a certain class of quantum graphs—we call them *regular quantum graphs*—there exists an explicit and exact periodic orbit expansion for every quantum energy level. In other words, although

[1] This article was submitted by the authors in English.

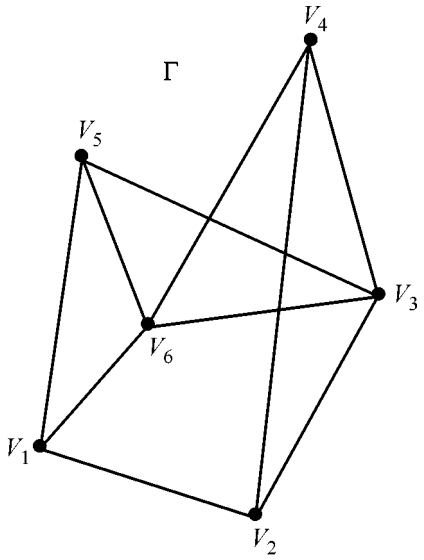

Fig. 1. A generic (quantum) graph with six vertices and ten bonds.

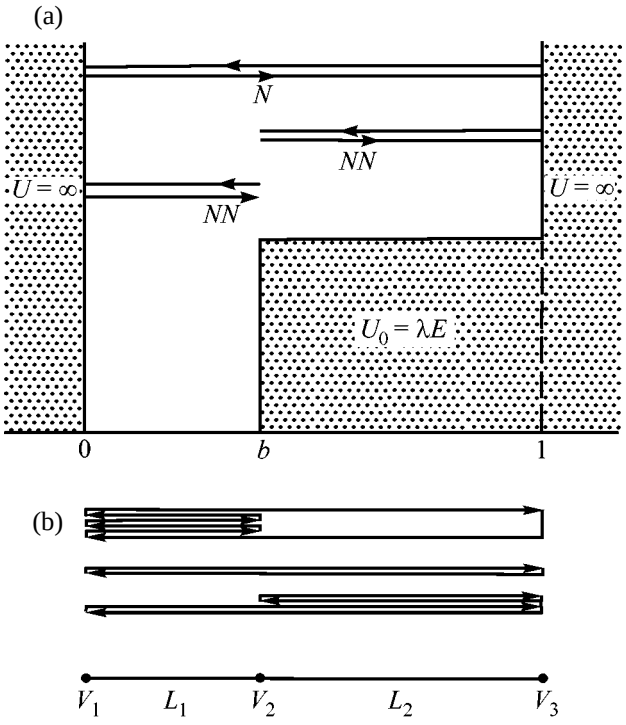

Fig. 2. (a) Simple step potential, a basic problem in one-dimensional quantum mechanics. Also shown are examples of Newtonian *N* and non-Newtonian (*NN*) periodic orbits used in the periodic orbit expansion of its energy eigenvalues (see text). (b) Three-vertex hydra graph corresponding to the step potential above.

the classical limit of regular quantum graphs is chaotic, each individual level of their spectra can be obtained exactly and explicitly via an analytical formula containing an explicit sum over the periodic orbits of the graph. To the authors' knowledge, this is the first time that the spectrum of a quantum chaotic system is obtained both *exactly* and *explicitly.*

The formal definition of regular quantum graphs is based on the properties of the spectral equation [3–5]

$$\det[1 - S(k)] = 0, \tag{3}$$

where $S(k)$ is the scattering matrix of the graph [3]. The modulus of complex function (3) is a trigonometric polynomial of the form

$$\cos(S_0 k - \pi\gamma_0) - \Phi(k) = 0, \tag{4}$$

where

$$\Phi(k) = \sum_i a_i \cos(S_i k - \pi\gamma_i) \tag{5}$$

and

$$S_0 = \frac{1}{k}\sum_{i<j}\int_{B_{ij}} k_{ij}(x)dx \tag{6}$$

is the total reduced action length of the graph Γ, and the constant frequencies $S_i < S_0$ naturally emerge as combinations of reduced classical actions (2). Under the scaling assumption, the coefficients a_i, γ_0, and γ_i are constants.

We now define regular quantum graphs. They satisfy

$$\alpha = \sum_i |a_i| < 1. \tag{7}$$

The motivation for this definition is the following: it allows us to solve Eq. (4) formally for the momentum eigenvalues k_n,

$$k_n = \frac{\pi}{S_0}[n + \mu + \gamma_0] + \frac{1}{S_0}\begin{cases}\arccos(\Phi(k_n)), & \text{for } n+\mu \text{ even}\\ \pi - \arccos(\Phi(k_n)), & \text{for } n+\mu \text{ odd},\end{cases} \tag{8}$$

where μ is a fixed integer chosen such that k_1 is the first non-negative solution of Eq. (4). Because of Eq. (7), the second term in Eq. (8) assumes only values between u and $\pi/S_0 - u$, where $0 < u = \arccos(\alpha)/S_0 < \pi/2S_0$. Thus, for regular graphs, the points

$$\bar{k}_n = \frac{\pi}{S_0}(n + \gamma), \quad n = 1, 2, \ldots, \quad \gamma \equiv \mu + \gamma_0 \tag{9}$$

are guaranteed not to be roots of Eq. (3) and serve as separators between root numbers n and $n + 1$. Obviously, function (9) reflects the average behavior of the levels of the momentum. It is simply the inverted average staircase, $\bar{k}_N = \bar{N}(k)^{-1}$. Geometrically, points (9) are the intersection points between the staircase func-

tion $N(k) \equiv \sum_n \Theta(k - k_n)$ and the average staircase $\bar{N}(\bar{k})$, resulting in the crossing condition

$$\bar{N}(\bar{k}_n) = N(\bar{k}_n) = n. \tag{10}$$

Crossing condition (10) is illustrated in Fig. 3.

The existence of separating points (9) implies that roots (8) are confined to the "root zones," or "root intervals" $I_n = [\bar{k}_{n-1}, \bar{k}_n]$, $n = 1, 2, \ldots$. If $\alpha \le C < 1$ holds (C constant), Eq. (8) implies the existence of finite-width root-free "forbidden zones" $R_n = (\bar{k}_n - u, \bar{k}_n + u)$ surrounding every separating point $\bar{k}_n$, where no roots of Eq. (3) can be found. The roots of Eq. (3) can only be found in the "allowed zones" $Z_n = [\bar{k}_{n-1} + u, \bar{k}_n - u]$, which are subsets of the root intervals $I_n = [\bar{k}_{n-1}, \bar{k}_n]$. For $C \longrightarrow 1$, the width of the forbidden regions shrinks, $u \longrightarrow 0$, and the allowed zones occupy the whole interval, $Z_n \longrightarrow I_n$.

Since S_0 is the largest action in Eqs. (4) and (5), it can be shown [12] that k_n is the *only* root in Z_n. Therefore, there is exactly one root k_n inside of $Z_n \subset I_n$, and this root is bounded away from the separating points $\bar{k}_{n-1}$ and $\bar{k}_n$ by a finite interval of length $2u$.

The existence of separating points (9) and the root-free zones R_n are the key for obtaining an explicit and exact periodic orbit expansion for every root of Eq. (3). The starting point for obtaining the explicit expressions is the exact periodic orbit expansion for the density of states, $\rho(k) \equiv \sum_{j=1}^{\infty} \delta(k - k_j)$. As shown in [1, 3–5], it can be written explicitly as

$$\rho(k) = \bar{\rho}(k) + \frac{1}{\pi}\mathrm{Re}\sum_p S_p^0 \sum_{\nu=1}^{\infty} A_p^\nu e^{i\nu S_p^0 k}. \tag{11}$$

Here, $\bar{\rho}(k)$ is the average density of states, ν is the repetition index, and S_p^0 and A_p are, correspondingly, the reduced action and the weight factor of the prime periodic orbit labeled by p. In the scaling case, S_p^0 and A_p are k-independent constants [12]. Multiplying the density of states by k and integrating from $\bar{k}_{n-1}$ to $\bar{k}_n$ yields the value of the root contained between these separating points,

$$\int_{\bar{k}_{n-1}}^{\bar{k}_n} \rho(k) k dk = \int_{\bar{k}_{n-1}}^{\bar{k}_n} \sum_{j=1}^{\infty} \delta(k - k_j) k dk = k_n. \tag{12}$$

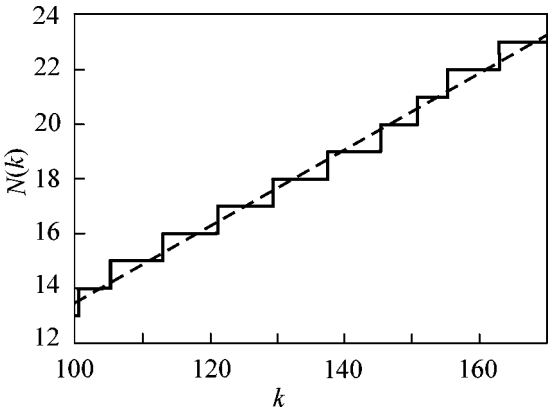

Fig. 3. The staircase function NN and the average staircase $\bar{N}(k)$. For the regular graphs, the average staircase intersects every "stair" of the $N(k)$ graph, with separation (9) showing as the intersection points $N(\bar{k}_n) = \bar{N}(\bar{k}_n)$.

Performing the same procedure using series expansion representation (11) and crossing condition (10), we obtain

$$k_n = \frac{\pi}{S_0} n - \frac{2}{\pi}\sum_p \frac{1}{S_p^0}\sum_{\nu=1}^{\infty}\frac{A_p^\nu}{\nu^2}\sin\left(\frac{\pi}{2}\nu\omega_p\right)\sin(\pi\nu\omega_p n), \tag{13}$$

where $\omega_p = S_p^0/S_0$ and the A_p's are assumed to be real (no vertex potentials).

Since all of the quantities on the right-hand side of Eq. (13) are known, this formula provides an explicit representation of the roots k_n of spectral Eq. (3) in terms of the geometric and dynamical characteristics of the graph. To our knowledge, this is the first time that the energy levels of a chaotic system are expressed explicitly in terms of a periodic orbit expansion. Previously, explicit formulas for individual energy levels were known only for integrable systems. In the context of periodic orbit theory, the energy levels of integrable systems are given by the Einstein–Brillouin–Keller (EBK) formula [11]. However, apart from a few exceptional cases [13], EBK quantization is only of semiclassical accuracy.

The difference between formulas (11) and (13) is profound. Density of states (11) allows the computation of spectral points only indirectly as the singularities of Eq. (11). Formula (13), on the other hand, allows the computation of every quantum level *individually*, *explicitly*, and *exactly* in terms of classical parameters.

In order to demonstrate that the class of regular quantum graphs is not empty, we present an explicit example: the one-dimensional scaled step potential with $V_0 = \lambda E$. A sketch of this potential is shown in Fig. 3. Physically, this potential is realized, e.g., by a

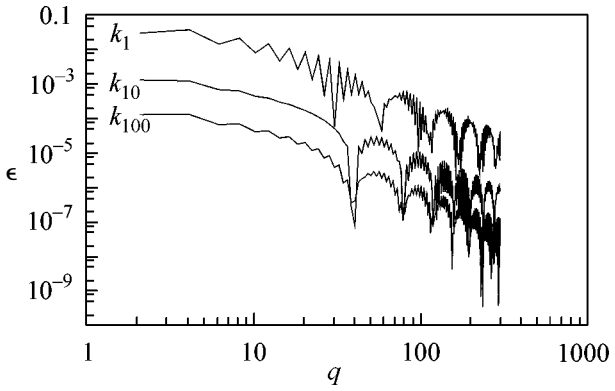

Fig. 4. Relative error $\epsilon_n^{(q)} = \left|k_n^{(q)} - k_n^{\text{exact}}\right| / k_n^{\text{exact}}$ of (13) (see text) by including periodic orbits up to length q. The three curves shown correspond to k_1, k_{10}, and k_{100}, as indicated in the figure.

rectangular microwave cavity partially loaded with a dielectric substance [7–9]. The scaling step potential is equivalent to the scaling three-vertex linear graph shown in Fig. 2b. It has two bonds $L_1 = b$ and $L_2 = \beta(1 - b)$; the single scaling constant β [see Eq. (2)] is given by $\beta = \sqrt{1-\lambda}$. The spectral equation is given by

$$|\det[1 - S(k)]| = \sin(Lk) - r\sin[(L_1 - L_2)k] = 0, \quad (14)$$

where $L = L_1 + L_2$ and $r = (1 - \beta)/(1 + \beta)$ is the reflection coefficient at the vertex V_2 between the two bonds. It defines the eigenvalues k_n only implicitly and is usually solved by graphical or numerical methods. Application of Eq. (13), however, solves Eq. (14) explicitly in terms of periodic orbits such as the ones shown in Fig. 2. In order to apply Eq. (14), we need the coefficients A_p. They are given by [10, 12]

$$A_p = (-1)^{\chi(p)} r^{\sigma(p)} (1 - r^2)^{\tau(p)/2}, \quad (15)$$

where r is the reflection coefficient at the middle vertex and $\sigma(p)$ and $\tau(p)$ are, correspondingly, the number of the reflections and the transmissions through it. Since the reflection coefficient may be positive or negative, depending on whether the particle scatters from the right or from the left, the factor $(-1)^{\chi(p)}$ is needed to keep track of how many times it appears with a minus sign, including the sign changes due to the wall ($x = 0$ and $x = 1$) reflections.

In order to illustrate the convergence of series (13), we computed k_1, k_{10}, and k_{100} of the scaling step potential including periodic orbits of increasing binary length q. For the parameters of the potential, we chose $b = 0.3$ (see Fig. 2) and $\lambda = 1/2$. Figure 4 shows the relative error $\epsilon_n^{(q)} = \left|k_n^{(q)} - k_n^{\text{exact}}\right| / k_n^{\text{exact}}$ for $n = 1$, 10, and 100 and q ranging from 1 to 150. We see that even for small q the relative error is very small, decreasing further for large q as a power-law in q. The power of convergence appears to be the same for all three k and is close to –2. The convergence with q is an important result. It indicates that, although series (13) is only conditionally convergent, it (i) converges to the correct result and (ii) is not just asymptotically convergent but keeps converging when more and more periodic orbits are included.

Additional examples of regular quantum graphs are provided by all linear and circular quantum graphs with at most two bonds per vertex, independently of the number of vertices. In other words, for any simply connected quantum graph and any dynamical dressing there always exists a set of scaling constants λ_{ij} of finite measure such that regularity condition (7) is fulfilled. Well-known particular cases of these simply connected quantum graphs are the "Manhattan potentials," which are obvious generalizations of the simple step potential, shown in Fig. 2a, to arbitrarily many steps inside of the well and linear chain graphs with scaling δ function potentials at the vertices.

It should be emphasized that "inverse staircase expansion" (13) is not just a curious finding, valid for some simple 1D systems such as quantum graphs. Similar explicit series may be obtained for more complicated higher dimensional systems when the following two key ingredients are available. The first ingredient is the exact series expansion of density of states (11), which has already been established for other classically chaotic systems such as, e.g., quantum billiards [14]. The second ingredient is a (piercing) average staircase function $\bar{N}(k)$ or the inverted staircase function $\bar{k}_n$ *which intersects every stair of the staircase,* $\bar{N}(\bar{k}_n) = N(\bar{k}_n) = n$, $n = 1, 2, \ldots$. The intersection points k_n then serve as the separators for the possible root locations, and the procedure outlined in the text can be used to find the periodic orbit expansions for individual roots of the system at hand. In most cases, of course, it is highly nontrivial to obtain these two necessary ingredients. The quantum graphs themselves are an excellent illustration of this point. While expansion (11) is valid for all quantum graphs, it is crossing condition (10) that is violated when inequality (7) breaks down. The regular graphs are precisely those for which the line $\bar{N}(k) = S_0 k/\pi + \gamma$ satisfies Eq. (10) and allows the application of the analytical procedure that resulted in explicit formula (13) for the representation and computation of individual eigenvalues k_n.

Y.D. and R.B. gratefully acknowledge financial support by the NSF, grant nos. PHY-9900730 and PHY-9984075; Y.D. and R.J by the NSF, grant no. PHY-9900746.

REFERENCES

1. J.-P. Roth, in *Lecture Notes in Mathematics*, Vol. 1096: *Théorie du Potentiel*, Ed. by A. Dold and B. Eckmann (Springer-Verlag, Berlin, 1984), pp. 521–539.

2. E. Akkermans, A. Comtet, J. Desbois, *et al.*, cond-mat/9911183.
3. T. Kottos and U. Smilansky, Phys. Rev. Lett. **79**, 4794 (1997).
4. T. Kottos and U. Smilansky, Ann. Phys. **274**, 76 (1999).
5. H. Schanz and U. Smilansky, Phys. Rev. Lett. **84**, 1427 (2000).
6. R. E. Prange, E. Ott, T. M. Antonsen, *et al.*, Phys. Rev. E **53**, 207 (1996).
7. L. Sirko, P. M. Koch, and R. Blümel, Phys. Rev. Lett. **78**, 2940 (1997).
8. Sz. Bauch, A. Bł˛edowski, L. Sirko, *et al.*, Phys. Rev. E **57**, 304 (1998).
9. R. Blümel, P. M. Koch, and L. Sirko, Found. Phys. **31**, 269 (2001).
10. Y. Dabaghian, R. V. Jensen, and R. Blümel, Phys. Rev. E **63**, 066201 (2001).
11. M. Gutzwiller, *Chaos in Classical and Quantum Mechanics* (Springer-Verlag, New York, 1990).
12. Y. Dabaghian, R. V. Jensen, and R. Blümel, in preparation.
13. R. I. Szabo, hep-th/9608068 (1996).
14. K. G. Anderson and R. B. Melrose, Invent. Math. **41**, 197 (1977).

JETP Letters, Vol. 74, No. 4, 2001, pp. 240–243. Translated from Pis'ma v Zhurnal Éksperimental'noĭ i Teoreticheskoĭ Fiziki, Vol. 74, No. 4, 2001, pp. 263–266.

Ultrahigh-Spatial-Resolution Field-Emission Projection Microscopy of Insulating Samples

B. N. Mironov, D. A. Lapshin, S. K. Sekatskiĭ, and V. S. Letokhov

Institute of Spectroscopy, Russian Academy of Sciences, Troitsk, Moscow region, 142190 Russia

Received July 13, 2001

The method of ultrahigh-spatial-resolution field-emission projection imaging of nonconducting tips is implemented experimentally. An image of a glass microcapillary tip was obtained for the first time by the nonscanning method with spatial resolution no worse than 20 nm. © *2001 MAIK "Nauka/Interperiodica".*

PACS numbers: 68.37.Vj; 79.70.+q

The methods of field-emission and field-ion microscopy make possible the imaging of metallic and semiconducting tips with an ultrahigh spatial resolution (a few nanometers for field-emission version and angstroms, "routine single-atomic resolution," for field-ion version), thus providing unique opportunities for research in surface physics, nanotechnology, etc. (see, e.g., [1]). These methods are based on the fact that a radial electric field occurring in the vicinity of tips directs (projects) emitted electrons or ions onto a detector. Accordingly, the microscope magnification M is determined by the ratio of the tip-to-detector distance L to the radius of curvature r of the tip,

$$M = L/\chi r, \quad (1)$$

it can be as high as several millions for submicron tips (χ is a numerical factor caused by the deviation of the microscope geometry from an ideal spherical capacitor; for real instruments, it ranges from 1.5 to 2 [1]).

It was long recognized that high conductivity of tips is not crucial for the physical implementation of the projection imaging principle. The equilibrium distribution of surface charges in insulating tips coincides with or, at least, is close to the distribution typical of conductors. In this case, the radial projecting electric field can also arise, and, hence, field-emission imaging with high spatial resolution is possible if the ultrahigh sensitivity allowing the operation with exceedingly weak field-emission currents is achieved and if the emitted charge is replenished within a reasonably short time. Nevertheless, inspite of the theoretical premises and the possibility of observing (thermal) field emission from semiconductors with very low conductivity and insulators (see, e.g., [2–4]), data on the observation of field-emission images of insulating tips with high spatial resolution are lacking in the literature, so the question of obtaining such images remains open. This letter reports the observation of field-emission images of insulating tips with a high spatial resolution no worse than 20 nm.

Standard World Precision Instruments (Germany) microcapillaries (quartz glass with resistivity $\rho = 10^{16}$–10^{18} Ω cm [5]) with 2-μm- and 100-nm-diameter holes for fluid ejection and analogous 2-μm-diameter microcapillaries made from Pyrex-type glass ($\rho \cong 2 \times 10^{14}$ Ω cm [5]) at the Institute of Cell Biophysics, Russian Academy of Sciences (Pushchino), were used as samples for investigation. Such a choice was dictated not only by the interest in imaging the structure of these samples but also by the fact that these microcapillaries are used as active elements (probes) in rapidly progressing scanning near-field optical microscopy (see, e.g., [6]), where they are considered as the most suitable probes for the implementation of the recently suggested method of near-field optical microscopy based on the resonance dipole–dipole fluorescence excitation or quenching in the sample (see our works [7, 8]). The microcapillaries were glued with silver paste to an electrode, to which voltage U was applied, and placed into the chamber of a laser projection field-emission microscope, which was described in detail in [9]. The microcapillaries were oriented perpendicular to the detector surface (microchannel plate + phosphorus screen, working zone 28 mm in diameter; made in Russia); the image at the detector output was photographed by a high-sensitivity TV camera and processed on a specialized Argus-50 processor (Hamamatsu Photonics C.C., Japan). A distance L from the tip to detector was reduced, as compared to our previous works, from 10–12 to 6 cm, in order to diminish the microscope magnification and observe the entire image of the microcapillary tip at the detector.

A series of images successively obtained at a voltage $U = -4$ kV for the tip of a microcapillary with a 2-μm-diameter hole is shown in Fig. 1 (immediately prior to recording images, the sample was held at a voltage of +5 kV for approximately 1 h). One can see that, first, the hole is clearly seen in all images and, second, the magnification factor of the microscope increases with a large time constant $t \cong 500$–1500 s. The dynam-

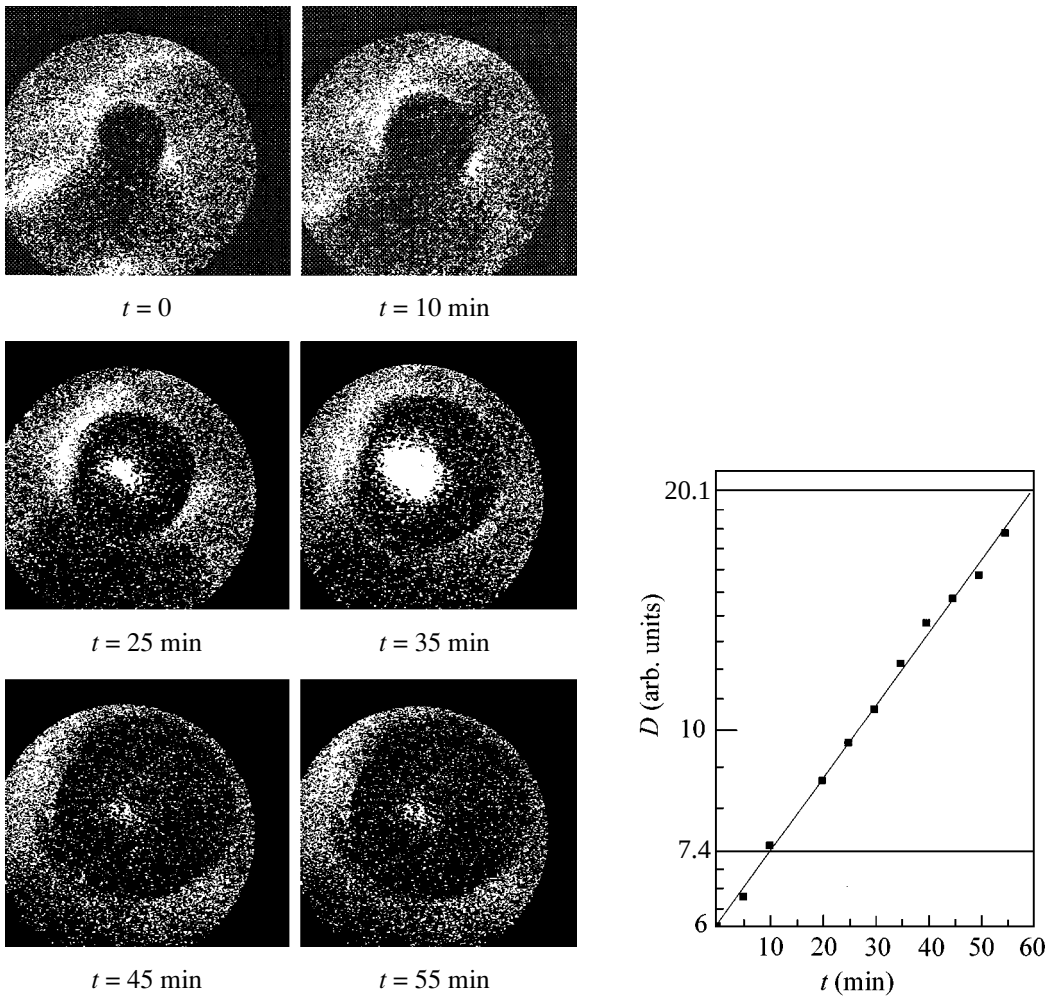

Fig. 1. Field-emission images of the tip of a quartz glass microcapillary with a 2-μm-diameter channel. The images were obtained within indicated time intervals after switching the potential. The typical time of recording one image was 5 min. Image size as a function of time is shown in the graph on the logarithmic scale. In some images, a bright field-emission area is seen in the hole center. These areas were observed occasionally (especially often immediately after establishing the working potential) and are likely due to the sporadic ejection of electrons and other charged particles from the capillaries.

ics of this increase is illustrated by the graph in Fig. 1. Note that the last ("quasistationary") image is close to that which would be expected for the standard (for conducting tips) magnification of a field-emission microscope [see Eq. (1)] and the screen size.

This dynamics can be interpreted as follows. After prolonged holding at a positive voltage, charge distribution in the system becomes close to the electrostatically equilibrium one. A change in the potential disturbs this equilibrium, after which the system starts to evolve to a new equilibrium. During this process, a weak electric current flows through the system, and the external electron emission also occurs and produces an image of the microcapillary tip at the detector. The features of this image (primarily the magnification factor) are determined by the transient (nonstationary) potential distribution, and, as the equilibrium is approached, one ultimately obtains the image that is close to the standard "metallic" image with ultrahigh spatial resolution.

The majority of insulating samples have a small "residual" bulk resistivity $\rho \leq 10^{15}\ \Omega$ cm, which is, nevertheless, sufficient for establishing charge distribution within a reasonably short time and provides the required bias on the tip, as we have demonstrated earlier in studying the laser projection photoelectron and photoion images of LiF- and glass-made tips [9, 10]. The resistance of a cone-shaped sample with angle ϑ and radius of curvature r of the tip apex is given by the formula

$$R = \rho/\pi r \tan\vartheta, \qquad (2)$$

while the equilibration time can be estimated using the Maxwellian relaxation time $t_M \cong \rho\epsilon\epsilon_0$. For $\rho = 10^{15}\ \Omega$ cm one has $t_M \approx 500$ s; note that a good agreement between the experimentally measured time of establishing sur-

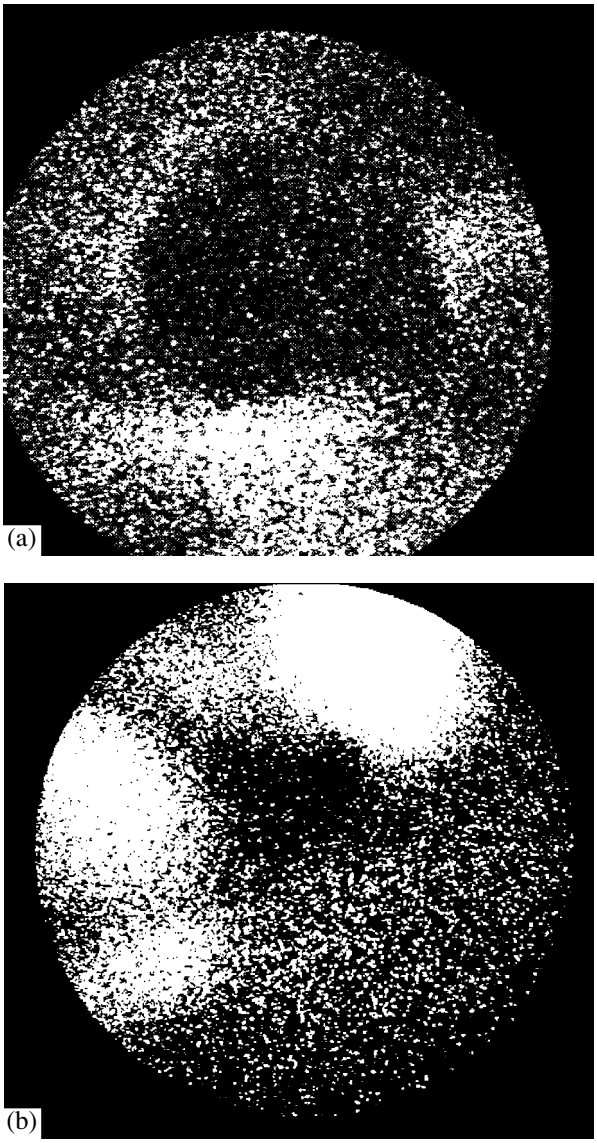

Fig. 2. (a) Field-emission image obtained at a voltage $U = -4$ kV for the tip of a quartz glass microcapillary with a 100-nm-radius hole. (b) Field-emission image of the same tip coated with a gold layer of thickness 5 nm by ion sputtering.

face potential (1.5 min) and the Maxwellian time (1.7 min) was observed precisely for the Pyrex-type glass [11]. Although a considerable portion ΔU of a bias of several kilovolts U applied to the tip can be expended on maintaining the current through the sample, the bias on the tip $U - \Delta U$ is still sufficient to induce a field emission and create a radial projecting field. For the typical $\Delta U = 1$ kV and a current of ~300 electrons per second (which is more than sufficient to produce images), one has $\sim 3 \times 10^{19}\ \Omega$ for the maximum possible resistance, in accordance with the above-mentioned estimate $\rho \le 10^{15}\ \Omega$ cm for $r = 1\ \mu$m and $\tan\vartheta \sim 0.1$ [9].

The magnification factor M of the microscope depends on the voltage drop on the sample (i.e., on the ratio of ΔU to $U - \Delta U$). This fact (i.e., that the magnification factor M for the nonideally conducting samples is lower than for the metallic tips and that it depends on the potential distribution over the sample) was already observed in the practice of field-emission microscopy (see, e.g., the discussion of the influence of the sample voltage and field penetration depth on the size of field-emission images of semiconducting tips [12]). In [13], a new method of calculating electric fields was suggested for the systems with nonzero voltage drop on the sample, and it was demonstrated by direct calculation that the factor M rapidly increases as ΔU decreases, i.e., as the charge distribution approaches the form typical of metals. This allows the qualitative explanation of the dynamics of field-emission images shown in Fig. 1: the magnification factor increases as the system approaches charge equilibrium.

The possibility of observing photoelectron images of even better insulators, for which the bulk conductivity cannot provide observable charge-equilibration times and explain the presence of a rather large bias on the tip (e.g., for quartz glass), is due, in our opinion, to the surface conduction processes. It is known that the surface conductivity of very good insulators is, as a rule, higher than the bulk conductivity (see, e.g., [11, 14–16]), and the dynamics of establishing surface potential is much more complex (and, as a rule, much faster) than follows from the simple models of bulk conductivity (see, e.g., [11, 14, 17] and references therein). For example, these times differ by more than an order of magnitude for PMMA: 15 min and 2.6 h, respectively [11]. As for quartz and glass, it was shown in early atomic-force microscopy studies of the charge-dissipation dynamics at the insulator surfaces that the redistribution time for a localized charge at the quartz surface is as short as a few minutes and even seconds, despite the very low conductivity [18]. Note also that the processes of surface conduction are particularly important for the sharpest samples, because the net resistance of such samples weakly (logarithmically) depends on the radius of curvature of the tip apex:

$$R = \frac{\rho_s}{2\pi \tan\vartheta} \ln R_0/r. \qquad (3)$$

Here, ρ_s is the surface resistivity (in ohms) and R_0 is the radius of the sample at the site of its fastening to the metallic electrode. It follows from the above estimates that the surface resistance of $\sim 2 \times 10^{18}\ \Omega$, typical of many insulators [11, 14–16], is sufficient to observe field-emission images.

The interaction of the tip surfaces with atoms (ions) of residual gas and the modification of conductivity in strong electric fields may also play a certain role. We are currently performing additional experiments to elucidate these issues.

In summary, the method of field-emission imaging of nonconducting tips with ultrahigh spatial resolution is experimentally implemented. The method is based on successive registration and analyzing of the field-emission images recorded as the system approaches charge equilibrium. The spatial resolution of the method is determined by the same factors as in the conventional field-emission studies of conducting samples (the broad energy distribution of emitted electrons) [1] and is approximately the same.

The efficiency of the method is best illustrated in Fig. 2a, where the field-emission image of the tip of a quartz glass microcapillary with a 100-nm-diameter hole is shown. Such objects can be analyzed neither with the standard optical microscope nor (without metal deposition, which makes the capillary unsuitable for the method of near-field optical microscopy developed in [7, 8] and for some other applications) with the electron microscope. For comparison, a field-emission image of the same tip, though coated with a 5-nm-thick gold layer by ion sputtering, is also shown in Fig. 2b. One can see that the quality and magnification of both images are comparable.

REFERENCES

1. T. T. Tsong, *Atom-Probe Field Ion Microscopy* (Cambridge Univ. Press, New York, 1990).
2. P. G. Borzyak, A. F. Yatsenko, and L. S. Miroschnichenko, Phys. Status Solidi **14**, 403 (1966).
3. V. M. Efimov, V. A. Kolosanov, and S. P. Sinitsa, Phys. Status Solidi A **49**, 217 (1978).
4. C. Schonenberger and S. F. Alvarado, Phys. Rev. Lett. **65**, 3162 (1990).
5. E. B. Shand, *Glass Engineering Handbook* (McGraw-Hill, New York, 1958).
6. A. Lewis and K. Lieberman, Nature **351**, 214 (1991).
7. S. K. Sekatskiĭ and V. S. Letokhov, Pis'ma Zh. Éksp. Teor. Fiz. **63**, 311 (1996) [JETP Lett. **63**, 319 (1996)].
8. S. K. Sekatskiĭ, G. T. Shubeita, M. Chergui, *et al.*, Zh. Éksp. Teor. Fiz. **117**, 885 (2000) [JETP **90**, 769 (2000)].
9. V. N. Konopsky, S. K. Sekatskii, and V. S. Letokhov, Appl. Surf. Sci. **94/95**, 148 (1996).
10. S. K. Sekatskiĭ, Zh. Éksp. Teor. Fiz. **112**, 1273 (1997) [JETP **85**, 690 (1997)].
11. H. T. M. Haenen, J. Electrost. **1**, 173 (1975).
12. G. N. Fursey and N. V. Egorov, Phys. Status Solidi **32**, 23 (1969).
13. S. K. Sekatskii, Ultramicroscopy **73**, 245 (1998).
14. G. M. Sessler, *Topics in Applied Physics*, Vol. 33: *Electrets* (Springer-Verlag, Berlin, 1980).
15. A. V. Dmitriev and S. S. Chang, Zh. Tekh. Fiz. **36**, 547 (1966).
16. M. I. Landstass and K. V. Ravi, Appl. Phys. Lett. **55**, 1391 (1989).
17. H. J. Wintle, J. Appl. Phys. **81**, 2682 (1997).
18. J. E. Stern, B. D. Terris, H. J. Mamin, and D. Rugar, Appl. Phys. Lett. **53**, 2717 (1988).

Translated by V. Sakun